FACULDADE DE ENGENHARIA DA UNIVERSIDADE DO PORTO

Control and supervision of an AGV with energy consumption optimization

Nuno Miguel Teixeira das Neves Lobo

Mestrado Integrado em Engenharia Eletrotécnica e de Computadores

Supervisor: Adriano da Silva Carvalho

October, 2021

Resumo

Os veículos guiados autónomos (AGVs) ganharam enorme importância e interesse no campo da indústria. Estes são soluções populares para o transporte de bens materiais para diferentes partes das fábricas. No entanto, em muitas fábricas, os armazéns estão localizados à parte da linha de produção ou em edifícios separados, exigindo que o transporte de bens materiais seja feito exteriormente. Os ambientes exteriores representam um desafio particular para os AGVs. Por um lado, estes ambientes causam mais desgaste nos componentes dos veículos e o clima na Europa pode atingir extremos opostos, dependendo da estação do ano e das regiões. Por outro lado, estes ambientes aumentam as preocupações de segurança, uma vez que outros veículos ou peões podem circular no mesmo espaço e ao mesmo tempo.

Neste projecto, um rebocador eléctrico XXL será transformado num AGV, que opera em ambiente exterior. Este veículo é responsável pelo transporte de mercadorias do final da linha de produção para o armazém exterior numa fábrica de automóveis. O principal objectivo é assegurar o seu funcionamento contínuo durante um turno de 16 horas, garantindo o mínimo de interrupções para v«carregamento da bateria. Desta forma, nesta dissertação foram abordados dois capítulos distintos: para a análise e estudo do consumo energético foi simulado a powertrain de um veículo eléctrico. Neste, foi considerado um motor de indução cujo método de controlo aplicado foi o Field Oriented Control (FOC). Para além do comportamento eléctrico, também foi simulado o modelo físico da carga, bem como o cálculo da energia eléctrica consumida. Para a navegação, foi estudada uma solução baseada na integração do GPS com o INS. Dadas as restrições temporais, apenas a solução GPS foi testada e a técnica Loosely Coupled foi abordada como uma possível solução de integração.

Palavras-Chave: AGV exterior, otimização energética, GPS/INS, controlo vetorial

Abstract

Autonomous guided vehicles (AGVs) have gained enormous importance and interest in the industry field. These are popular solutions for transport of good and material to different parts of the factories. However, in many factories, warehouses are located apart from the factory floor or in separate buildings, requiring the transport of material goods to be done outdoors. Outdoor environments represent a particular challenge for AGVs. On one hand, these environments causes more wear and tear on vehicle components and the weather in Europe can reach opposite extremes depending on the season and regions. On the other hand, these environments increase safety concerns since other vehicles or pedestrians can circulate in the same space at the same time.

In this project, an electric tugger XXL will be transformed into an AGV, which operates in outdoor environment. This vehicle is responsible for transporting goods from the end of the production line to the outside warehouse in a car manufacturing plant. The main objective is to ensure its continuous operation during a 16-hour shift, and guarantee the minimum battery charging actions. In this way, in this dissertation two distinct chapters were approached: for the analysis and study of the energy consumption it was simulated the powertrain of an electric vehicle. In this one it was considered an induction motor whose control method applied was the Field Oriented Control (FOC). Besides the electrical behaviour, also the physical model of the load was simulated as well as the calculation of the consumed electrical energy. For navigation, a solution based on the integration of GPS with INS was studied. Given the temporal constraints, only the GPS solution was tested and the loosely coupled technique was approached as a possible integration solution.

Keywords: Outdoor AGV, Energy optimization, GPS/INS, Field Oriented Control

Agradecimentos

Quero agradecer a todas as pessoas que diretamente ou indiretamente me ajudaram a concluir este projeto. Neste grupo mencionado, devo agradecer com especial atenção à paciência e disponibilidade demonstrada pelo meu orientador, Adriano Carvalho, que, sempre que requisitado, me tentou ajudar ou me comunicou possíveis soluções para os problemas que foram aprecendo ao longo do desenvolvimento desta dissertação. Devo também agradecer aos meus pais que sempre respeitaram o meu espaço e silêncio em casa. Foi fundamental essa tranquilidade, especialmente tendo em conta dos successivos confinamentos impostos pela pandemia.

Nuno Lobo

"Be the change that you wish to see in the world."

Mahatma Gandhi

Contents

List of Figures

List of Tables

Abbreviations and symbols

AGV	Automated Guided Vehicle
DGPS	Differential Global Positioning System
DR	Dead Reckoning
DTC	Direct Torque Control
EKF	Extended Kalman Filter
FOC	Field Oriented Control
GLONASS	Globalnaya Navigazionnaya Sputnikovaya Sistema
GNSS	Global Navigation Satellite System
GPS	Global Positioning System
IIoT	Industrial Internet of Things
INS	Inertial Navigation System
IoT	Internet of Things
LC	Loosely coupled
KF	Kalman Filter
LIB	Lithium-ion battery
LIDAR	Light Detection And Ranging
NMEA	National Marine Electronics Association
P	Proportional
PI	Proportional-Integral
PID	Proportional–Integral–Derivative
PLC	Programmable Logic Controllers
RTK GPS	Real-Time Kinematic Global Positioning System
SA	Simulated Annealing
SLAM	Simultaneous Localization and Mapping
SLC	Small Load carrier
SOC	State-of-charge
TC	Tightly coupled
VSI	Voltage Source Inverter
WLAN	Wireless Local Area Network

Chapter 1

Introduction

1.1 Context

With a current economy that demands very fast changes in manufactured products and many of them with specific characteristics for each customer, flexibility is an essential requirement for today's industries in order to be able to produce more and at lower costs, in others words, for industries to be more efficient and manageable. For this reason, companies try to find solutions to optimize production and logistics processes. Advances in technology have taken the industry to a new level, the Industry 4.0, which aims to meet the needs of today's industry as well as to increase the freedom of processes through the possibility for systems to perform self-making-decisions, making processes more seamless and relying less on human intervention [34].

It is in this context that autonomous guided vehicles (AGV) gain enormous importance and interest in the industry field. These are popular solutions for transport of good and material to different parts of the factories. Therefore, they are considered the key to the logistics and automation of the plants. The industry 4.0, also known as IIoT, has overcome the concern about systems integration through wireless sensor communication and implementation, but the possibility for systems to take new decisions autonomously has raised security concerns. Traditionally, AGVs work in closed environments with pre-defined paths, with limited speed so that they are able to stop safely once an obstacle is detected by their on-board sensors. With the evolution of navigation technologies motivated by this new concept of industry and new autonomous cars systems, those vehicles have reached a degree of autonomy that allows their operation beyond closed work environments [23].

However, outdoor environments represent a particular challenge for AGVs. On one hand, these environments causes more wear and tear on vehicle components and the weather in Europe can reach opposite extremes depending on the season and regions such as:

- Extreme temperatures variations (from -30 ^{o}C in winter and up to 40 ^{o}C in summer)
- Extreme temperature variations for mixed indoor/outdoor operations

- Different lightning conditions (darkness, cloudy skies, extreme sunlight and low-standing sun)
- Fog, snowfall, heavy rain, wind or black ice/sleet
- Varying surface conditions (dry, wet, ice or snow), which influence traction and braking ability

which leads to rigorous planning and construction of an outdoor AGV [28]. On the other hand, these environments increase safety concerns since other vehicles or pedestrians can circulate at the same time. This means that new challenges must be overcome, such as avoidance of moving obstacles, whose appearance cannot be determined in advance [23].

1.2 Objectives

In this project an electric tugger XXL will be transformed into AGV, which operates in outdoor environment. This vehicle is responsible for transporting goods from the end of the production line to the outside warehouse in a car manufacturing plant and must have circulation times that ensure the continuous operation of the production line during two continuous shifts (16 hours). In this way, we can split this project into the following objectives:

- The AGV must know its location in order to be able to move autonomously and, being an outdoor environment, traditional location methods become unfeasible, so it will be necessary to develop a navigation algorithm accurate and feasible for this type of environments.
- Given the simultaneous movement of people and other vehicles, the AGV must be able to detect and avoid possible obstacles in order to ensure safe movement. It is a new challenge because it will be necessary to predict, detect and recognize moving obstacles.
- In some areas the AGV will have to circulate at higher speeds, so developing a security algorithm that responds in real time is critical.
- As an electric and rechargeable vehicle, concerns on battery charge management, energy consumption management and charging periods should be taken into account in this dissertation.

Since the fulfilment of all the requirements and systems necessary for the control and supervision of an AGV was impossible to achieve taking into account the time allocated for the development of this dissertation, only the following topics will be developed:

- Modelling and analysis of the powertrain
- Study of a reliable navigation system

1.3 Motivation

The motivations for the development of this project are related to environmental issues. With the increase in pollutant gas emissions from vehicles and with the drastic consequences for the environment already known to all, the development of vehicles with minimum energy consumption is fundamental for a more sustainable future. The aim is to develop an AGV control algorithm that minimises consumption as much as possible. The other issue is related to the optimization of intra-logistic processes. AGVs is a fundamental part for the optimisation of these processes, and in an industry 4.0 context, they increase the flexibility and automation of a company. Therefore, it is desired that this AGV is able to meet the production needs of this industry by quickly and safely transporting the goods needed for manufacturing.

Chapter 2

Literature Review

2.1 Introduction

In this chapter will be presented what technologies and standards are associated with AGVs. This will start with a historical review of the evolution of this type of vehicle, as well as what functions and technologies have been acquired over the years. Then, its applications will be studied, particularly in automotive industries, and the technologies and safety standards that exist today will be addressed. Finally, though the focus of this dissertation is the powertrain simulation and the study of a reliable navigation system, this chapter will address other topics that are important for the general understanding of what the control of an AGV involves.

2.2 The evolution of AGVs

According to [28], AGVs have been a key player for the industries since the middle of the last century, after the end of World War II. Motivated by the world economy booming, with the rapid development of sensory and regulatory technology and the dream of self-driving robots doing the work of humans, the first developments of these vehicles have emerged. With the evolution of technologies and new ways of manufacturing, AGVs have taken new functions as well as new sensors and performances. Thus, the history of AGVs can be divided into four eras. Each one represents the state of technology available and the emotional attitude towards the systems.

2.2.1 The First Era

In 1953, A.M. Barrett Jr., owner of Barrett Electronics, launched the "Guide-O-Matic", a modified towing tractor reconfigured to follow an overhead wire in a grocery warehouse [35], being considered the first AGV in history (Figure 2.1). Then, in 1954, the first AGV was installed at Mercury Motor Company in Columbia for long-distance round-trip consignment shipping. This vehicle was an innovation of track-guided because now they now followed an electrically conductive strip which was mounted on the floor. Nowadays, this principle is known as inductive track guidance [28]. Only in the middle of 1960s, the first systems for individual transportation were used to

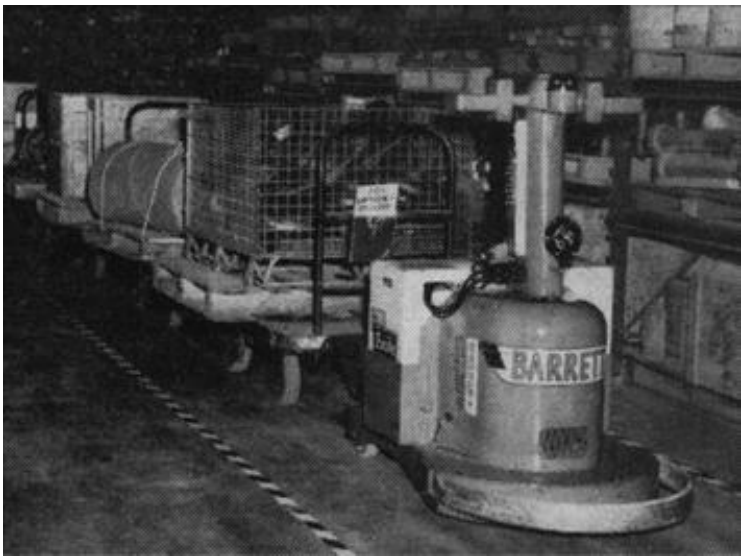

Figure 2.1: First AGV [1]

interconnect workplaces as well as the first systems were installed in good commissioning in food industry.

Some of the characteristics of these vehicles are as follows [28]:

- Simple electric magnetic sensor systems
- No flexibility - practically only one possible direction
- Working operations and employees had to be protected
- Vehicle guidance initially based on vacuum tubes
- Personnel protection was provided by bumper or safety bar equipped with "tactile sensor"
- Track guidance based on electrified conductors on the all floor or optical guiding strips.

2.2.2 The Second Era

The years 1970 to 1990 were marked by revolutionary technological inventions. In 1970's some developments that influenced AGVs appeared on the market [28]:

- PLC came to use and improvements in sensor technologies improve precision during driving, navigation and at the goods transfers station.
- Improvements on battery systems. Battery charging was introduced.
- Active inducted track guidance became the standard. The vehicle control was based on the block section control system used in railroads.

- AGV were fully integrated into production processes making possible to use the vehicles as workbenches.
- Infrared and radio signals were used for data transfer.

Market demand was driven primarily by the automotive industry [28]. Demand for cars has boomed and industries have been forced to look for solutions to improve productivity, reduce waste and lower the cost of production. Thus, many factories were modernized during the 1980's, with more and better machines enhancing worker's output [36]. As part of this objective, the AGVs have played an important role in some of the following applications [28]:

- Taxi operators for "pit-stop field assembly"
- AGVs as mobile workplaces in pre-assembly
- Interlinking of production machines in component manufacturing
- Tractors, piggyback and forklift vehicles to supply production lines
- In the warehouse, for commissioning and delivering materials to the lines
- Special equipment for integration into manufacturing systems.

However, at the end of 1980's, the automotive industry suffered a recession and, although innovative and responsible for increasing flexibility in some areas, AGVs were still expensive and the desired degree of flexibility was not always achieved, so after this reception the investment in these vehicles stagnate [28].

2.2.3 The Third Era

This era experienced the technological advances of the late 1990s and the first decade of this century. With the evolution of computers and microelectronics, new forms of communication as well as the speed and amount of data that became possible to process in such a short time, opened new horizons.

Electronic guidance and contact-free sensors have earned their position in the market and industry and are controlled by a standard PC while AGV normally contains a microprocessor. The classic "free" navigation technologies are magnetic and laser navigation taking the conductive cable guidance to its disuse. WLAN has established itself as a means of data transfer [28].

These improvements have had an impact on the way that developments in vehicle and controlling technology. Some of the areas with developments were [28]:

- Vehicles with higher speeds during the performance of their tasks thanks to improved sensory technology
- Cost reduction thanks to simpler and less expensive solutions;

- Alternative energy concepts with inductive transmission;
- Magnet point, laser, transponder, building navigation were developed;
- PC responsible for control and as part of intelligent sensory technology;
- WLAN was the main data transmission technology;
- Serving a bulk-storage warehouse, commissioning, lean production or hospitals have started to be part of the areas of application of the AGVs.

2.2.4 The Fourth Era

The latter Era is related to the present new industrial revolution, also known as Industry 4.0. The industrial landscape has changed, from which the products become the decision agents for the actions to be carried out. This is possible thanks to the IoT, where technologies aim to enhance the communication between systems and better manage facilities inside factories [34]. Another important aspect to mention is the efforts concerning the decarbonisation of the planet, which has motivated the development of electric or hybrid vehicles. Thus, good energy management and flexibility are two important factors to take into account in order to optimize industrial processes.

Is in this context that AGVs are passing through a new revolution. Up to now, the AGV simply follows pre-programmed procedures [28]. The AGV guidance technology is based on fixed or free route methods. Fixed route methods, such as magnetic tape, thought they provide accurate positioning and are inexpensive, they are not flexible as any changes would require re-taping which requires a high maintenance cost [34]. The free route methods provide more flexibility, but they still have higher costs and are less reliable and accurate [34].

One of the key factors for the robustness of AGVs is the integration of navigation and safety. Today's AGVs navigate until the personnel safety sensor is activated and the order to stop is given [28]. Although safe, this process is only compatible for places where there are instructed people, with fairly limited travel speeds, usually the speed of a person walking. Nevertheless, today's industry and with the development of technologies a new challenge arises: not the ability to only meet safety requirements when stopping as soon as an obstacle is detected, but rather to develop methods capable of predicting and recognising, so as to allow self-making-decision to stop, get around the obstacle or brake without the emergency stop activated by on-board sensors. Another issue concerns external transport. For logistical reasons, it is increasingly necessary to automate transport between warehouses in order to maximise productivity without requiring workers to transport goods by vehicle. Thus, the need to develop outdoor AGVs increases, but changing environment conditions in outdoor scenarios state additional challenges to a safe sensing of the environment [23]. On the other hand, outdoor circulation requires higher speeds and the presence of pedestrians or other vehicles in the same traffic area increases the degree of safety to be taken into account: predict, detect, recognize and avoid moving obstacles [23]. For this, and for higher speeds, it is necessary to develop an algorithm that can respond in real time, which makes this a new challenge, since the current sensors still require a high amount of data to process or are

very sensitive to variations in weather conditions with those presented in the first chapter of this document.

Therefore, this Era will be marked by the decentralisation of the control of these vehicles, which will be carried out by each one independently, increasing their flexibility. However, and allied to the still limitations at sensor level, it will also be necessary to decentralize the security algorithm of these vehicles, so that current proposals point to the combination of more than one type of sensor and some fixed, that is, installed in the plant in order to track possible obstacles or correction of the AGV positioning. This also represents that each sensor will have to communicate with the others, being this concept inserted in the so-called IoT.

2.3 Applications

2.3.1 AGV categories

Based on [28], the following table summarizes the categories and their characteristics of an AGV:

Table 2.1: Categories of Automated Guided Vehicle [28]

No.	Category	Load Type	Description
1	Forklift AGV (specially designed)	Pallet	Conceived, designed and produced by AGVS manufacturers; Floor-level load pickup; Various heights; Standard or special pallets or other fork compatible Containers; Stackable; Typical payload: 1t.
2	Forklift AGV (as automated serial vehicle)	Pallet	A serial product from a forklif manufacter is used and automated by AGVs manufactors; Similar to No. 1.
3	Piggyback AGV	Pallet	Limited transfer heights; Side load pickup using roller tracks or chain conveyor; Typical payload: 1t.
4	Towing vehicle	Trailer	Also known as "Tugger"; Pulls multiple trailers; Typical weight of trailers: 5t.
5	Underride AGV	Roller container	It underrides the roller container, and lifts is for transport; The standard AGV in hopital logistics; Typical payload: 0.5t.
6	Assembly AGV	Assembly object	Use in serial assembly, a substructure holds the pickup for the assembly object. Typical payload: up to 1t.
7	Heavy load AGV	Rolls, coils (paper or metal)	Transporting heavy paper rolls or steel coils (up to 35t).
8	Mini-AGV	SLC	Use in large fleets.
9	PeopleMover	Passengers	Similar to small or large buses.
10	Diesel AGV	Diverse	Outdoor vehicles (diesel-electric or diesel-hydraulic drive); Typical payload $\geq$ 3t.
11	Special AGV	Diverse	Special solutions for special tasks.

2.3.2 AGVs in Automotive and Auto Components industries

2.3.2.1 BMW New Leipzig Plant

This plant was used for the production of the BMW 300 series (E90) in 2005. For the first time, an automated guided vehicle system took over extensive logistics function in the area of parts supply [28]. In order to optimise and organise the production processes, the following standard processes have been created for the supply of parts to the assembly area at the Leipzig plant [28]:

1. Large and simple parts are delivery by truck to direct vicinity of their assembly areas (Direct delivery by truck);

2. Large and complex aggregates are assembled directly at the plant sit by external suppliers or BMW employees (Module delivery by overhead monorail);

3. AGVS commissioned and brought the parts to their respective assembly sites in the assembly area, most of which were stored in a staging area (Warehouse goods via AGVs);

The entire route layout is 14.5 km long with around 400 load pick-up and dropoff stations [28]. The vehicles do not exceed 1.2m/s in the main direction of the movement and the reverse movement only took place for positioning, no faster than 0.3 m/s, and giving off an acoustic warning signal [28]. Personnel protection and obstacles recognition is performed by a laser scanner and the assembly area was to be kept free of stacked materials to ensure quality and operating safety [28].

The type of navigation used is free navigation based on a combined principle of taking bearings and dead reckoning. Dead reckoning consists of measuring wheel and fiber-optic gyroscope which determine the path traveled and bearings are taken every five meters [28]. To achieve this, over 3000 small permanent magnets are set into the floor at this interval for the entire layout [28]. This process is also known as magnet navigation and has advantages that lie in its reliability and flexibility [28].

2.3.2.2 Denso in the Czech Republic

Denso Manufacturing is an international company producing air conditioning units for automotive industry based in Liberec. In order to improve the production efficiency, two Linde P30C towing tractors with trailer capacity of max. 3000kg [28]. The vehicles don't require AGV guindance control and are inductively guide along an induction path milled into the floor [28].

These vehicles have an important requirement: the tractor could be manually operated when necessary and eight production lines are served by two vehicles where a towing tractor can go through up to twenty cycles per shift [28]. As the AGV can be controlled manually, it is possible to drive outside the closed system by pressing a terminal key at the bottom, and thus switching from automatic to manual [28].

2.3.2.3 SEAT's Martorell plant

With the aim of becoming a more sustainable and intelligent factory, SEAT's Martorell plant introduced eight automated guided vehicles. Each vehicle and its carriages have a maximum transport capacity of 10 tonnes and cover a 3.5 kilometres route. At the moment, there are already two operational routes between the press and the body shops, where side parts of the vehicle and moving elements, such as hatches and doors, are delivered, which reduces with the transport of trucks between these workshops [37]. At the end of the day, the eight AGVS travel 240 km. These routes are external, making SEAT the first European industrial manufacturer to have AGVS in outdoor areas.

For navigation, these vehicles use SLAM navigation (simultaneous localisation and mapping), becoming the firts outdoor AGV without magnetic guidance. These vehicle are able to communicate with their surroundings and regulate traffic thanks to 4G technology and travel at a speed of 1m/s, so they are able to come to a complete half in front of any object or person within a radius of on and a half metres [38].

Another interesting feature in these AGVs is induction electric battery charging, without the need of cables. Theire battery is fully charged in 15 minutes while they are stopped to load parts onto them [38]. According to SEAT, these features allows a reduction of 1.5 tons of CO_2 per year.

2.4 Technologies and safety standards

2.4.1 Sensors for Perception and Localisation

As referenced in the previous section, today's AGVs have achieved a level of autonomy and flexibility that promises to revolutionise the industry among other applications. However, to guarantee the autonomy of these vehicles, it is not only necessary to develop accurate location methods, but these vehicles should perceive accurately its surroundings [2], especially in outdoor environments, where the perception of neighbouring vehicles, pedestrians, possible animal crossings, buildings or trees, among others, is fundamental to ensure safe navigation. Thus, in day-to-day is not possible to disassociate safety and navigation.

Up to now, these AGVs follows a physical or virtual path until a separate safety system orders it to stop [28], but, the goal for the new generation of AGVs is to characterize the obstacles attentively so that only for imminent emergency situations the on-board emergency sensors order the vehicle to stop.

For outdoor navigation, methods based on GNSS (Global Navigation Satellite Systems), being the GPS (Global Positioning System) the most known, are well-known and used. Recently, Simultaneous Localisation and Mapping (SLAM) methods are increasingly being studied since can provide high accuracy positioning and creates a 2-D or 3-D image of the surroundings. However, these processes require greater computational capabilities, leading to real-time response issues, specially for high-speed vehicles [28]. For sensing the surrounding environment and objects there are available sensors such as sonar, radar, Light Detection And Ranging (LIDAR) and cameras

[2]. Sonar, radar and lidar are active sensors because they emit energy in the form of sound or electromagnetic waves and measure the return to map the surrounding environment [2]. On the other hand, cameras are considered passive sensors since they do not emit energy or only measure light/electromagnetic waves in the environment [2].

According to [2], sonar measures distance to nearby objects but has a very limited range and low angular resolution. Radars rely on reflection of radio waves that they emit to measure distance to and speed of moving objects, but may suffer from interference from other radars and create false alarms. Lidar emit laser (infrared light) at wavelengths at typical scan frequency of 10-15kHz. Through the emission of millions pulses per second lidar can provide high resolution, a large field of view, and the capability to create a 3-D point cloud of surrounding environment. However, it is not possible to measure the speed and is sensitive to different environments conditions. Both radar and lidar also are weak in detecting very near objects where sonar performs well [2]. Cameras provide high field of vision and high resolution. Nevertheless, camera vision demands more computational resources than lidar.

The figure 2.2 presents the comparison between these senors technologies:

	Sonar	Radar	Lidar	Single vision camera
Perceived Energy	Sound waves	Millimeter wave radio signal	600–1000 nanometer wave laser signal	Visible light
Range [m]	2–5	0.15–250	2–100	250
Vehicle recognition versus other objects	Tracking	Tracking	Spatial segmentation, motion	Appearance, motion
Resolution	–	o	+	++
Field of view	–	+ (short range radar)- (long range radar)	++	++
Distance measurement	+	++	++	–
Velocity measurement	−−	++	+	–
Operation in poor weather	++	++	o	–
Poor lighting performance	++	++	++	−−
Other challenges	Poor classification low range low resolution	Poor classification, poor pedestrian detection, poor static object detection, prone to interference	Poor classification compared to vision, difficulty with highly reflective objects	high computational cost
Cost (US $)	50	50–200	7,000–70,000	100–200

++Very good +good o average – poor −−very poor

Figure 2.2: Comparison of different extroceptive sensor technologies [2]

2.4.2 AGV safety and legislation

In Europe, the Machinery Directive, establishes the necessary tasks for new machines to meet essential health and safety requirements [39]. The standards harmonized under MD are grouped into three types [39] [40]:

- **A-type:** specify basic concepts, terminology and design principles applicable to all categories of machinery.
- **B-type:** deal specific aspects of machinery safety or specific types of safeguard that can be used across a wide range of categories of machinery. Application of the specifications of B-type standards confers a presumption of conformity with the essential health and safety requirements of the Machinery Directive that they cover when a C-type standard or the manufacturer's risk assessment shows that a technical solution specified by the B-type standard is adequate for the particular category or model of machinery concerned.
- **C-type:** contain the safety requirements for a specific machine or a type of machine. If a Type-C standard exists, it has priority over the Type-A and Type-B standards. Nevertheless C-type standards may refer to A or B-type standards, indicating which of the specifications of the A or B-type standard are applicable to the category of machinery concerned.

For mobile automation, EN 1525:1997 is the only standard that has been available in Europe in the past. However, it was only listed for presumption of conformity for the old Directive (98/37/EC) and never for the current one (2006/42/EC). For this reason, there has never been a harmonised Type-C standard for AGVs [39]. Recently, the EN ISO 3691-4 was developed, though not listed in the e Official EU Journal. This means that EN has remained the unique standard for these vehicles since 1997, which represents a problem because this standard no longer addresses the current state of the art technology and is also not harmonized with the Machinery Directive [41].

In accordance with the legislation, some technical safety features to take into account in an AGV are [28]:

- An emergency stop switch easily recognizable to everyone and accessible. If the emergency is activated, the vehicle stops immediately.
- A combination of optical and acoustic warnings signals, including blinkers to indicate a change of direction (with acoustic support).
- Mechanical, independently operating brakes ensure proper stopping. The brakes must be designed so that they can stop the AGV even with a maximum payload and also at maximum incline of the drive path (slope).
- Personnel protection system which has to ensure that people or objects are reliably recognized. The vehicle has to safely come to a stop before persons or objects are injured or damaged.

For personnel protection, on of the most used is non-contacting laser scanners, of which the leading manufacturer is SICK. Recently, the outdoorScan3 has been introduced to the market, a safety laser scanner for outdoor automation certified in accordance with ISO 13849 and IEC 62998 for protection of persons for indoor and outdoor use.

2.5 Electric Vehicle Powertrain

The figure 2.3 shows a diagram schematising a powertrain of an electric vehicle, whose arrows between the blocks indicate the direction and which variables are associated in the communication or transfer of energy between blocks.

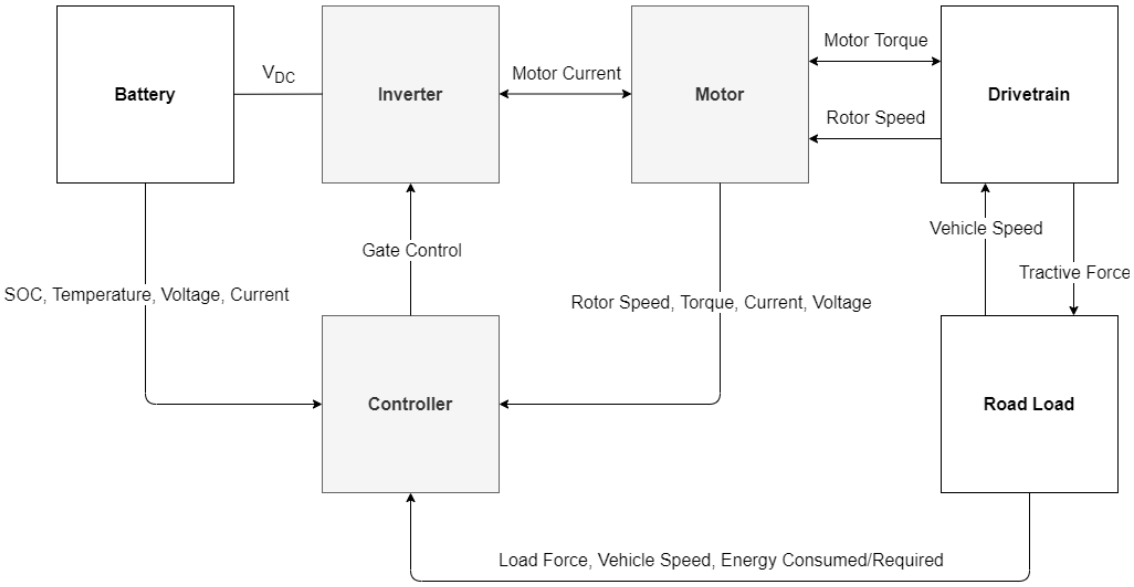

Figure 2.3: Powertrain diagram

The main element of a powertrain is the electric motor, since it is the responsible for the transformation of electrical energy into mechanical energy, i.e., a device capable of generating torque needed to move the wheels of a vehicle. To feed it, a voltage source is required and, given that batteries can be seen as DC sources and the motor studied in this dissertation is an AC machine, it is necessary to convert the DC power into AC power, performed through the inverter (AC/DC converter). The inverter is controlled by a controller responsible for measuring and estimating important variables for the motor operation and having as output control signals to the inverter. The load applied to the motor can be represented as torque or speed on the motor shaft since it is a rotating load. However, the torque applied to the wheels as well as the direction of rotation of the latter must be ensured by the drivetrain, consisting, inter alia, of a reduction gearbox and other mechanical devices that ensure the correct application of force and direction of rotation on the vehicle wheels. To better model the load torque to which the motor will be subjected, a model of forces acting on road vehicles will be studied. In the case of batteries,

they are of great importance in supervision and energy optimisation algorithms, as the autonomy of a vehicle depends mainly on them, and it is also necessary to ensure that the voltage at their terminals (among others) is what is required for the correct operation of the engine. On the other hand, they are responsible for energy storage, which can come from normal charging or electrical regeneration techniques, such as regenerative braking.

After an overview of the different elements that characterise a powertrain, in the next subsections these will be studied in detail. Since the motor is seen as the main element of a powertrain, this analysis will start by studying mathematical transformations and models of an AC motor, followed by the inverter characteristics and the different control methods. Afterwards a mathematical model of a battery will be discussed, and finally the vehicle equations, including the model of the forces acting on the road vehicles.

2.5.1 Clarke and Park Transforms

Clarke and Park transforms are essential for vector control of AC machines. These consist of mathematical transformations that allow the decomposition of a three-phase system into only two components. Whereas Clarke transform performs the conversion of stationary quantities (*abc* - of a three-phase system) into a two-phase orthogonal system ($\alpha\beta$), Park transform converts the two components in the $\alpha\beta$ frame to an orthogonal rotating reference frame (dq) [42] [43]. The figure 2.4 shows the reference frames presented so far and will serve as a support for the theoretical development of these two transforms. These are also presented in the form of current vectors, but these transforms apply to other electrical variables, such as voltage.

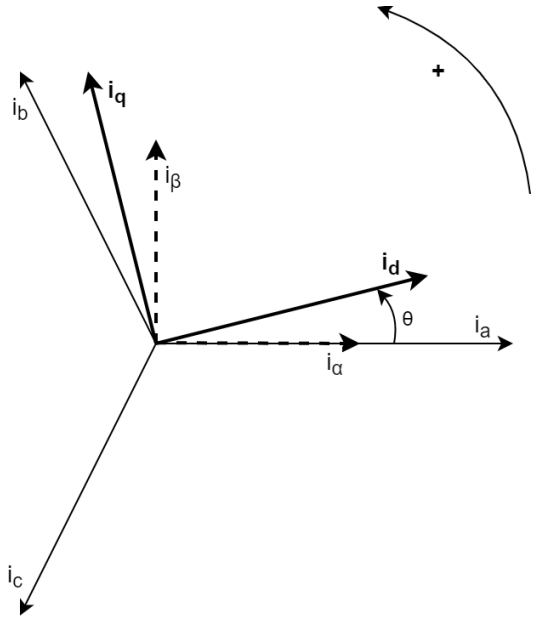

Figure 2.4: Representation of three-phase system (*abc*) and two-phase orthogonal system reference frames (stationary ($\alpha\beta$) and rotational(dq))

2.5.1.1 Clarke Transform

As already stated, Clarke transform converts quantities of a three-phase system into two in an orthogonal system, being known as Direct Clarke Transform. However, this transform can be used in its inverse form, transforming two quantities of an orthogonal system into three of a three-phase system: Inverse Clarke Transform. Thus, the matrix representations of the Direct and Inverse Clarke transform are as follows, respectively [44][45]:

$$\begin{bmatrix} i_\alpha \\ i_\beta \\ i_0 \end{bmatrix} = \frac{2}{3} \cdot \begin{bmatrix} 1 & -\frac{1}{2} & -\frac{1}{2} \\ 0 & \frac{\sqrt{3}}{2} & -\frac{\sqrt{3}}{2} \\ \frac{1}{2} & \frac{1}{2} & \frac{1}{2} \end{bmatrix} \cdot \begin{bmatrix} i_a \\ i_b \\ i_c \end{bmatrix} \tag{2.1}$$

$$\begin{bmatrix} i_a \\ i_b \\ i_c \end{bmatrix} = \begin{bmatrix} 1 & 0 & 1 \\ -\frac{1}{2} & \frac{\sqrt{3}}{2} & 1 \\ -\frac{1}{2} & -\frac{\sqrt{3}}{2} & 1 \end{bmatrix} \cdot \begin{bmatrix} i_\alpha \\ i_\beta \\ i_0 \end{bmatrix} \tag{2.2}$$

where i_a, i_b and i_c are quantities in a three-phase system (abc), i_α and i_β are quantities in an orthogonal stationary reference frame ($\alpha\beta$) and i_0 is the homopolar component of the system. However, in balanced three-phase systems the following relation can be obtained:

$$i_a + i_b + i_c = 0 \tag{2.3}$$

In this way, it is possible to reduce the costs related to measurement, since the third phase can be calculated as a function of the first two, reducing the number of sensors required:

$$i_c = -i_a - i_b \tag{2.4}$$

Thus, the Clarke transform can also be simplified, being the Direct and Inverse forms of this transform written as follows, respectively [44][45]:

$$\begin{bmatrix} i_\alpha \\ i_\beta \end{bmatrix} = \begin{bmatrix} 1 & 0 \\ \frac{1}{\sqrt{3}} & \frac{2}{\sqrt{3}} \end{bmatrix} \cdot \begin{bmatrix} i_a \\ i_b \end{bmatrix} \tag{2.5}$$

$$\begin{bmatrix} i_a \\ i_b \\ i_c \end{bmatrix} = \begin{bmatrix} 1 & 0 \\ -\frac{1}{2} & \frac{\sqrt{3}}{2} \\ -\frac{1}{2} & -\frac{\sqrt{3}}{2} \end{bmatrix} \cdot \begin{bmatrix} i_\alpha \\ i_\beta \end{bmatrix} \tag{2.6}$$

Furthermore, and assuming the orthogonality of the two components, three vectors associated with the three phases of a three-phase system can be represented by a single vector, whose amplitude is calculated as follows:

$$|i| = \sqrt{i_\alpha^2 + i_\beta^2} \tag{2.7}$$

2.5.1.2 Park Transform

After simplification of the three-phase system (abc) in an orthogonal two-phase system ($\alpha\beta$), there remains a problem that makes it impossible to use traditional control methods, such as PI or PID controllers, to control variables associated with AC machines: this two-phase system frame is still stationary, so the variables represented in this referential ($\alpha\beta$) are seen as sinusoids. To overcome this problem, the use of a rotational orthogonal two-phase system, whose frequency of rotation around the origin is the same as the frequency of sinusoidal perturbations of the variables in $\alpha\beta$ system, will allow the conversion of these variables into continuous variables in dq referential. This transformation ($\alpha\beta$ system to dq system) is performed through Park Transform. Thus, in the Park Transform, it is essential to obtain the angle between the α-axis and the d-axis (or q-axis) in real time and as accurately as possible. This angle represents the angular position of the dq reference frame with respect to α-axis [46].

Depending on the initial alignment of the referential dq, that is, at time $t = 0^{+}s$, the d-axis is aligned with the α-axis, or the q-axis is aligned with the alpha-axis, the Park Transform can be written as follows, where the first represents the alignment of d-axis with α-axis, and the second the alignment of q-axis with α-axis [46]:

$$\begin{bmatrix} i_d \\ i_q \end{bmatrix} = \begin{bmatrix} \cos\theta & \sin\theta \\ -\sin\theta & \cos\theta \end{bmatrix} \cdot \begin{bmatrix} i_\alpha \\ i_\beta \end{bmatrix} \tag{2.8}$$

$$\begin{bmatrix} i_d \\ i_q \end{bmatrix} = \begin{bmatrix} \sin\theta & -\cos\theta \\ \cos\theta & \sin\theta \end{bmatrix} \cdot \begin{bmatrix} i_\alpha \\ i_\beta \end{bmatrix} \tag{2.9}$$

Similar to the Clarke Transform, this transform can also be used in its inverse form, transforming quantities in the dq system into quantities in the $\alpha\beta$ system. Therefore, depending on the initial alignment, the Inverse Park Transform can be written in the following forms,where the first represents the alignment of d-axis with α-axis, and the second the alignment of q-axis with α-axis [47]:

$$\begin{bmatrix} i_\alpha \\ i_\beta \end{bmatrix} = \begin{bmatrix} \cos\theta & -\sin\theta \\ \sin\theta & \cos\theta \end{bmatrix} \cdot \begin{bmatrix} i_d \\ i_q \end{bmatrix} \tag{2.10}$$

$$\begin{bmatrix} i_\alpha \\ i_\beta \end{bmatrix} = \begin{bmatrix} \sin\theta & \cos\theta \\ -\cos\theta & \sin\theta \end{bmatrix} \cdot \begin{bmatrix} i_d \\ i_q \end{bmatrix} \tag{2.11}$$

Finally, similar to what is done in the $\alpha\beta$ referential, it is possible to deduce the following:

$$|i| = \sqrt{i_d^2 + i_q^2} \tag{2.12}$$

2.5.2 Induction motor modelling

An induction motor can be modelled using its per phase model, although this is not the most suitable for vector control algorithms given the complexity associated with any three-phase system.

However, a three-phase system can be simplified, as just discussed, so a motor can be modelled using an $\alpha\beta$ model or a dq model. These two referential frames allow to use the vector control by reducing the number of phases to two, and as the phases are in quadrature in these two references frames, it is possible to separate motor variables (e.g. current or voltage) into two components: α and β ($\alpha\beta$ model) or the torque component and the magnetization component (dq model).

2.5.2.1 $\alpha\beta$ model

Considering a Squirrel-Cage Machine and the symmetrically of the motor model, with a linear magnetic circuit characteristic [48], the motor differential equations are (model based on [49][48]):

$$u_{s\alpha} = R_s i_{s\alpha} + \frac{d}{dt}\psi_{s\alpha} \tag{2.13}$$

$$u_{s\beta} = R_s i_{s\beta} + \frac{d}{dt}\psi_{s\beta} \tag{2.14}$$

$$u_{r\alpha} = 0 = R_r i_{r\alpha} + \frac{d}{dt}\psi_{r\alpha} + \omega_r \psi_{r\alpha} \tag{2.15}$$

$$u_{r\beta} = 0 = R_r i_{r\beta} + \frac{d}{dt}\psi_{r\beta} + \omega_r \psi_{r\beta} \tag{2.16}$$

$$\psi_{s\alpha} = L_s i_{s\alpha} + L_m i_{r\alpha} \tag{2.17}$$

$$\psi_{s\beta} = L_s i_{s\beta} + L_m i_{r\beta} \tag{2.18}$$

$$\psi_{r\alpha} = L_r i_{r\alpha} + L_m i_{s\alpha} \tag{2.19}$$

$$\psi_{r\beta} = L_r i_{r\beta} + L_m i_{s\beta} \tag{2.20}$$

The electromagnetic torque can be calculated as function of stator magnetic fluxes and stator currents:

$$T_e = \frac{3}{2} p(\psi_{s\alpha} i_{s\beta} - \psi_{s\beta} i_{s\alpha}) \tag{2.21}$$

The equations 2.13, 2.14 can be written in another way in order to estimate the stator magnetic fluxes [49]:

$$\psi_{s\alpha} = \int u_{s\alpha} - R_s i_{s\alpha}\, dt \tag{2.22}$$

$$\psi_{s\beta} = \int u_{s\beta} - R_s i_{s\beta}\, dt \tag{2.23}$$

$$|\psi_s| = \sqrt{\psi_{s\alpha}^2 + \psi_{s\beta}^2} \tag{2.24}$$

Taking advantage of the fact that the β component is in quadrature with α, the stator flux angle can be obtained as follow:

$$\cos\theta_e = \frac{\psi_{s\alpha}}{|\psi_s|} \tag{2.25}$$

$$\sin\theta_e = \frac{\psi_{s\beta}}{|\psi_s|} \tag{2.26}$$

$$\theta_e = \arctan\frac{\psi_{s\beta}}{|\psi_{s\alpha}|} \tag{2.27}$$

Thus, the synchronous angular speed can be estimated through the variation in time of the stator flux angle:

$$\omega_e = \frac{d\theta}{dt} = \frac{(u_{s\beta} - R_s i_{s\beta})u_{s\alpha} - (u_{s\alpha} - R_s i_{s\alpha})u_{s\beta}}{\psi_{s\alpha}^2 + \psi_{s\beta}^2} \tag{2.28}$$

Since the synchronous speed in an induction motor is not the same as the rotor speed, it will be necessary to estimate the slip speed, which, according to [49], can be calculated as follows:

$$\omega_{sl} = K_s T_e \tag{2.29}$$

where k_s was defined as the ratio of rated slip frequency/rated torque. Thus, the rotor speed is obtained subtracting the slip angular speed from the synchronous speed:

$$\omega_r = \omega_e - \omega_{sl} \tag{2.30}$$

The next table summarises and characterises the variables used in the previously presented equations and is valid for the following subsections:

Table 2.2: Motor parameters

Parameters	Definition	Units
$\alpha\beta$	Stator orthogonal coordinate system	—
p	Pole pairs	—
$u_{s\alpha,\beta}$	Stator voltages	V
$u_{r\alpha,\beta}$	Rotor voltages	V
$i_{s\alpha,\beta}$	Stator currents	A
$i_{r\alpha,\beta}$	Rotor currents	A
$\psi_{s\alpha,\beta}$	Stator magntic fluxes	Wb or Vs
$\psi_{r\alpha,\beta}$	Rotor magntic fluxes	Wb or Vs
R_s	Stator resistance	Ω
R_r	Rotor resistance	Ω
L_{ls}	Stator self-inductance	H
L_{lr}	Rotor self-inductance	H
L_m	Mutual inductance	H
$L_s = L_m + L_{ls}$	Stator inductance	H
$L_r = L_m + L_{lr}$	Rotor inductance	H
ω_m	Rotor angular speed	rad/s
$\omega_r = p\omega_m$	Electrical rotor angular speed	rad/s
ω_e	Synchronous angular speed	rad/s
ω_{sl}	Slip angular speed	rad/s
T_e	Motor electromagnetic torque	Nm

2.5.2.2 *dq* model

Moving now to the dq model (based on [48][49][50]), the equations describing the electrical behaviour of the motor can be written as follows:

$$u_{sd} = R_s i_{sd} + \frac{d}{dt}\psi_{sd} - \omega_e \psi_{sq} \tag{2.31}$$

$$u_{sq} = R_s i_{sq} + \frac{d}{dt}\psi_{sq} + \omega_e \psi_{sd} \tag{2.32}$$

$$u_{rd} = 0 = R_r i_{rd} + \frac{d}{dt}\psi_{rd} + (\omega_e - \omega_r)\psi_{rq} \tag{2.33}$$

$$u_{rq} = 0 = R_r i_{rq} + \frac{d}{dt}\psi_{rq} + (\omega_e - \omega_r)\psi_{rd} \tag{2.34}$$

$$\psi_{sd} = L_s i_{sd} + L_m i_{rd} \tag{2.35}$$

$$\psi_{sq} = L_s i_{sq} + L_m i_{rq} \tag{2.36}$$

$$\psi_{rd} = L_r i_{rd} + L_m i_{sd} \tag{2.37}$$

$$\psi_{rq} = L_r i_{rq} + L_m i_{sq} \tag{2.38}$$

The electromagnetic torque can be written in different ways, depending on the reference frame adopted and control method (which will be addressed below), by manipulating the equations of the motor model [50]. Thus, the electromagnetic torque can be expressed as:

$$T_e = \begin{cases} \frac{3}{2} p(i_{sq}\psi_{sd} - i_{sd}\psi_{sq}) \\ \frac{3L_m}{2} p(i_{sq} i_{rd} - i_{sd} i_{sq}) \\ \frac{3}{2}\frac{L_m}{L_r} p(i_{sq}\psi_{rd} - i_{sd}\psi_{rq}) \end{cases} \tag{2.39}$$

2.5.2.3 Mechanical Model

The motor is a machine capable of producing torque, having a load coupled to it, seen as a load torque and with influence on the inertia of the system, since loads with greater mass will consequently result in systems with higher inertia, being naturally dynamically slower. Taking these concepts into account, the equation that describes the mechanical behaviour of the motor is as follows:

$$J\frac{d}{dt}\omega_m = T_e - T_f - F\omega_m - T_L \tag{2.40}$$

where:

Table 2.3: Motor Mechanical parameters (adapted from [29])

Parameters	Definition	Units
J	Combined rotor and load inertia	kgm^2
F	Combined rotor and load viscous friction coefficient	$Nm/(rad/s)$
T_e	Electromagnetic Torque	Nm
T_L	Load Torque	Nm
T_f	Motor shaft static friction torque	Nm
ω_m	Rotor angular speed	rad/s

2.5.2.4 Torque-Slip characteristics

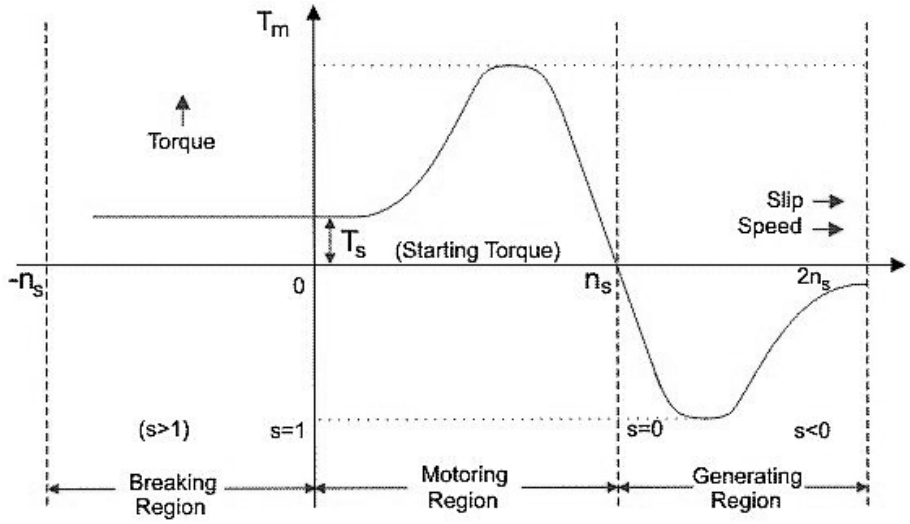

Figure 2.5: Torque-Slip curve of an induction machine (adapted from [3])

As can be observed in figure 2.5, an induction machine has three regions according to its torque-slip curve:

- Breaking region
- Motoring region
- Generating region

The motoring region is probably the most used and best known region. In this region, the torque varies from zero to the full load torque while the rotor speed is always bellow the synchronous speed. The slip is positive and the induction machine consumes electrical energy. If an external source causes the increasing of the rotor speed to the limit where it exceeds the synchronous speed, the torque and slip signal invert, turning both negatives. In this case, the induction machine operates as generator, converting mechanical energy into electrical energy which can be stored or delivered to the power grid. Finally, for braking, the known control methods reduce the stator frequency (f_s), thus reducing the synchronous speed (n_s) to values below the actual rotor speed (n_r). In this way, the electromagnetic torque and slip become negative, counteracting the movement of the rotor, causing its braking as well as the regeneration of electrical energy. To stop the movement, the frequency of the power supply is reduced to zero.

2.5.3 Three-phase Voltage Source Inverter

A VSI is electronic device which aims to output three-phase voltage source with controlled amplitude, frequency and phase [5]. This consists of three legs, one for each phase of the three-phase

system, where each of these legs consists of two switches, typically MOSFETs or IGBTs. The switches of any leg cannot be switched on simultaneously in order to avoid short circuit across the dc link voltage supply [51].

The follow figures show the schematic of a VSI, where S_n is equivalent to Q_n, representing each switch:

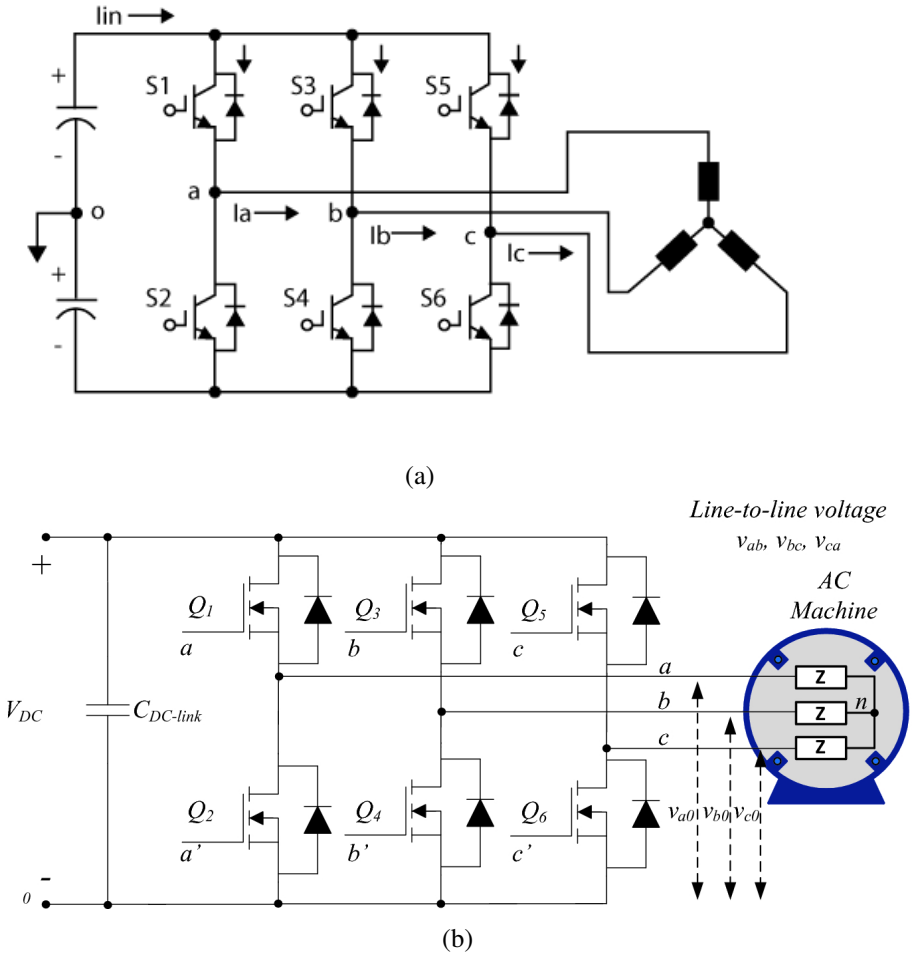

Figure 2.6: Three-Phase Voltage Source Inverter (2.6a: implemented with IGBTs, 2.6b: Implemented with MOSFETs) (adapted from [4][5])

During the VSI operation, the switches can generate eight different states of conduction. Each state describes the commutation of the switches on each leg, with the "ON" state indicating that the top switch is conducting, having logic value "1". While the top switch is active, the bottom switch remains open, having logic value "0" [5]. Of the eight valid states, six are named "active states" since produce non-zero AC output voltages [51]. The remaining two states occur when the top three switches are active simultaneously, or the bottom three, producing zero-line output voltage. These two states are known as "zero switching states".

However, given its operating mechanism based on the commutation of its switches, the output of this inverter will consequently have harmonic content, since its output will not be a pure sinusoid. The harmonic causes distortion on the output device and it leads to less desirable behaviour

in electrical machines such as motors. Higher harmonic content may cause higher torque ripple, which leads to faster degradation of the mechanical characteristics of the rotor. Thus, different modulation methods have been developed over time in order to reduce the harmonic content as well as a better use of the available DC bus voltage, among other characteristics such as frequency and amplitude of the output signal.

2.5.4 Modulation Techniques

Depending on its operation mood, a VSI can be classified into two types [52]:

- Stepped wave inverter
- Pulse Width Modulation inverter

According to [5], six-step modulation is the most basic three-phase voltage generator with variable-frequency. On the other hand, PWM techniques are based on the generation of variable-with pulses (through duty-cycle variation) to control frequency and/or amplitude of the output signal [53]. The pulses are delivered to the switches, thus controlling their opening and closing. For a high-amplitude signal, the switch is "ON" more of the time, for a low-amplitude signal if "OFF" more of the time [53]. PWM techniques are also the most used for voltage control because of its greater efficiency.

2.5.4.1 Six-Step Modulation

As stated on the previous subsection, a VSI has six active states. This method, which is described in [5], take advantages of this feature and outputs AC voltages by moving from one state to another, creating a sequence of states. As result, the output line voltages (V_{ab}, V_{bc} and V_{ca}) consist of discrete values of voltages: V_{DC}, 0 and $-V_{DC}$ [54]. If these states were assigned spatially, they are 60º (or $\pi/3$) apart, completing a circle [5]. Thus, to generate a complete period of the wave, an imaginary voltage vector is required, which go through all the vertices until complete 360º turn [5]. The output wave form frequency is defined by the speed with which a full turn is executed while the voltage amplitude remains unvaried [5].

The following figure shows the six active states spatially, according to the switching combination:

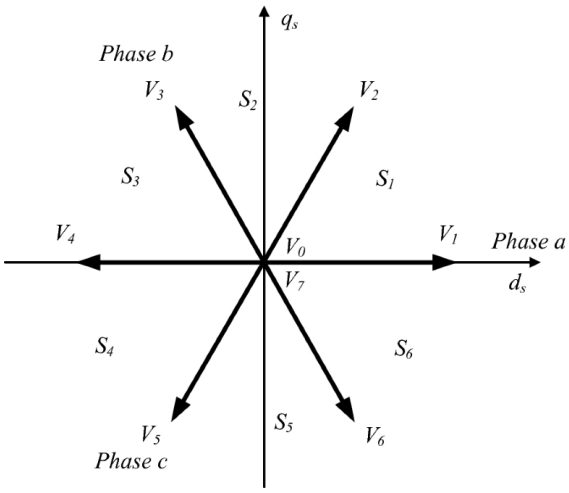

Figure 2.7: Spatial Vector Position [5]

For a better understanding of this modulation method, a table, based on figures 2.7 and 2.6, with the different switching states and the associated voltages (line-to-line and phase voltage) can be created:

Table 2.4: Switches active states with output voltages, line-to-line, and phase voltage (adapted from [5])

Vector	a-S_1	b-S_3	c-S_5	v_{an}	v_{bn}	v_{cn}	v_{ab}	v_{bc}	v_{ca}
V_0	0	0	0	0	0	0	0	0	0
V_1	1	0	0	$2V_{DC}/3$	$-V_{DC}/3$	$-V_{DC}/3$	V_{DC}	0	$-V_{DC}$
V_2	1	1	0	$V_{DC}/3$	$V_{DC}/3$	$-2V_{DC}/3$	0	V_{DC}	$-V_{DC}$
V_3	0	1	0	$-V_{DC}/3$	$2V_{DC}/3$	$-V_{DC}/3$	$-V_{DC}$	V_{DC}	0
V_4	0	1	1	$-2V_{DC}/3$	$V_{DC}/3$	$V_{DC}/3$	$-V_{DC}$	0	V_{DC}
V_5	0	0	1	$-V_{DC}/3$	$-V_{DC}/3$	$2V_{DC}/3$	0	$-V_{DC}$	V_{DC}
V_6	1	0	1	$V_{DC}/3$	$-2V_{DC}/3$	$V_{DC}/3$	V_{DC}	$-V_{DC}$	0
V_7	1	1	1	0	0	0	0	0	0

As can be observed from table 2.4, the six-step modulation allows the maximum utilization of DC-link voltage [5]. Also in [5], the peak value per phase of the output voltage as well as the RMS value of the line-to-line voltage are presented. The peak value per phase can be given by the first harmonic [5] as:

$$\hat{V}_{sixstep} = \frac{2V_{DC}}{\pi} \tag{2.41}$$

Thus, the line-to-line voltage is calculated as follows:

$$\hat{V}_{sixstep-abRMS} = \frac{\sqrt{3}}{\sqrt{2}}\frac{2V_{DC}}{\pi} = 0.78V_{DC} \tag{2.42}$$

The main advantage of this technique is that the RMS output voltage of VSI is 10% higher than the input RMS voltage [5]. However, the amplitude of the voltage cannot vary and the output voltage contains an important amount of harmonics, leading to less performance on the control of electric machines, more electromagnetic motor torque ripple, compromising the motor life-time [5].

2.5.4.2 Sinusoidal Pulse Width Modulation - SPWM

SPWM is one of the most popular PWM modulation techniques. In this technique, multiple pulses per half-cycle are generated, whose width is varied with respect to sine wave magnitude [52]. The PWM is generated by comparing two waveform: a control signal, also known as reference voltage or modulating signal, and a triangular wave - the carrier wave. In the case of a three-phase inverter, three control signals are required. The PWM frequency is defined by the frequency of the carrier signal (f_{carr}) and its amplitude (V_{carr}) remains constant, whereas the amplitude and frequency of VSI output is controlled by changing the amplitude and frequency of the control signal (V_c and f_c, respectively). The amplitude of the AC outuput voltage harmonics also depend on the amplitude modulation index [51], calculated as follows [52]:

$$m_a = \frac{controlsignalvoltage}{carriersignalvoltage} = \frac{V_c}{V_{carr}} \tag{2.43}$$

and the frequency modulation index is defined as: [52]:

$$m_f = \frac{PWM_{frequency}}{fundamentalfrequency} = \frac{f_s}{f_1} \tag{2.44}$$

for which, for $m_f > 9$, the amplitude of the AC output voltage harmonics depends entirely on the amplitude modulation index (m_a) [51]. According to [51], m_f should be an odd integer and a multiple of 3 for three-phase PWM inverter, in order to avoid harmonics at ouput voltage.

Since m_f is normally high, associated with high switching frequencies, that is, PWMs with frequencies much higher than those used in the control signal, SPWM moves the voltage harmonics components to higher frequencies [55]. However, over modulation ($m_a > 1$) causes loss of some intersections between the carrier and the modulating signal, generating low-order harmonics [51].

Thus, according to [55], the working principle of SPWM can be summarized as follows:

- The frequency of carrier wave defines the frequency of PWM
- Amplitude and frequency of control signal control the amplitude and frequency of the first harmonic of the output voltage
- PWM signal is created by comparing the control wave with carrier wave. Taking phase A as an example, the following relation can be obtained:
  - If $V_c > V_{carr}$ then $V_{ao} = V_{DC}/2$

– If $V_c < V_{carr}$ then $V_{ao} = -V_{DC}/2$

The modulation index can also be defined as function of maximum amplitude of the six-step modulation [5] as:

$$m' = \frac{V_{PWM}}{\hat{V}_{sixstep}} = \frac{V_{DC}/2}{2V_{DC}/\pi} = \frac{\pi}{4} = 78.55\% \tag{2.45}$$

Thus, it can be concluded that this technique relies on a poor use of voltage.

2.5.4.3 Space-Vector Pulse Width Modulation - SVPWM

The working principle of SVPWM is based on the reconstruction of the reference voltage vector v_{ref} which rotates in the counter clock wise direction [5] [55]. As stated in 2.5.4.1, the VSI has eight possible conduction states and six of them, the "active sates", can form a hexagon, as can be seen in the following figure:

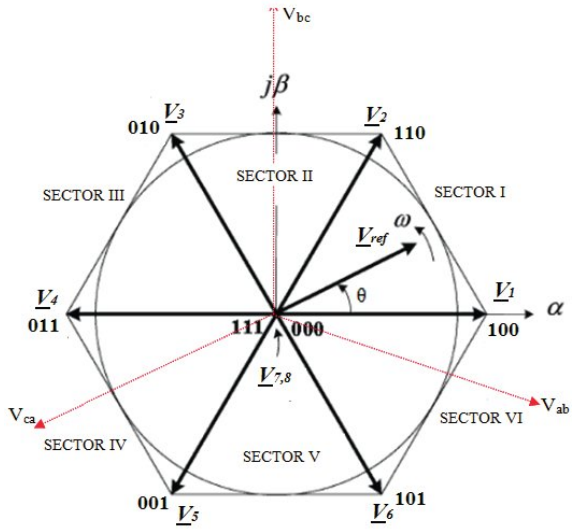

Figure 2.8: Space vector hexagon for two-level inverter [6]

Although in the figure 2.8 the hexagon is represented in the $\alpha\beta$ referential frame, V_{ref} can be represented by its orthogonal components either in $\alpha\beta$ or dqs axis transformation [5]. Its reconstruction is performed by its two adjacent vector components plus V_0 and/or V_7. To generate a sinusoidal voltage in the output of the VSI, V_{ref} is expected to pass through successive sectors I to VI one by one [6], where the rotation speed will fix the frequency, while the amplitude of the voltage will be fixed by the amplitude of its the components [5]. $V_7(a,b,c) = (1,1,1)$ and $V_0(a,b,c) = (0,0,0)$ serve to complete the PWM cycle [5].

The following picture shows the ways in which V_{ref} is reconstructed in sector I:

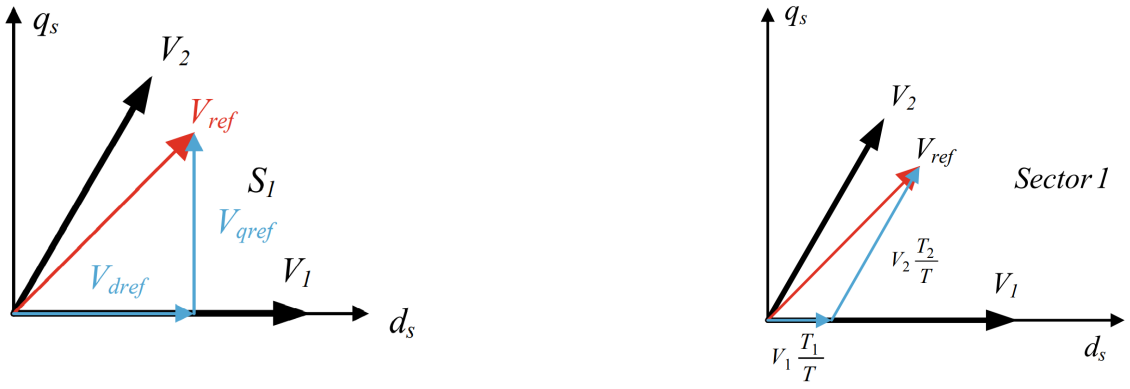

(a) (b)

Figure 2.9: Construction of V_{ref} (2.9a: by its dq components, 2.9b: by the nearest vectors of the hexagon (V_1 and V_2)) (adapted from [5])

Analysing the figures 2.8 and 2.9a, it can be concluded that the maximum amplitude of V_{ref}, in the linear zone of SVPWM, corresponds to the circle inscribed in hexagon, which radius is equal to $VDC/\sqrt{3}$ [5]. Thereby, two more columns can be added to table 2.4, with the amplitude of the orthogonal components of V_{ref} in the dq referential frame:

Table 2.5: Orthogonal voltages in dq referential frame of the eight switching states

Vector	V_{ds}	V_{qs}
V_0	0	0
V_1	$2V_{DC}/3$	0
V_2	$V_{DC}/3$	$V_{DC}/\sqrt{3}$
V_3	$-V_{DC}/3$	$V_{DC}/\sqrt{3}$
V_4	$-2V_{DC}/3$	0
V_5	$-V_{DC}/3$	$-V_{DC}/\sqrt{3}$
V_6	$V_{DC}/3$	$-V_{DC}/\sqrt{3}$
V_7	0	0

The modulation index, compared to the maximum amplitude of six-step ($\hat{V}_{sixstep}$), will have the value of:

$$m' = \frac{\hat{V}_{ref}}{\hat{V}_{sixstep}} = \frac{V_{DC}/\sqrt{3}}{2V_{DC}/\pi} = 0.907 \tag{2.46}$$

That is, 90.7% of the fundamental wave of the six-step modulation in the linear zone [5].

After understanding and analyzing the method and amplitude of the voltages by which V_{ref} is constructed, it is necessary to calculate the time which each nearest vector, and by sector, should be active. Once again, these calculations are presented in [5]. Thus, by analyzing the figure 2.9b, and based on [5], the linear combination of V_{ref} in the sector I can be obtained as follows:

$$\overline{V}_{ref} = \frac{T_1}{T}\overline{V}_1 + \frac{T_2}{T}\overline{V}_2 + \frac{T_0}{T}\overline{V}_0 + \frac{T_7}{T}\overline{V}_7 \tag{2.47}$$

and

$$T = T_1 + T_2 + T_0 + T_7 \tag{2.48}$$

where T_n corresponds to duration times of each state of the devices in sector I [5] and the sum of all these duration time is equal to the PWM period, T. The following table shows how these times can be calculated for each sector:

Table 2.6: Time calculation for each sector (from [5])

Sector I $0 \leq \omega \cdot t \leq \frac{\pi}{3}$	Sector II $\frac{\pi}{3} \leq \omega \cdot t \leq \frac{2\pi}{3}$	Sector III $\frac{2\pi}{3} \leq \omega \cdot t \leq \pi$
$T_1 = \frac{\sqrt{3}}{2} m' \cos(\omega \cdot t + \frac{\pi}{6})$ $T_2 = \frac{\sqrt{3}}{2} m' \cos(\omega \cdot t + \frac{3\pi}{2})$ $T_0 + T_7 = T - (T_1 + T_2)$	$T_2 = \frac{\sqrt{3}}{2} m' \cos(\omega \cdot t + \frac{11\pi}{6})$ $T_3 = \frac{\sqrt{3}}{2} m' \cos(\omega \cdot t + \frac{7\pi}{6})$ $T_0 + T_7 = T - (T_2 + T_3)$	$T_1 = \frac{\sqrt{3}}{2} m' \cos(\omega \cdot t + \frac{3\pi}{2})$ $T_1 = \frac{\sqrt{3}}{2} m' \cos(\omega \cdot t + \frac{5\pi}{6})$ $T_0 + T_7 = T - (T_3 + T_4)$
Sector IV $\pi \leq \omega \cdot t \leq \frac{4\pi}{3}$	**Sector V** $\frac{4\pi}{3} \leq \omega \cdot t \leq \frac{5\pi}{3}$	**Sector VI** $\frac{5\pi}{3} \leq \omega \cdot t \leq 2\pi$
$T_1 = \frac{\sqrt{3}}{2} m' \cos(\omega \cdot t + \frac{7\pi}{6})$ $T_2 = \frac{\sqrt{3}}{2} m' \cos(\omega \cdot t + \frac{\pi}{2})$ $T_0 + T_7 = T - (T_4 + T_5)$	$T_2 = \frac{\sqrt{3}}{2} m' \cos(\omega \cdot t + \frac{5\pi}{6})$ $T_3 = \frac{\sqrt{3}}{2} m' \cos(\omega \cdot t + \frac{\pi}{6})$ $T_0 + T_7 = T - (T_5 + T_6)$	$T_1 = \frac{\sqrt{3}}{2} m' \cos(\omega \cdot t + \frac{\pi}{2})$ $T_1 = \frac{\sqrt{3}}{2} m' \cos(\omega \cdot t + \frac{11\pi}{6})$ $T_0 + T_7 = T - (T_1 + T_6)$

Depending on the type of switching, $T_0 = T_7$ or $T_0 \neq T_7$. Thus, after calculating V_{ref} which, in the case of a motor, its orthogonal components can be obtained from the motor current controller output, after locating in which sector V_{ref} is situated and calculating T_1 and T_2, it is necessary to calculate T_0 and T_7. According to [5], for symmetric switching, $T_0 = T_7 = (T - T_1 - T_2)/2$ (in sector 1), where V_0 is applied at the beginning and end of switching period and V_7 is applied in the middle of switching cycle [5]. Finally, it is necessary to assign the duty cycles to T_a, T_b and T_c as in the next table for the case symmetrical switching:

Table 2.7: Duty-cycles T_a, T_b and T_c for symmetrical switching (adapted from [5])

Sector	T_a, T_b, T_c
1	$T_a = T_0$ $T_b = T_0 + T_1$ $T_c = T_0 + T_1 + T_2$
2	$T_a = T_0 + T_2$ $T_b = T_0$ $T_c = T_0 + T_1 + T_2$
3	$T_a = T_0 + T_1 + T_2$ $T_b = T_0$ $T_c = T_0 + T_1$
4	$T_a = T_0 + T_1 + T_2$ $T_b = T_0 + T_2$ $T_c = T_0$
5	$T_a = T_0 + T_1$ $T_b = T_0 + T_1 + T_2$ $T_c = T_0$
6	$T_a = T_0$ $T_b = T_0 + T_1 + T_2$ $T_c = T_0 + T_2$

2.5.5 Controllers

This sub-section is intended as an overview of the type of controllers that methods associated with induction motor control (which will be studied later in this document) use. Based on the bibliographic study carried out, the types of controllers most commonly found were linear controllers and hysteresis controller. In this way, the basic operation and equations of these two types of controllers will be discussed here.

2.5.5.1 Linear Controllers

Linear controllers are those whose gains applied to the input error are constant over the entire range of values. However, linear controllers are effective if the system operating point is almost constant and the disturbances are not relevant [56]. In the case of field oriented control, which will be discuss further, the Park Transform is of great importance in transforming sinusoidal variables to approximately constant variables, allowing the application of this type of controllers. Nevertheless, for required range of operation, that is, changing operating points and strong disturbances [56], nonlinear control techniques are more suitable, such as fuzzy-logic, sliding mode or adaptive controllers.

There are 3 major types of linear controllers:

- Proportional controller
- Integral controller

- Derivative controller

In the proportional controller, the error between the desired set point and the actual value from the close loop is multiplied with a constant gain k_p:

$$y_p(t) = k_p e(t) \tag{2.49}$$

where y_p is the P-controller output and $e(t)$ the error. However, the steady-state error is not eliminated since the closer the system is to the desired reference, the smaller the error will be, as a consequence the controller action will be smaller and smaller for low error values. Thus, this controller provides a stable operation but maintains the steady-state error [57].

To eliminate the steady-state error, the integrative error control action can be added to the proportional controller - PI controller. The integral part integrates the error over time, ensuring a control action that eliminates the steady-state error, by holding the value to the final control at which error becomes zero. The gain of the integral controller is k_i, and the PI equation can be written as follows:

$$y_{pi}(t) = y_p(t) + y_i(t) = k_p e(t) + k_i \int e(t)\, dt \tag{2.50}$$

The disadvantages of this controller is the increased rise time and settling-time, not being the most suitable for systems that require a very fast dynamic response. On the other hand, this controller eliminates the steady-state error and reduces the maximum overshoot.

For systems that require a fast dynamic response, the use of a derivative action becomes necessary. This control action works by multiplying the error derivative of a gain k_d. Once the derivative of the error translates the future behaviour of it, since its magnitude translates the speed with which the system is tending towards the target value, and its sign indicates whether the target value has been reached or already exceeded, the derivative action is seen as a predictor of future behaviour of error. Then, an increasing of the derivative gain leads to an increase of the speed response. Furthermore, the derivative action adds damping to the system, which reduces the system overshoot. Thus, by combining actions of proportional, integral and derivative, a so-called PID controller is obtained. The PID equation is as follows:

$$y_{pid}(t) = y_p(t) + y_i(t) + y_d(d) = k_p e(t) + k_i \int e(t)\, dt + k_d \frac{d}{dt} e(t) \tag{2.51}$$

A study of comparing and analysis of the performance of these different controllers was carried out by [30]. The next table summarises the studied differences in the system response when the three gains, k_p, k_i and k_d, are changed:

Table 2.8: Response of different parameters with increase in K_p, K_i, K_d (adapted from [30])

Parameter (increase)	**Rise time**	**Overshoot**	**Settling time**	**Steady-state error**
k_p	Decrease	Increase	Small change	Decrease
k_i	Decrease	Increase	Increase	Decrease significantly
k_d	Minor decrease	Minor decrease	Minor decrease	No change

Each parameter and characteristics of the response is explained and graphically represented in the table 2.9 and figure 2.10, respectively:

Table 2.9: Step-response parameters

Characteristic	**Definition**
Rise time	Time required for the response curve to rise from: 10% to 90% (over-damped systems) 0% to 100% (under-damped systems)
Overshoot	Maximum value of the exceed of the response curve from the target value
Settling time	Time required for the response curve to stabilise at values with a maximum deviation from the target value never exceeding 3% or 5% typically.

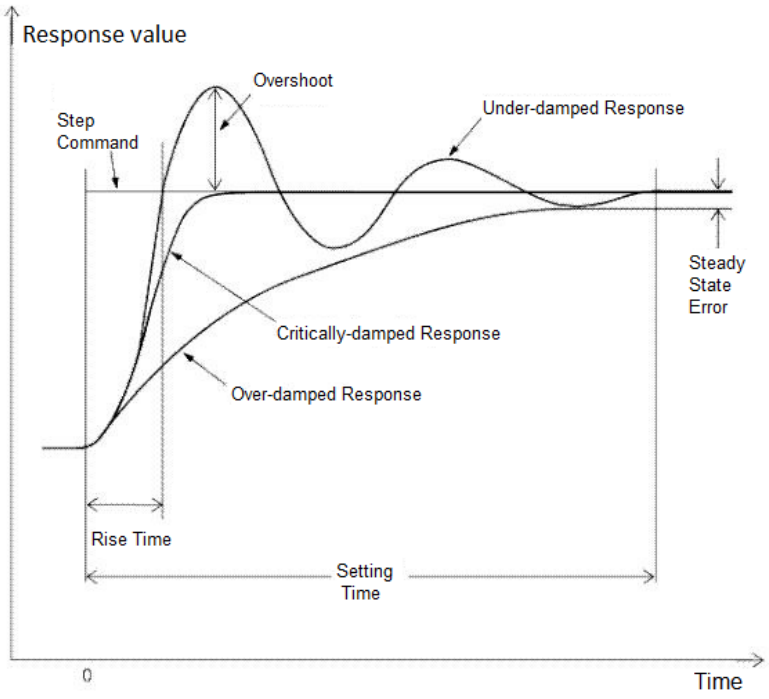

Figure 2.10: Step-response characteristics and parameters (adapted from [7])

2.5.5.2 Hysteresis Controller

The hysteresis controller aims to limit the error between predefined bounds. Whenever it exceeds one of these limits, lower and upper, an abrupt state changeover at the output occurs. Depending on the number of the possible output values, this type of controller can be classified as two-level hysteresis, three-level hysteresis and others. A 3-level hysteresis controller is represented in the next figure:

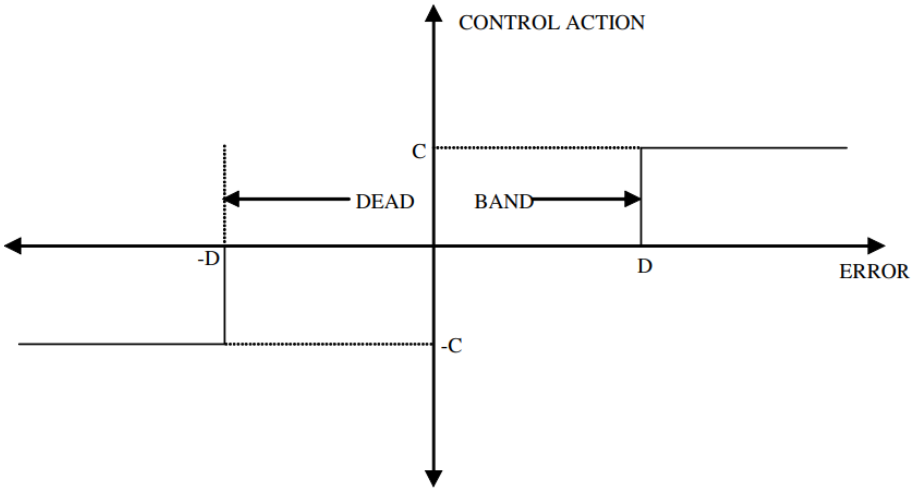

Figure 2.11: 3-level hysteresis controller [8]

Based on figure 2.11, the 3-level hysteresis algorithm is as follows, where $y_c(t)$ is the output signal of the controller, having C, $-C$ and 0 as possible values, D and $-D$ the defined bounds and $e(t)$ the error signal:

$$y_c(t) = \begin{cases} 0, & |e(t)| < D \\ -C, & e(t) < -D \\ C, & e(t) > D \end{cases} \tag{2.52}$$

Considering the same variable names, in the case of a 2-level controller, the algorithm can be written as follows:

$$y_c(t) = \begin{cases} 0, & e(t) < -D \\ C, & e(t) > D \end{cases} \tag{2.53}$$

2.5.6 Control methods for Induction Motors

2.5.6.1 Direct Torque Controller - DTC

Direct Torque Control is a method based on the direct application of a control sequence to switching states of the inverter [31]. The sequence selection is carried out using a switching table and two hysteresis controller responsible for regulating the electromagnetic torque and flux of the machine [44].

A schematic representation of DTC is shown in the next figure:

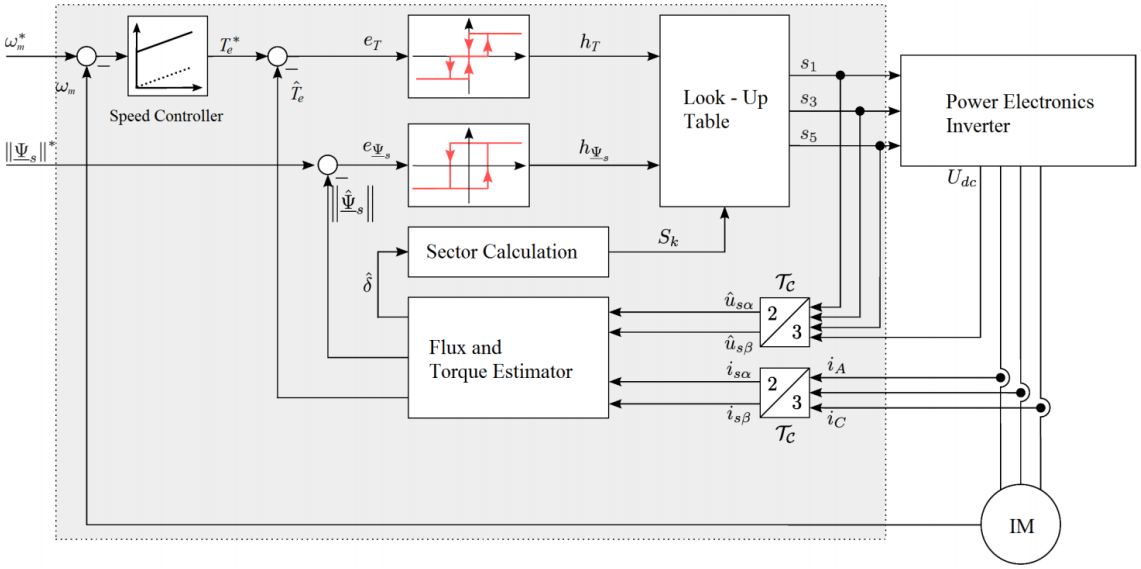

Figure 2.12: DTC schema [9]

From figure 2.12 the following blocks can be highlighted:

- Clarke Transformation
- Flux and Torque Estimator
- Sector Calculation
- 2 hysteresis controllers, also known as bang-bang controllers, for regulating Torque and Flux references
- Look-Up Table (or Switching Table)

It can also be observed that in this method only the measurement of the motor stator currents and voltages is required. Hence, the motor can be modelled by the $\alpha\beta$ model presented in 2.5.2.1, for which the currents and voltages are transformed using the Clarke Transform. Then, the flux and torque estimator is based on the equations 2.22, 2.23 and 2.21, respectively, and the flux angle can be calculated through the equation 2.27.

The "Sector Calculation" aims to determine in which sector the flux angle lies, as can be seen in the following figure:

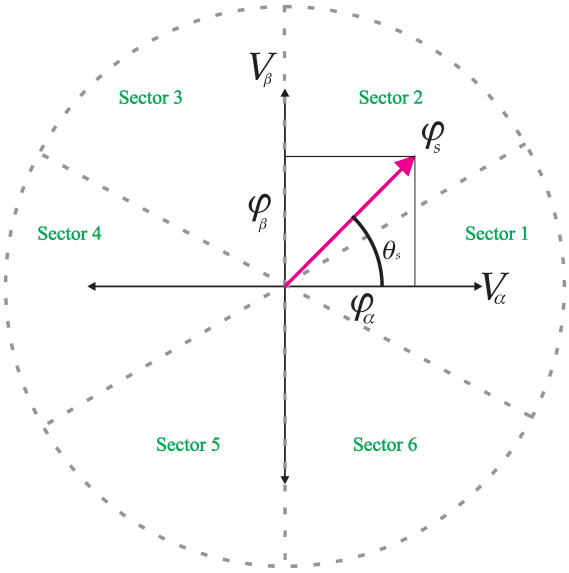

Figure 2.13: Sectors of the flux vector circular trajectory [10]

A method for this calculation is proposed by [10], based on the signs of the flux components, and can be determined using the equation 2.54 and table 2.10 [10]:

$$\psi_{ref} = \sqrt{3}\,|\psi_\beta| - |\psi_\alpha| \tag{2.54}$$

Table 2.10: Stator flux space vector's sector (adapted from [10])

Sector	Sign of ψ_α	Sign of ψ_β	ψ_{ref}
1	+	+/−	−
2	+	+	+
3	−	+	+
4	−	+/−	−
5	−	−	−
6	+	−	+

After estimating the electromagnetic torque and flux, as well as the sector to which the flux angle lies, it is necessary to compare the torque and flux values with the desired references. To accomplish this task, DTC uses two hysteresis comparators whose function is to restrict the magnitude of the torque and flux errors to values between two limits [11].The electromagnetic torque comparator is a three level hysteresis while the stator flux comparator is a two level hysteresis [31]. Thus, torque-controller output has -1, 1 or 0 as possible values, depending on if the error is either under lower limit, upper limit or between both [11]. On the other hand, flux-controller output can be 0 or 1, depending on if the error is under the lower limit or over upper limit, respectively [11].

Finally, the output of the two controllers are applied to the switching table 2.11 whose function is to calculate the switching states, taking into account the outputs of the two controllers and the sector to which the flux angle lies:

Table 2.11: Switching table (adapted from [31])

c_ψ	c_T	S_1	S_2	S_3	S_4	S_5	S_6
1	1	V_2	V_3	V_4	V_5	V_6	V_1
	0	V_7	V_0	V_7	V_0	V_7	V_0
	-1	V_6	V_1	V_2	V_3	V_4	V_5
0	1	V_3	V_4	V_5	V_6	V_1	V_2
	0	V_0	V_7	V_0	V_7	V_0	V_7
	-1	V_5	V_6	V_1	V_2	V_3	V_4

where the voltage vectors are:

Table 2.12: Voltage vectors

Vector	a	b	c
V_0	0	0	0
V_1	1	0	0
V_2	1	1	0
V_3	0	1	0
V_4	0	1	1
V_5	0	0	1
V_6	1	0	1
V_7	1	1	1

and c_ψ, c_T represents the torque and flux controller output, respectively.

The next figure represents the active voltage vectors and sectors of the flux space, where either flux reference either the flux controller hysteresis band are represented in the circle:

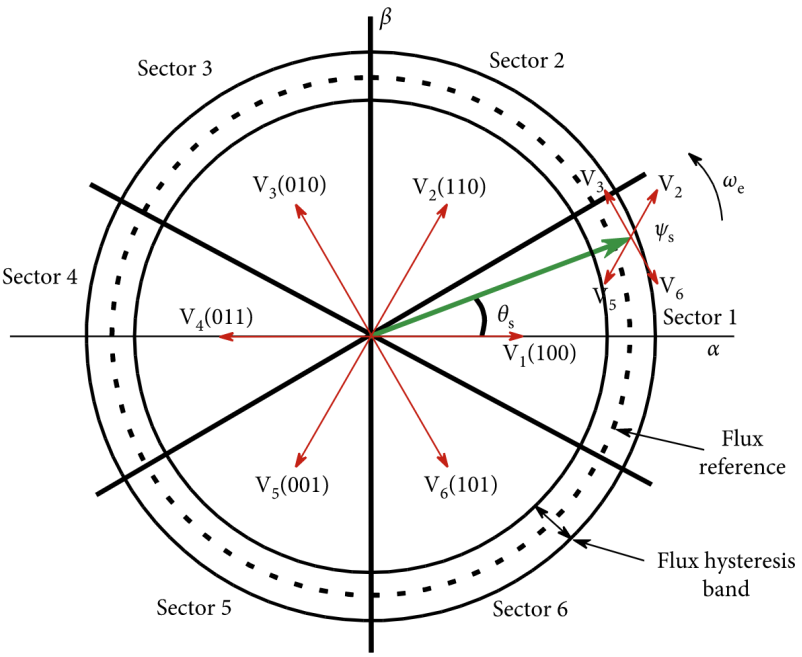

Figure 2.14: Active voltage vectors and sectors of the flux space [11]

A correct choice of the limits of the two hysteresis comparators must be ensured because, taking into account the switching behaviour of these controllers, the torque remains within a defined tolerance band, switching at a varied frequency between the two limits [9]. Moreover, their behaviour causes greater switching losses and high switching frequencies [11], which causes an irregular noise level, specially at low speed [9], and high ripple in the flux and electromagnetic torque that generates mechanical vibrations, deteriorating the machine performance [31].

2.5.6.2 Field Oriented Control - FOC

Field oriented control (FOC), also known as vector control, is a technique used to control AC machines which requires the transformation of the stator currents and voltages from the stationary reference frame to the rotor flux reference frame [58]. This transformation is already explained in 2.5.1.2 and 2.5.2.2. Typically, this technique is used for speed control or torque control, depending on the application [58]. The schematic of FOC is presented in the following figure:

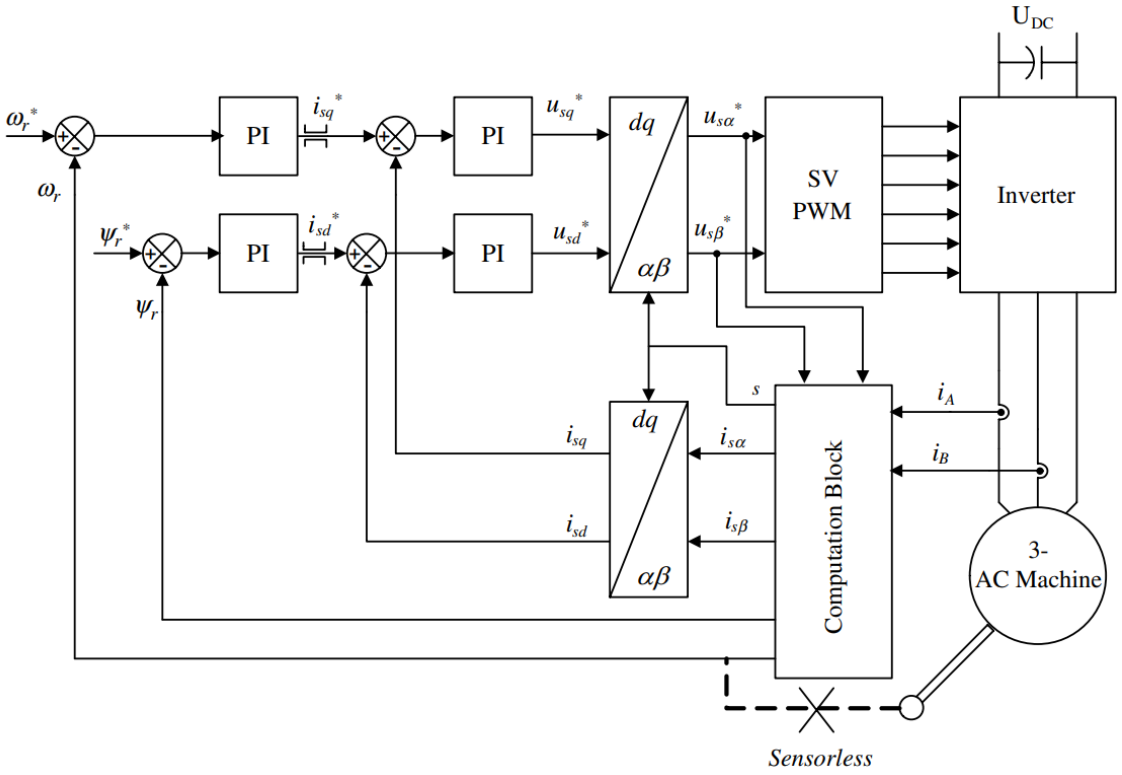

Figure 2.15: FOC for three-phase AC machine [12]

The working principle of FOC is based on the insight that the torque is proportional to the cross product of stator current and flux [9]. In this context, the stator current space vector can be decomposed into a flux-forming (i_d) and a torque-forming (i_q) component through the Park Transformation [9]. However, in order to allow the application of the Park Transform, obtaining the rotor flux angle represents one of the most important steps of the FOC. With respect to the method of obtaining this angle, FOC can be divided into two submethods: Direct Field Oriented

Control (DFOC) and Indirect Field Oriented Control (IFOC). According to [50], in the DFOC the rotor flux angle is obtained by using Hall sensors or flux sensing (proposed in the original approach of Blaschke [9]), or using flux observers which use the measured terminal voltages and currents [9]. On the other hand, the IFOC is knonw as feed-forward control, since obtaining the flux rotor angle requires the use of rotor position measurement and the calculation of the slip frequency from current reference values [9]. Although IFOC has several advantages over the DFOC, such as the elimination of the sensors, leading to the decrease of the cost factor, and better dynamic performance [59], the major drawback is the high sensitive to the rotor resistance, which affects the robustness of the control [9].

Manipulating the space vector equations of the motor presented in 2.5.2.2, the DFOC rotor flux angle can be calculated as follows:

$$\theta_e = \arctan(\frac{\psi_{rq}}{\psi_{rd}}) \tag{2.55}$$

In IFOC, the rotor flux angle is obtained by adding the slip frequency to the measured rotor angular speed:

$$\theta_e = \int \omega_e \, dt = \int \omega_r + \omega_{sl} \, dt \tag{2.56}$$

and the slip frequency can be estimated as:

$$\omega_{sl} = \frac{L_m}{\tau_r} \frac{i_{sq}^{ref}}{\lambda_{rd}} \tag{2.57}$$

where $\tau_r = \frac{L_r}{R_r}$ is the rotor constant time. If the rotor flux was kept constant and the d-axis is aligned to the rotor flux reference frame [60], the slip frequency can be simplified as follows:

$$\omega_{sl} = \frac{1}{\tau_r} \frac{i_{sq}^{ref}}{i_{sd}^{ref}} \tag{2.58}$$

because it is possible to imply [60]:

$$\lambda_{rd} = L_m i_{sd} \tag{2.59}$$

After obtaining the rotor flux angle, the measured stator currents are transformed into two DC components, d and q. Subsequently, these currents are compared with the two current references in order to calculate the current errors. These errors are then controlled by PI controllers, and the output of these controllers must correspond to the components of the reference vector, V_{ref}. Finally, the modelling method used by the FOC is the SV-PWM, already studied in 2.5.4.3. Depending on the reference frame using by SVM-PWM, V_{ref} components in dq frame may need to be transformed to $\alpha\beta$ referential through the inverse Park Transform.

According to [59], the main advantages of FOC are:

- Four quadrant operation

- Dynamic speed accuracy
- Torque control at low frequencies and low speed
- Improved torque response
- Reduction in power consumption

2.5.6.3 FOC vs DTC

A study comparing these two control methods was conducted by [9]. These methods differ considerably, although at the performance level one of the most critical difference are due to the controllers used. FOC uses linear controllers (PI) to control the flux and speed while torque is controlled indirectly [9]. To ensure a good response, a good tuning of them are required and their linear operation range has also a big impact on it. On the other hand, DTC uses two hysteresis controllers which control directly the torque and flux and select the appropriate stator voltage vectors, maintaining the torque and flux within upper and lower bounds [9]. Owing to their nature, the response time of hysteresis controllers is optimal. As drawback, the switching frequency is variable leading to more harmonic content in the output voltage of the VSI and, consequently, higher harmonic content in the motor torque, although within bounded values, resulting from the limits set in the controllers.

The following table sumarises the main differences between FOC and DTC:

Table 2.13: Comparison of FOC and DTC for Induction Motors (Adapted from [9])

	FOC	**DTC**
Reference frame	dq	$\alpha\beta$
Controlled variables	Torque (T_e) Rotor flux (ψ_r)	Torque (T_e) Stator flux (ψ_s)
Control parameters	Stator currents (i_s)	Stator voltage space vector
Sensed variables	Rotor mechanical speed (ω_m) Stator currents (i_s)	Stator voltages (V_S) Stator currents (i_s)
Estimated variables	Rotor flux position Slip frequency (ω_{sl})	Torque Stator flux (ψ_s)
Controllers	Linear controllers for stator currents	Hysteresis controllers for torque and stator flux
Torque Control	Controlled by stator currents High dynamics Torque ripple	Directly controlled High dynamics Controlled torque ripple
Flux Control	Controlled by stator currents Slow dynamics	Directly controlled Fast dynamics
Parameter sensitivity	Rotor time constant ($\tau_r = \frac{L_r}{R_r}$)	Stator resistance (R_S)
Implementation Complexity	High complexity Coordinate transformation necessary	Medium complexity No coordinate transformation necessary

2.5.6.4 Field Weakening Control

In certain applications such as traction drives, the motor is required to operate at higher speeds than its rated speed. This region of operation is called field weakening. The major problem in this region relates to the voltage and current constrains from the inverter [13], leading to the need for magnetic field reduction. However, to ensure maximum torque production, the motor's magnetic field must be adjusted correctly, maintaining maximum voltage and maximum current [12]. That is, weakening the magnetic flux to a level that ensures the maximum torque production over the whole speed range [12].

According to [12], there are three methods of controlling field weakening:

- adjustment of the machine flux in inverse proportion to speed $(1/\omega)$ [12]
- forward control of the flux based on simplified machine equations [12]
- closed loop control of the stator voltages to keep a maximum level [12]

A robust field-weakening method based on FOC and taking into account the voltage and current constrains is proposed by [13]. The voltage constrain equation is as follows:

$$v_{sd}^2 + v_{sq}^2 \leq v_{s,max}^2 \tag{2.60}$$

where $v_{s,max}$ corresponds to the maximum inverter output voltage, limited by the DC-link voltage and the modulation technique [13]. Since the modulation technique used in FOC is SVM-PWM, then the equation 2.60 can be rewritten as follows:

$$(R_s i_{sd} - \omega_e \sigma L_s i_{sq})^2 + (R_s i_{sq} - \omega_e \sigma L_s i_{sd})^2 \leq v_{s,max}^2 \tag{2.61}$$

where $sigma = 1 - \frac{L_m^2}{L_s L_r}$ is the leakage coefficient.

On the other hand, the current constrain equation is presented as follows:

$$i_{sd}^2 + i_{sq}^2 \leq i_{s,max}^2 \tag{2.62}$$

Assessing the two equations, the authors of [13] described the current constraint boundary as a circle with its center at the origin, while the voltage constraint boundary is an ellipse with its center at the origin. The resulting operating region is the overlap of voltage constraint ellipse and current constraint circle. For a maximum torque capacity, the authors considered that the operating point should be on the overlap edge [13].

The proposed method is then divided into three regions:

- Constant torque region
- Field-weakening region 1
- Field-weakening region 2

During the constant torque region, the motor operates at speeds lower than the base speed. In this region, the field current remains at its rated value [13] and the motor operation is only limited by the current constraint circle, then the torque current is limited as follows:

$$\left|i_{sq,limit}\right| = \sqrt{i_{s,max}^2 - i_{sd,rated}^2} \tag{2.63}$$

In the field-weakening region 1 ($\omega_m > \omega_{m,rated}$), the available operating region is now limited by current and voltage constrains as already explained. To ensure the maximum torque production and the field current reduction, the following method was proposed:

1. $i_{sd,ref}$ is regulated in inverse proportion to speed ($1/\omega$), named as basic strategy

2. If the inverter output voltage reference exceeds $v_{s,max}$, the voltage loop will be activated to reduce the unnecessary high flux level [13].

Thus, the flux current reference is the sum of the basic strategy current and the regulated current from voltage loop:

$$i_{sd,ref} = i_{BS} + i_{VL} \tag{2.64}$$

where i_{BS} is calculated as follows:

$$i_{BS} = \begin{cases} i_{sd,rated} & \omega_{m,ref} \leq \omega_{m,rated} \\ i_{sd,rated}\frac{\omega_{m,based}}{\omega_{m,ref}} & \omega_{m,ref} > \omega_{m,rated} \end{cases} \tag{2.65}$$

The voltage loop is controlled by a PI regulator and activated whenever the output voltage reference exceeds the maximum voltage allowed, that is, the output of the regulator is zero if $\Delta_{V_{DC}} \geq 0$ and negative when $\Delta_{V_{DC}} < 0$. $\Delta_{V_{DC}}$ is calculated as follows:

$$\Delta_{V_{DC}} = V_{s,max} - \sqrt{v_{sd,ref}^2 + v_{sq,ref}^2} \tag{2.66}$$

Thus, the voltage loop current has the following formula:

$$i_{VL} = k_{pv}\Delta_{V_{DC}} + k_{iv}\int \Delta_{V_{DC}}\, dt \tag{2.67}$$

where k_{pv} and k_{iv} are the PI coefficients.

Finally, the torque current limit will then be:

$$\left|i_{sq,limit1}\right| = \sqrt{i_{s,max}^2 - i_{sd}^2} \tag{2.68}$$

The field-weakening region 2 is applied at high-speed. In this region. the voltage constraint ellipse is even tighter, leading to the maximum torque operation point being on the edge of voltage

constraint ellipse, where the field current needs to be further reduced [13]. However, since at high-speed the stator resistance drop can be ignored [13], it is possible to simplify the voltage constraint equation:

$$i_{sq}^2 + (\frac{i_{sd}}{\sigma})^2 \leq \frac{v_{s,max}^2}{(\sigma L_s \omega_e)^2} \tag{2.69}$$

Nevertheless, the equation 2.69 is only valid when $i_{sq} < \frac{i_{sd}}{\sigma}$. Lastly, if $\psi_{rd} = L_m i_{sd}$, the torque current limit is now as follows:

$$|i_{sq,limit2}| = \frac{\psi_{rd}}{\sigma L_m} \tag{2.70}$$

The next figure presents a schematic of the method proposed by [13]:

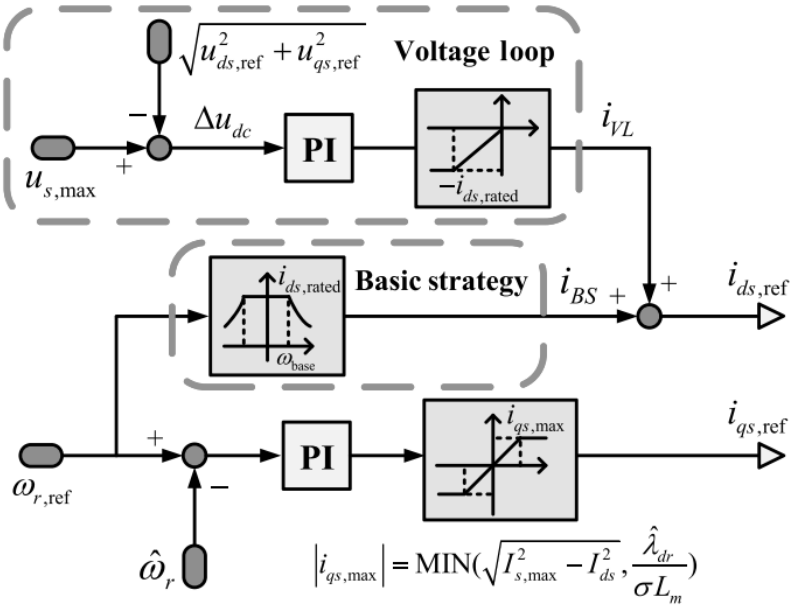

Figure 2.16: Field-weakening strategy (adapted from [13])

2.5.7 Battery

2.5.7.1 Mathematical Model

Since the AGV in this project is an electric vehicle, a good prediction of the battery status is essential to ensure the best estimation and control of its movements. That is, if the state of charge is low, it will be necessary to take the AGV back to the charging station, interrupting the transport of goods. Thus, the main equations that should be taken into consideration in order to simulate the status of the battery are the follows:

$$I_{battery} = \frac{V_{OC} - \sqrt{V_{OC}^2 - 4R_{int}P}}{2R_{int}} \tag{2.71}$$

where V_{OC} is the open circuit of the battery, R_{int} is the intern resistance of the battery and P is the sum the circuit power, including the motor power and load used for power consumption accounting without considering the motor. The voltage at the battery terminals and losses can be calculated as follows:

$$V_{terminals} = V_{OC} - R_{int} * I_{battery} \tag{2.72}$$

$$P_{Losses} = R_{int} * I^2_{battery} \tag{2.73}$$

Another important concept to take into account is SOC (State-of-Charge). The SOC characterizes the remaining capacity of the lithium-ion battery (LIB), and is defined as the ratio of the remaining capacity to the maximum available capacity [61]. The following equations represent the way SOC can be calculated:

$$SOC_t = 1 - DOD_t = \frac{C_t}{C_max} \times 100\% \tag{2.74}$$

$$SOC_t = SOC_0 - \frac{\int_{t_0}^{t} \eta i(t)\, dt}{C_{max}} \tag{2.75}$$

where SOC_t is the actual estimated SOC, DOD_t is the depth of discharge, C_t is the remaining battery capacity, C_{max} is the maximum available capacity when the battery is fully charged, SOC_0 is the initial SOC when the estimation process starts, η denotes the Coulombic efficiency, and $i(t)$ is the load current (assumed discharging is positive) [61].

2.5.7.2 Discharge characteristic

A battery is also described by its discharge curve. This curve shows the voltage evolution at the terminals as a function of the percentage of discharged load, i.e. current consumption. It is therefore desirable for these curves to be flat and for as long as possible, meaning that the battery voltage remains constant as it is discharged, and the longer the discharge lasts for the same consumed current, the better its capacity will be. The parameters which describe this curve are as follows:

Table 2.14: Discharge curve parameters (Adapted from [32])

Parameter	Formula	Description
A	$E_{full} - E_{exp}$	Voltage drop during the exponential zone
B	$\frac{3}{Q_{exp}}$	Charge of the exponential zone
K	$(E_{full} - E_{nom} + A \cdot e^{(-B \cdot Q_{nom})-1}) \cdot \cdot \frac{Q - Q_{nom}}{Q_{nom}}$	Polarization factor
E_0	$E_{full} + k + R \cdot i - A$	Ideal Voltage

2.5.7.3 Types of batteries

There are 4 major battery types on the market:

- Lead Acid
- NiCd
- NiMH
- Lithium-ion

The characteristics of these models can be studied in the figure below:

Specifications	Lead Acid	NiCd	NiMH	Li-ion		
				Cobalt	Manganese	Phosphate
Specific Energy Density (Wh/kg)	30-50	45-80	60-120	150-190	100-135	90-120
Internal Resistance (mΩ)	<100 12V pack	100-200 6V pack	200-300 6V pack	150-300 7.2V	25-75 per cell	25-50 per cell
Life Cycle (80% discharge)	200-300	1000	300-500	500-1,000	500-1,000	1,000-2,000
Fast-Charge Time	8-16h	1h typical	2-4h	2-4h	1h or less	1h or less
Overcharge Tolerance	High	Moderate	Low	Low. Cannot tolerate trickle charge		
Self-Discharge/month (room temp)	5%	20%	30%	<10%		
Cell Voltage (nominal)	2V	1.2V	1.2V	3.6V	3.8V	3.3V
Charge Cutoff Voltage (V/cell)	2.40 Float 2.25	Full charge detection by voltage signature		4.20		3.60
Discharge Cutoff Voltage (V/cell, 1C)	1.75	1.00		2.50-3.00		2.80
Peak Load Current Best Result	5C 0.2C	20C 1C	5C 0.5C	>3C <1C	>30C <10C	>30C <10C
Charge Temperature	-20 to 50°C -4 to 122°F	0 to 45°C 32 to 113°F		0 to 45°C 32 to 113°F		
Discharge Temperature	-20 to 50°C -4 to 122°F	-20 to 65°C -4 to 149°F		-20 to 60°C -4 to 140°F		
Maintenance Requirement	3-6 Months (topping charge)	30-60 days (discharge)	60-90 days (discharge)	Not required		
Safety Requirements	Thermally stable	Thermally stable, fuse protection common		Protection circuit mandatory		
In Use Since	Late 1800s	1950	1990	1991	1996	1999
Toxicity	Very High	Very High	Low	Low		

Figure 2.17: Characteristics of the battery models (adapted from [14])

2.5.8 Vehicle equations and dynamics

2.5.8.1 Kinematics equations

Considering an differential robot composed by two wheels, with their shaft passing by the same axle, their movement is controlled by varying each wheel speed independently [15].

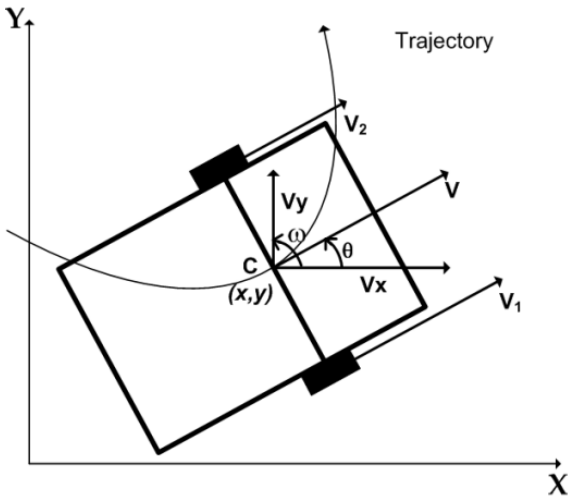

Figure 2.18: Differential Robot [15]

The robot's linear and angular speeds are as follows:

$$v(t) = \frac{V_1(t) + V_2(t)}{2} \tag{2.76}$$

$$\omega(t) = \frac{V_1(t) - V_2(t)}{b} \tag{2.77}$$

where $V_1(t)$, $V_2(t)$ are the right and left wheel speed respectively, measured in the contact point between the wheel and the ground and b the distance between the ground contact points [15].

Based on the centered difference discretization, the following equations are obtained:

$$x(i+1) = x(i) + d(i) \cdot \cos(\theta + \Delta\theta/2) \tag{2.78}$$

$$y(i+1) = y(i) + d(i) \cdot \sin(\theta + \Delta\theta/2) \tag{2.79}$$

$$\theta(i+1) = \theta(i) + \Delta\theta. \tag{2.80}$$

where:

$$d(i) = \frac{d_1(i) + d_2(i)}{2} \tag{2.81}$$

$$\Delta\theta(i) = \frac{d_1(i) - d_2(i)}{b} \tag{2.82}$$

2.5.8.2 Forces Acting on Road Vehicles

According to Newton's Second Law of Motion, the vehicle's longitudinal dynamics are described as:

$$m\frac{dv(t)}{dt} = F_p(t) - F_{res}(t) - F_b(t) \tag{2.83}$$

where m represents the vehicle total mass, F_p is the sum of forces applied by the powertrain at the wheels, F_b is the force applied at wheels during the braking and F_{res} represents the road load [2].

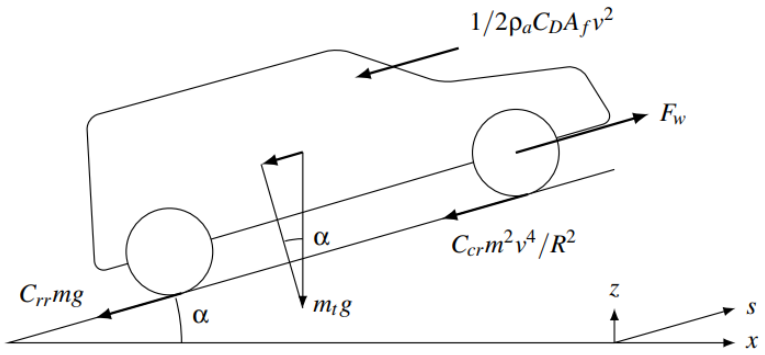

Figure 2.19: Schematic representation of the forces acting on a vehicle in motion [2]

Through the figure 2.19 is possible to describe the road load F_{res} as:

$$F_{res}(t) = \frac{1}{2}\rho_a C_D(t) A_f (v(t) - w)^2 + C_{rr} mg cos(\alpha(s(t))) + C_{cr}\frac{m^2 v(t)^4}{R(s(t))^2} + mgsin(\alpha(s(t))) \tag{2.84}$$

where C_{rr} is the coefficient of rolling resistance, α and R are the road slope and the out-of-the-pictured-plane radius of curvature, ρ_a is air density, w is longitudinal wind speed, A_f is vehicle's frontal area, C_{cr} the coefficient of cornering resistance and C_D is the aerodynamic drag coefficient [2]. This force can be seen as the sum of the Aerodynamics resistance (force acting opposite to the relative motion of any object moving with respect to a surrounding fluid); Tire Rolling Resistance (force per unit vehicle weight required to move the vehicle on level ground at a constant slow speed); Gradient Resistance (the resistance of the vehicle moving on a sloping road) and Inertia Resistance (opposite force generated during the acceleration and deceleration).

2.6 Navigation

This section aims to present concepts and methods of navigation available on the market and/or developed by other authors. Before the presentation of the different methods, it is necessary to present the different reference frames and clarify the difference between location and position. According to [28], position means an exact set of coordinates whereas the location can contain other information, such as junctions, other stations or when certain activities are necessary [28]. Thus, certain individual positions in the layout can be defined as locations and be serially numbered [28].

2.6.1 Reference frames

When a certain position of one point is studied, it must take into account that it is expressed in relation to some reference. This is the purpose of coordinate frames. Therefore, different coordinate frames and their mutual transformations will now be presented.

2.6.1.1 Earth-Centered Inertial Frame (ECI)

An inertial frame is defined as a non-rotating and non-accelerating frame with respect to the fixed stars [62]. It is used by all inertial sensors since they produce measurements relative to an inertial frame resolved along the instrument's sensitive axis [16]. Typically the inertial frame is the ECI and it can be defined as follows:

- **Origin**: at center of mass of Earth
- **Z-Axis** (z^i): parallel to the Earth's spin axis
- **X-Axis** (x^i): in the equatorial plane pointing towards the vernal equinox
- **Y-Axis** (y^i): completes a right-handed system

2.6.1.2 Earth-Centered Earth-Fixed Frame (ECEF)

This frame is similar to ECI frame, however it rotates along with the Earth [16]. It can be defined as follows:

- **Origin**: at the center of mass of Earth
- **Z-Axis** (z^e): parallel to the Earth's spin axis
- **X-Axis** (x^e): passes through the intersection of the equatorial plane and the reference meridian (i.e. the Greenwich meridian) [16]
- **Y-Axis** (y^e): completes a right-handed system

2.6.1.3 Local-level Frame (LLF)

A local-level frame is used to represent a vehicle's attitude and speed when on or near the surface of the Earth [16]. This frame can be referred to ENU (esat, north and up) or NED (north, east and down), depending on the direction which its axles are aligned. Whereas ENU's axis (x, y and z respectively) are aligned with the east, north and up directions, the NED's axis are alignned with north, east and down. Thus, this frame can be defined as:

- **Origin**: center of the navigation sensor frame or navigation system
- **X-Axis** (x^l) or **E-Axis**: points to east
- **Y-Axis** (y^l) or **N-Axis**: points to true north
- **Z-Axis** (z^l) or **U-Axis**: points upward along the ellipsoid normal

The next figure shows the spatial representation on Earth of the frames mentioned so far:

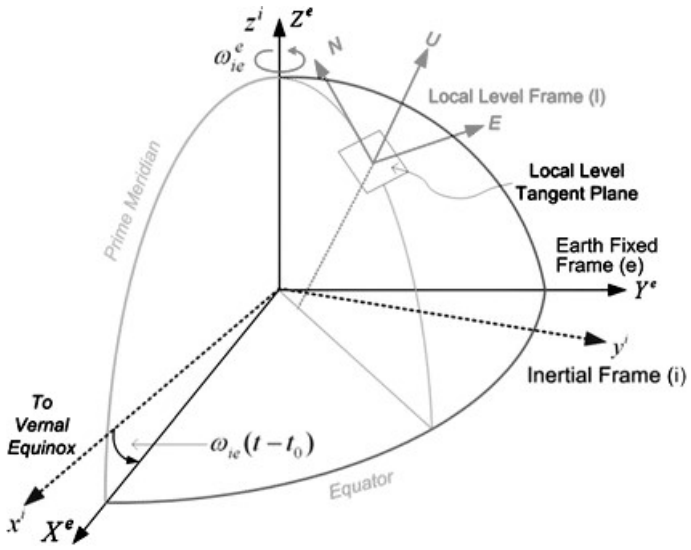

Figure 2.20: ECI, ECEF and ENU (local-level) frames representation (adapted from [16])

2.6.1.4 Body Frame

As the name indicates, the body frame is an orthogonal frame whose origin coincides with the vehicle's centre of gravity. Thus, the complexity in the calculation of its kinematic equations is reduced since the axes of motion of the vehicle are aligned with those of the sensor, for example an IMU. Then, it can be defined as:

- **Origin**: center of gravity of the vehicle (in order to simplify kinematics equations)
- **X-Axis** (x^b): points towards transverse direction direction (right direction of the moving vehicle)
- **Y-Axis** (y^b): points towards the forward direction

- **Z-Axis** (z^b): points towards the vertical direction (completes the right-handed system)

The following figure shows the comparison of the axis alignment of the body frame with the ENU frame:

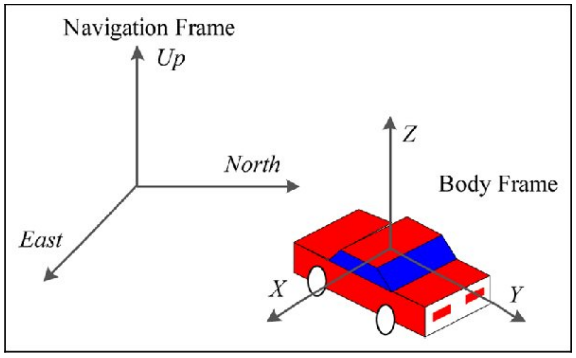

Figure 2.21: ENU (local-level) and body frames representation [17]

2.6.2 Important concepts

2.6.2.1 Reference Ellipsoid

Since the navigation of the AGV will take place in outer space, certain concepts associated with the Earth must be taken into account. The Reference Ellipsoid is on of them. According to [16], the Reference Ellipsoid is a mathematical model that approximates the geoid by an ellipsoid which center is coincident with the Earth's center of mass. This approximation is made by considering the rotation of an ellipse about its minor axis, which is coincident with the mean rotational axis of the Earth [16].

Different methods have been developed to parameterise this ellipsoid, being the world geodetic system (WGS)-84 one of the best known and currently used, whose parameterisation can be studied in the following table:

Table 2.15: (WGS)-84 parameters (adapted from [16])

Symbol	Value	Units	Description
a	6378137.0	m	Semimajor axis (equatorial radius)
$\frac{1}{f}$	298.257223563	—	Reciprocal flattening
$f = \frac{a-b}{a}$	0.00335281	—	Flatness
$b = a(1-f)$	6356752.3142	m	Semiminor axis
$e = \sqrt{\frac{a^2-b^2}{a^2}} = \sqrt{f(2-f)}$	0.08181919	—	Eccentricity
ω_e	$7.292115 \cdot 10^5$	rad/s	Earth's rotation rate
GM	$3.986004418 \cdot 10^{14}$	m^3/s^2	Gravitational constant

2.6.2.2 Normal and Meridian Radii

These two radii are of particular importance for further coordinate conversion, since these determinate the rates at which the latitude and longitude change as a vehicle moves on (or near) the

surface of the Earth [16]. Whereas R_N is defined for the east-west direction, R_M is defined for the north-south direction and their formulas are as follows:

$$R_N = \frac{a}{(1 - e^2 \sin^2 \varphi)^{\frac{1}{2}}} \tag{2.85}$$

$$R_M = \frac{a(1 - e^2)}{(1 - e^2 \sin^2 \varphi)^{\frac{3}{2}}} \tag{2.86}$$

where φ represents the latitude.

2.6.2.3 Earth Gravity

$$\gamma = a_1(1 + a_2 \sin^2 \varphi + a_3 \sin^4 \varphi) + (a_4 + a_5 \sin^2 \varphi)h + a_6 h^2 \tag{2.87}$$

Table 2.16: 1980 geographic reference system (GRS) (adapted from [16])

a_1	=	$9.7803267714\ m/s^2$
a_2	=	0.0052790414
a_3	=	0.0000232718
a_4	=	$-0.0000030876910891/s^2$
a_5	=	$0.0000000043977311/s^2$
a_6	=	$0.0000000000007211/ms^2$

2.6.3 Coordinate Transformations

2.6.3.1 ECI to ECEF

The difference between ECI and ECEF coordinate frames is due to the effect of the Earth's rotation rate, ω_e, that is, the ECEF frame rotates simultaneously with the Earth. Therefore, the transformation from ECI-frame to ECEF is the simple rotation of the the ECI-frame about Z-axis by an angle $\omega_e t$ [16]. The result matrix can be defined as follows:

$$R_i^e = \begin{bmatrix} \cos \omega_e t & \sin \omega_e t & 0 \\ -\sin \omega_e t & \cos \omega_e t & 0 \\ 0 & 0 & 1 \end{bmatrix} \tag{2.88}$$

where t is the time of the reference epoch [16].

The transformation of the coordinates expressed in ECEF to ECI-frame is performed through the inverse of R_i^e:

$$R_e^i = (R_i^e)^{-1} = (R_i^e)^T \tag{2.89}$$

2.6.3.2 LLF to ECEF

The rotation of LLF to ECEF involves the rotation of $\varphi - 90$ degrees around its east direction (X-Axis) and by $-90 - \lambda$ degrees about its up direction (Z-axis) [16]. Hence, the rotation matrix between these two coordinate frames can be written as follows:

$$R_l^e = \begin{bmatrix} -\sin\lambda & -\sin\varphi\cos\lambda & \cos\varphi\cos\lambda \\ \cos\lambda & -\sin\varphi\sin\lambda & \cos\varphi\sin\lambda \\ 0 & \cos\varphi & \sin\varphi \end{bmatrix} \tag{2.90}$$

where φ represents the latitude and λ the longitude.

The inverse transformation (ECEF to LLF) is calculated thus:

$$R_e^l = (R_l^e)^{-1} = (R_l^e)^T \tag{2.91}$$

2.6.3.3 Body Frame to LLF

This transformation can be expressed in terms of Euler angles: yaw, pitch and roll. These angles represent the attitude of a moving body, in this case a vehicle. Thus, transforming coordinates expressed in Body Frame to LLF is performed through the well-known direction cosine matrix, which can be written as follows:

$$R_b^l = \begin{bmatrix} R(1,1) & R(1,2) & R(1,3) \\ R(3,1) & R(2,2) & R(2,3) \\ R(3,1) & R(3,2) & R(3,3) \end{bmatrix} \tag{2.92}$$

$$R_b^l = \begin{bmatrix} \cos y\cos r - \sin y\sin p\sin r & -\sin y\cos p & \cos y\sin r + \sin y\sin p\cos r \\ \sin y\cos r - \cos y\sin p\sin r & \cos y\cos p & \sin y\sin r - \cos y\sin p\cos r \\ -\cos p\sin r & \sin p & \cos p\cos r \end{bmatrix} \tag{2.93}$$

where p, r and y represent the pitch angle, roll angle and yaw angle respectively. The value of these attitude angles can be obtain as follows:

$$p = \arctan \frac{R_b^l(3,2)}{\sqrt{[R_b^l(1,2)]^2 + [R_b^l(2,2)]^2}} \tag{2.94}$$

$$y = -\arctan \frac{R_b^l(1,2)}{R_b^l(2,2)} \tag{2.95}$$

$$r = -\arctan \frac{R_b^l(3,1)}{R_b^l(3,3)} \tag{2.96}$$

Once, the inverse transformation can be obtained:

$$R_l^b = (R_b^l)^{-1} = (R_b^l)^T \tag{2.97}$$

2.6.3.4 Body Frame to ECEF

This transformation is obtained indirectly through successive transformations (Body Frame to LLF and LLF to ECEF):

$$R_b^e = R_l^e R_b^l \tag{2.98}$$

and its inverse form can be also calculated:

$$R_e^b = (R_b^e)^{-1} = (R_b^e)^T \tag{2.99}$$

2.6.3.5 Body Frame to ECI

As in the previous transformation, this is also obtained indirectly (Body Frame to ECEF and ECEF to ECI-frame):

$$R_b^i = R_e^i R_b^e \tag{2.100}$$

with its inverse form being written as follows:

$$R_i^b = (R_b^i)^{-1} = (R_b^i)^T \tag{2.101}$$

2.6.4 Available methods for outdoor navigation

Outdoor navigation presents a new challenge. Firstly, the weather conditions are not constant, with changes in brightness throughout the day and the possibility of fog, rain or snow. This means that some of the methods available in the navigation market are not suitable for this type of environment, or those available are much more expensive or require much more complex and robust algorithms. On the other hand, other vehicles or pedestrians cross in this type of environment, which raises the level of safety required from an AGV.

After a bibliographical study, these are the navigation methods most commonly used in outdoor environments:

- Transponder navigation
- Laser navigation
- SLAM
- GPS navigation
- INS

2.6.4.1 Transponder navigation

According to Götting KG [18], through transponders, either specific positions are determined along a line or track-guided system, or virtual tracks are defined. The transponders are activated by the transponder reader/antenna, transmit their identification signal and their position is then detected with an accuracy of millimetres or centimetres. However, despite the fact that this type of navigation is easy to install if the driving surface is free of metallic surface, and very robust, it requires a hard floor, resilient to the heat as well as to the strain of multiple heavily loaded vehicles driving over it [28].

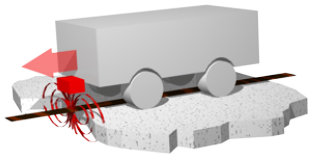

Figure 2.22: Transponder navigation (inductive) [18]

2.6.4.2 Laser navigation

Laser navigation is a free navigation method based on measure of reflecting light. Depending on the procedure used (with or without direct distance measurement) at least two or three markers must be visible to allow positioning [28]. The laser scanner scans the AGV surroundings without contact while driving and continuously measures the positions of the fixed reflectors. Comparing these to the coordinates of the reflectors as they were entered during start-up and configuration, the sensor recognizes the landmarks that lie along the route, determining its own current position and orientation along the route, which at the same time determines those of the AGV [28]. However, the traditional laser is not feasible for outdoor use because of its limited range and sensitivity to different weather conditions and the presence of other vehicles, especially trucks, can obstruct the sensor's field of view, interrupting the AGV's continuous positioning. Recently, the use of laser scanners has been applied in SLAM, a method that will be evaluated now.

2.6.4.3 SLAM

Simultaneous localization and mapping (SLAM) is a method used for vehicles such as AGVs that consists on building a map and localizing the vehicle in that map at the same time [63]. SLAM has been seen as the prime tool to solve detection and tracking of moving objects (DAMTO) problem concurrently, since DATMO allows the vehicle being aware of dynamic entities around, tracking them and predicting their future behaviors [64]. One of the most well-known mapping models is Occupancy Grid (OG), which is the process of memorizing data acquired by the robot during exploration in a suitable representation [64]. The main problems associated with the construction of OG lie in noisy sensors, sensor integration and high computational complexity [64].

For localization estimation, described as the process of deriving the current position of the robot within the map, there are three main approaches:

- Visual SLAM
- Lidar SLAM
- SLAM by sensor fusion

Visual SLAM uses images acquired from cameras and other image sensors [63] and can be divided into two main categories depending on the type of sensor used: Monocular Camera and Stereovision. Regarding Stereovision, the most popular approach in recent years is the feature-point based one, in which the camera motion is estimated with feature-point matching between consecutive frames, and 3D point clouds are generated based on the estimated camera motion [64].

Lidar SLAM can be divide into scan matching approach and probabilistic approach. Scan matching approaches also can be categorized based on their association method such as Feature-to-Feature, Point-to-Feature and Point-to-Point [64]. Feature-to-Feature approaches try to use less information to represent the raw data in order to speed up algorithms. On the contrary, Point-to-Point based approaches use all the raw data [64]. For Point-to-Point matching, ICP is one of the most successful algorithms that consists on iterative process by using a closed-point rule to initial guess of their relative pose, and then solving the Point-to-Point least-squares problem to compute their relative pose [64].

2.6.4.4 GPS navigation

In contrast to transponder navigation, the Global Navigation Satellite System (GNSS) works on any surface, but needs a clear line of sight upwards [28]. It calculates the distance from satellite to receiver by using interval between the signal from satellite and the signal to receiver and, through the triangulation method, the position of the receiver is calculated [22]. However, in order to provide accurate measurements, this method also requires the use of more expensive receivers as well as more than one.

The GPS has three main observables:

- Pseudo-range measurements
- Carrier phase measurements
- Doppler measurements

According to [65], the pseudo-range measures the distance between a satellite and a receiver. Its calculation takes the differences between the reception time and the transmission time multiplied with the speed of light. Thus, the pseudo-range for the mth satellite, in meters, can be written as follows [65]:

$$\rho^m = r^m + c\delta_{t_r} - c\delta_{t_s} + I^m + T^m + \varepsilon_p^m \tag{2.102}$$

where:

c	is the speed of light
r^m	is the true range between the receiver at time t_r and the the satellite at time t_t in meters
δ_{t_r}	is the receiver's clock offset in seconds
δ_{t_s}	is the satellite's clock offset in seconds
I^m	is the ionospheric delay in seconds
T^m	is the tropospheric delay in seconds
ε_p^m	is the error due to various sources

Another way to measure the distance between the sensor and the satellite is thought the carrier signals - carrier phase measurements, which can be written as:

$$\phi = \frac{1}{\lambda}(r + c\delta_{t_r} - c\delta_{t_s} - I_\phi + T_\phi) + N + \varepsilon_\phi \tag{2.103}$$

where:

λ	Wavelength
I_ϕ	is the ionospheric delay in meters
T_ϕ	is the tropospheric delay in meters
N	is the integer ambiguity in cycles
ε_ϕ	is the error in the measurement in cycles

To convert the phase measurement to meters, in [65] is suggested that the equation 2.103 can be multiplied by the wavelength:

$$\Phi = \lambda\phi = r + c\delta_{t_r} - c\delta_{t_s} - I_\phi + T_\phi) + N + \varepsilon_\phi \tag{2.104}$$

Regarding Doppler measurements, in [65] is stated that the Doppler effect is a frequency shift of the electromagnetic signal caused by the relative motion of the emitter and receiver. Thus, the Doppler shift can be calculated as follows:

$$f_d = -\frac{\dot{r}}{\lambda} \tag{2.105}$$

The position and speed calculations make use of these observations, which are described in detail in [62].

Coupled with all systems and sensors, there is the presence of errors that must be studied so that they can be mitigated. Regarding GPS, the sources of errors are the following:

- Satellite clock error
- Receiver clock error
- Ionosphere delay
- Tropospheric delay

- Multipath erros
- Satallite orbital erros
- Receiver noise

A detailed description of these can be found here [65]. In this same source, the user equivalent range error (UERE) is specified, described as the combined effect of all the residual errors:

$$\sigma_{UERE} = \sqrt{\sigma_{eph}^2 + \sigma_{clk}^2 + \sigma_{ion}^2 + \sigma_{tro}^2 + \sigma_{mlt}^2 + \sigma_{rcv}^2} \tag{2.106}$$

where

σ_{eph}	is the range due to ephemeris data
σ_{clk}	is the range due to the satellite's clock
σ_{ion}	is the range error due to ionosphere
σ_{tro}	is the range error due to the troposphere
σ_{mlt}	is the range error due to multipath
σ_{rcv}	is the range error due to the receiver measurement

2.6.4.5 INS

According to [62], Inertial Navigation System is considered a sophisticated Dead Reckoning. It is a combination of sensors able to determinate the position, speed and attitude of a moving object. Associated with this method of navigation is the concept of an IMU (Inertial Measurement Unit). A basic IMU consists of three accelerometers and three gyroscopes mounted on an orthogonal triad [62]. While accelerometers measure the specific force, gyroscopes are able to measure the angular rate with respect to the inertial referential. The specific force is defined as:

$$f = a - g \tag{2.107}$$

where

f	is the specif force, defined in the inertial frame
a	is the kinematic acceleration
g	is the gravitational acceleration

To obtain the speed, the gravity should be subtracted to the specific force and than integrated. Then, the result of the integration is added to the initial speed. Integrating the speed, the final position is yielded.

The purpose of using gyros is that specific force is expressed in a frame different from the frame in which speed and position are usually expressed (being the navigation frame the most used) [62]. Therefore, since when integrated, gyros provides the angular change with respect to the previous, supposed known, initial orientation [62], gyros are used to transform the specific force in the navigation frame.

However, the calibration of the gyroscope is crucial, as, according to [62], the presence of an uncompensated gyro error introduces the linear error in angles and in turn yielding quadratic error in speed and cubic error in position. For this reason, the latest IMUs introduce magnetometers. These sensors provides heading measurements relative to the Earth's magnetic north by observing the direction of the local magnetic field. Knowing the deviation between geographic north and magnetic north, known as declination angle, these sensors help to estimate the initial orientation of the object.

A full description of the errors associated with IMUs is described in [20], which can be:

- Bias
- Scale factor error
- Repeatability
- Resolution
- Stability
- Noise

The noise error is described as the random error that occurs in output and can be removed by stochastic models [20]. The most used model is the 1^{st} order Gauss Markov process.

2.6.5 Sensor fusion

According to [66], sensor fusion is a process that aims to combine data from different sensors in order to mitigate the uncertainties associated with them. The combination of sensors can be performed in three ways:

- Redundant sensors
- Complementary sensors
- Coordinated sensors

The redundant sensors give the same information for the world [66]. Complementary sensors, on the other hand, allow the sharing of distinct information to the world. Finally, the coordinated sensors collect information about the world sequentially [66].

The sensors communication can also be divided into three categories:

- Decentralized - There is no communication between the sensors nodes.
- Centralized - Involves a central node responsible for collecting measurements from all sensors.
- Distributed - The nodes interchange information at a given communication rate [66]

2.6.5.1 Kalman Filter

For sensor fusion, one of the most commonly used filters is the Kalman Filter (KF). Its applications requires that both the system and the measurement models of the underlying process are linear [19]. Since the information coming from the sensors is mostly transmitted at a constant rate, sampling frequency, i.e., in discrete-time form, it is also necessary to implement a discrete-time KF. According to [19], a discrete-time linear system can be described as:

$$x_k = \Phi_{k,k-1} x_{k-1} + G_{k-1} w_{k-1} \tag{2.108}$$

where:

x_k	is the state vector
$\Phi_{k,k-1}$	is the state transition matrix (STM)
G_{k-1}	is the noise distribution matrix
w_{k-1}	is the process noise vector
k	is the measurement epoch

The discrete-time linear measurement of the system is described as:

$$z_k = H_k x_k + \eta_k \tag{2.109}$$

where:

z_k	is the measurement vector
H_k	is the observation matrix
η_k	is the measurement noise

As $\Phi_{k,k-1}$ is the discrete-time representation of the known dynamic behaviour of the system, if F represents the dynamic coefficient matrix of a continuous time system, then the discrete-time STM can be obtained through the first two terms of the Taylor series expansion [19]:

$$\Phi = (I + F\Delta_t) \tag{2.110}$$

where I is the identity matrix and Δ_t the sampling interval [19].

In [19] the KF assumptions are also listed and the summary of which is as follows::

- Both the process and its measurements can be described by linear models
- The system noise w_k and the measurement noise η_k are uncorrelated zero-mean white noise processes with known auto covariance functions [19]
- The initial system state vector x_0 is a random vector uncorrelated to both the process and measurement noises and the mean value of its estimation, $\bar{x}_0$, and its covariance matrix P_0 are known.

The next table contains the description of the variables and terms associated to the implementation of this filter:

Table 2.17: KF variables and terms (adapted from [19])

Variable	Description
Φ	State transition matrix of a discrete-time linear dynamic system
H	Measurement sensitivity/observation matrix: defines the linear relationship between the state of the dynamic systems and the measurements
x	Sate vector of a linear dynamic system
$\hat{x}(-)$	The predicted value of the estimated state vector of a linear dynamic system
$\hat{x}(+)$	Corrected value of the estimated state vector of a linear dynamic system
$P(-)$	Predicted matrix of the covariance of state estimation
$P(+)$	Corrected matrix the estimation covariance of state estimation uncertainty in matrix form
z	Measurement/observation vector
K	Kalman gain matrix
w	Process noise
η	Measurement noise

A description of the step-by-step implementation is once again described in [19], whereby the next image summarises the algorithm associated with the implementation of this filter:

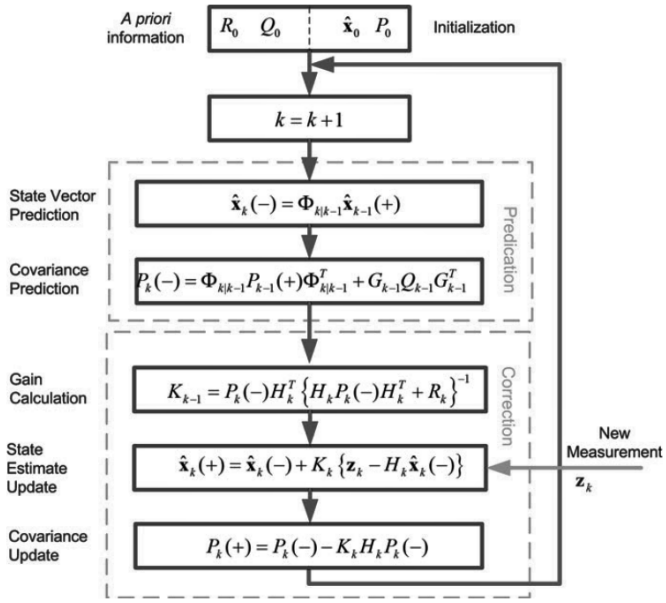

Figure 2.23: Kalman filter algorithm (adapted from [19])

2.6.5.2 GPS/INS integration

The integration of GPS with INS has been the subject of much recent study, presenting robust and adequate solutions for outdoor navigation, ensuring considerable advances in localisation and autonomous navigation. These two types of navigation have complementary characteristics which can be combined to improve the performance that either can achieve in a standalone mode [33].

The next table summarises the characteristics of these two methods:

Table 2.18: GPS and INS characteristics (adapted from [33])

Characteristics	**INS**	**GPS**
Accuracy	Short term accuracy (deteriorates with time)	Long term accuracy (noisy in short term)
Initial conditions	Required	Not required
Attitude information	Available	Not available (typically)
Sensitive to gravity	Yes	No
Self-contained	Yes	No
Jamming immunity	Yes	No
Output date rate	High	Low

According to [33], there are three main integration architectures:

- Loosely coupled
- Tightly coupled
- Ultra-tightly or deeply coupled

The loosely coupled strategy is a decentralized integration between GPS and INS. The basic steps of this method, based in [20], are as follows:

1. Determinate the position and speed (r^n_{GPS}, v^n_{GPS}) from GPS through the processing of the raw GPS measurements.
2. Determinate the position and speed from INS (r^n_{INS}, v^n_{INS}), output of the mechanization equations.
3. The difference between INS and GPS position and speed are used as input measurements to the KF [62].
4. The errors estimated are used to update the INS position and speed

Its method can be seen in the next figure:

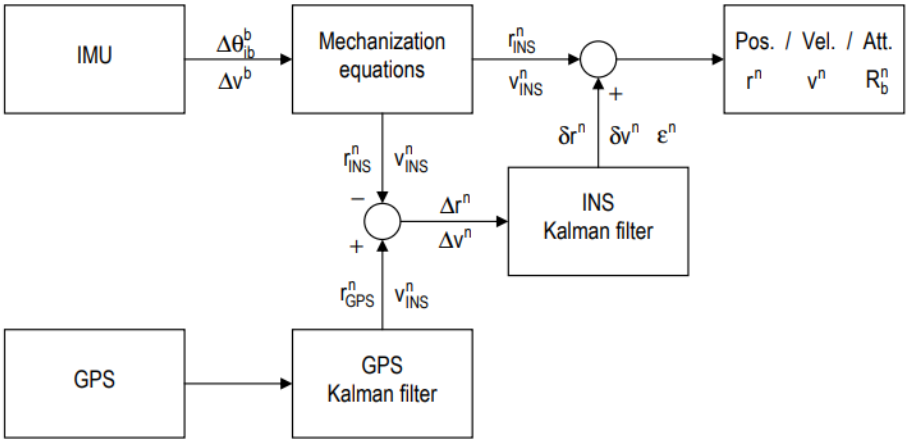

Figure 2.24: Loosely Coupled integration ([20])

As advantage, this method has a simple implementation, leading to better processing time of the algorithm. As disadvantage, this method requires the GPS position and speed, which is not always possible to obtain due to GPS cover (cannot be less than 4 satellites) [20].

The tightly coupled strategy is a centralized integration between GPS and INS. steps of this method, based in [20], are as follows:

1. Determinate the position and speed from INS (r^n_{INS}, v^n_{INS}), output of the mechanization equations.
2. Predict pseudoranges and Doopler measurement (ϕ_{INS}, $\dot{\phi}_{INS}$), using the raw GPS ephemeris information.
3. The difference between predict pseudoranges and Doopler measurement and the GPS pseudoranges and Doopler measurement are used as input measurements to the KF.
4. The errors estimated are used to update the INS position and speed

Its method can be seen in the next figure:

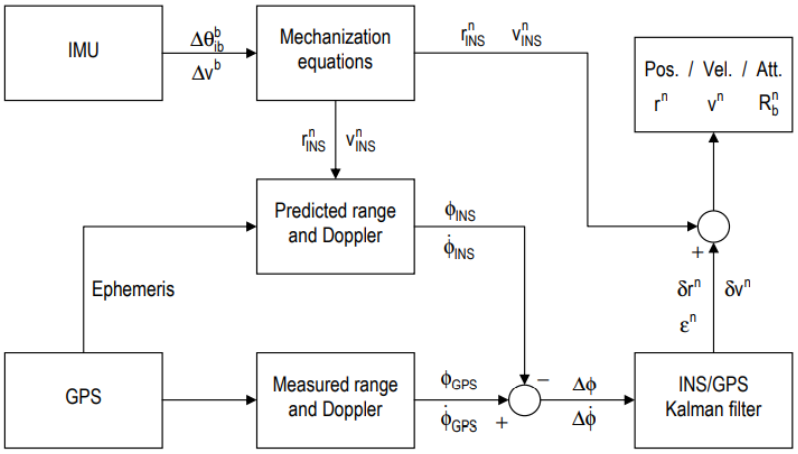

Figure 2.25: Tightly Coupled integration ([20])

As advantage, this method can update the INS result, even during poor satellite coverage [20]. As disadvantage, this method requires better computational resources since it is more complex and involves more variables.

In ultra-tightly strategy, the GPS measurements are used to estimate e INS errors and INS measurements to aid GPS receiver tracking loops [62]. This integration requires access to receiver's firmware, is not normally accessible in low-cost sensors.

2.6.5.3 Multi-GNSS RTK and Odometry

In 2019, M. Tradacete et al [21] proposed a method based on the fusion of Multi-GNSS RTK and Odometry by using an Extended Kalman Filter. The main advantage of using multi-GNSS lies in the increased number of tracked satellites to over 10 in good signal conditions and to more that 5 in almost any other situations [21]. RTK positioning is an interference positioning technique in which the distance (baseline vector) between a fixed base station and a rover station is obtained by calculating the distance between the two stations and the GNSS satellite, using measurements of the phase of the satellite signal's carrier wave. With the base station fixed at a known position, the position of the rover can then be determined using the baseline vector [67].

The system's architecture includes a Real-Time Kinematic Multi-Global Navigation Satellite System based on both GPS and GLONASS with a local base station that broadcasts differential corrections, a GPRS modem, and an incremental-encoder odometry system [21]. The system architecture diagram is shown in figure 2.26:

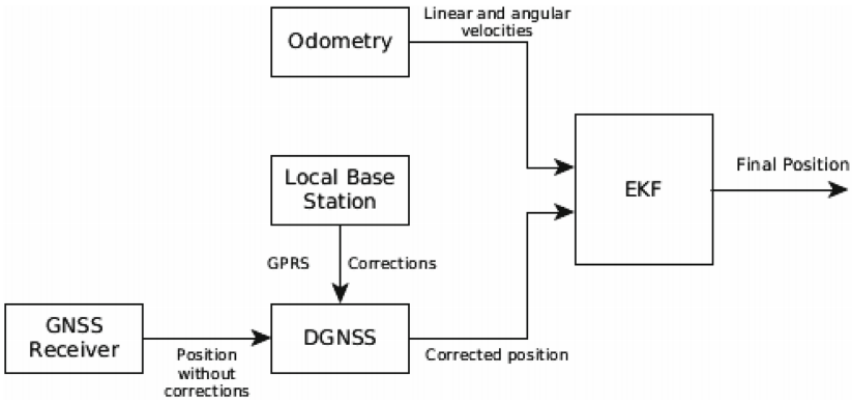

Figure 2.26: System architecture diagram [21]

For the Multi-GNSS it was included a differential Hiper Pro GPS+ receiver configured as rover, and a local base station to generate differential corrections. The rover is able to obtain data from both GLONASS and GPS to provide a more robust solution than a standard GPS by increasing the number of visible satellites. The use of differential corrections improve the achieved accuracy [21]. As result of GPS+GLONASS performance for differential receiver with Fixed-RTK, the

mean measurement error value was reduced to 1.3 cm with a max deviation of 3.4 cm. However, achieving a fixed-RTK solution takes a long time and it may even be unreachable due to poor satellite visibility. The mean required time to achieve convergence was over 9 min in about 50% of the tests carried out [21]. Regarding odometry, in order to remove the cumulative error, the relative position and angle are not given to the filter, but rather giving instant speeds.

The fusion algorithm is based on EKF, but with some changes. It was propose an adaptive filter in accordance with every available quality parameter in order to adapt the output of the filter to the real environment conditions, since the raw covariance matrices provided in the original method only considered certain quality indicators, which were insufficient for the application requirements [21]. The measurement covariance matrices provided by the sensors are adjusted following the GNSS receiver quality indicators: fix quality and Horizontal Dilution of Precision (HDOP) [21].

To test the localization system, an area approximately 4 *km* radius distance to the differential corrections base-station was chosen, enabling high quality corrections. The test route presented a length of about 5,5 km with both two lane and four lane roads involving challenging tasks for autonomous vehicles. Additionally, the route has been performed between 20 to 30 km/h, including defiant conditions for the GNSS signals [21]. The results presented demonstrate an accuracy of a few centimetres and the ability of the vehicle to keep within its lane. Considering that the AGV will navigate at lower speeds and the route will be shorter, this method presents itself as a very robust solution for the desired purpose of this dissertation.

2.6.5.4 Multi GPS and INS

This method was proposed in 2013 by S. Choi et al. [22]. According to the authors, the problem of using these methods alone is the error distance that can reach 10 *m* (in the case of GPS) and double integration makes the error increase with each iteration (INS).

High accuracy DGPS and RTK GPS has been researched, however these methods are very expensive comparing to normal GPS [22]. Thus, the integration method proposed was the tightly coupled GPS/INS. The block diagram of this method based on EKF is the following:

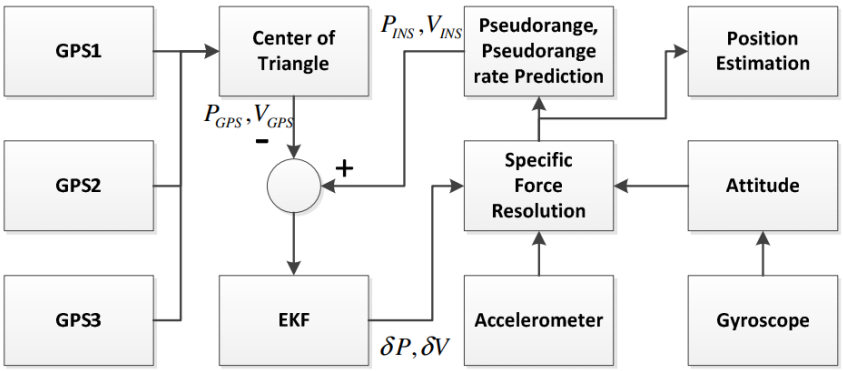

Figure 2.27: GPS/INS fusion algorithm [22]

Where GPS_n represents each GPS receiver and P_{INS}, V_{INS} and P_{GPS},V_{GPS} are the pseudo INS and GPS position and speed value respectively.

A particularity of this method was the use of three GPS receivers, arranged in the shape of a triangle, in order to improve accuracy.The the final positions is calculated through the equation [22]:

$$P(G_i) = (x_i, y_i), P(G) = \frac{G_1 \cdot n_1 + G_2 \cdot n_2 + G_3 \cdot n_3}{n_1 + n_2 + n_3} \tag{2.111}$$

G is the GPS receiver and n represents the number of measured satellites at the receiver. From a logical point of view, an algorithm has been developed for which the stability of the GPS signal reception is verified. That is, if the GPS receiver receives data from four or more satellites, the location information is considered stable and the system starts to collect and process data [22]. According to their studies, the maximum position error with Multi-GPS was 2.6117m, still large, but less than the error verified by a single receiver or three receivers without this algorithm.

Using 3 low-cost GPS receivers as a multiple GPS system and the tightly-coupled fusion system based on EKF showed up an average error of 0.5298m, proving that the multi-GPS system reduces the GPS error and the fusion system make the estimation more flexible and reduces the global error since the position error of INS is compensated by precise value of GPS absolute position information [22].

2.7 Safety Concept

Since outdoor environments usually require higher speeds, a greater sensing range for obstacle detection is necessary. Thus, avoiding collisions with static or moving obstacles is a key factor in ensuring safe navigation.

In 2012, T. Toben et al. [23] proposed a safety concept for efficient AGVs based on a combination of on-board sensors and fixed sensors installed in strategic locations.

The authors have defined three safety modes: **stop**, **normal** and **fast**. If the mode **stop** is activated, the vehicle cannot move and **normal** and **fast** refers to driving speed. As a safe vehicle is in particular collision-free, the vehicle is always safe or in mode stop [23]. The following constrains was defined to ensure the safe mode [23]:

1. Node stop is set and active at the beginning.
2. **Stop**, **normal** and **fast** cannot be activated simultaneously.
3. The modes **normal** and **fast** become active only if they are set.
4. Each mode takes time to activate:
   (a) If **normal** is active and **stop** is set, **stop** is active after t_n time units.
   (b) If **fast** is active and **normal** is set, **normal** is active after t_f time units.

(c) If **fast** is active and **stop** is set, **stop** is active after $t_f + t_n$ time units.

5. Setting a mode guarantees safety for a pre-defined time:

(a) If **normal** is set, driving with normal speed is safe for t_n time units.

(b) If **fast** is set, driving with fast speed is safe for $t_f + t_n$ time units.

In figure 2.28 the control flow between components of the safety architecture is represented.

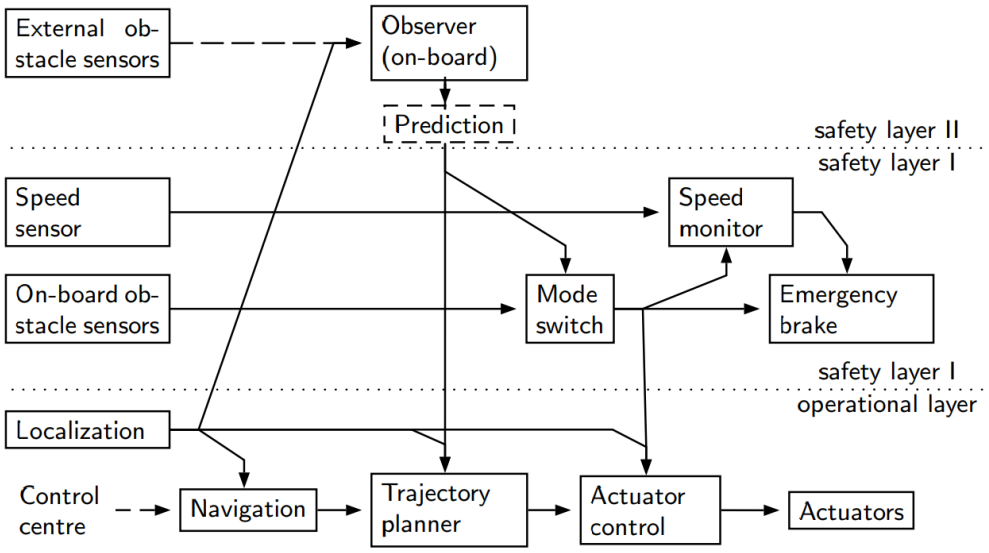

Figure 2.28: Safety system architecture [23]

While *safefty layer I* corresponds to the classical architecture of an AGV divring at a normal speed, *safefty layer II* is responsible to ensure safe driving at a faster speed [23]. **External obstacle sensors** are used to monitor the driving path in front of the vehicle and communicate the informatio to an on-board **Observer** component, which decides whether driving at fast speed is safely possible taking into account the current position of the vehicle [23]. The information from these two components is given to the **Mode switch** component, which sets the suitable mode for **Speed monitor**, **Emergency brake** and **Actuator control** in order to adjust the vehicle speed limit to the current mode [23].

A graphical schematic of the result of the combination of the two types of sensors is shown in figure 2.29:

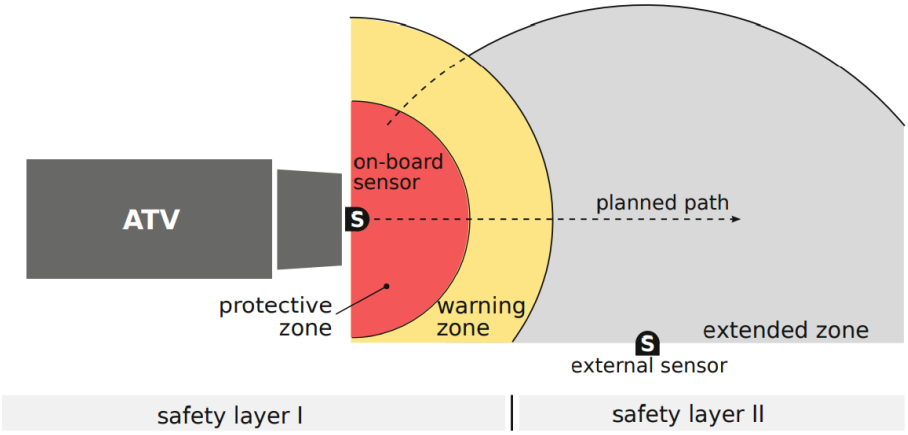

Figure 2.29: Zones covered by safety sensors (S) and their respective safety layer in the system architecture [23]

Thus, setting mode **fast** is only possible if no obstacle is in the extended zone. However, this implementation can be very conservative because not every obstacles in this zone necessarily poses a safety risk [23]. To this end, an **Prediction** component can be used to estimate the movements of the obstacle for the near future and then to decide whether a mode reduction is required [23]. The prediction of movement can be performed in three main ways:

- Nominal
- Probabilistic
- Worst-case

The nominal movement is an extrapolation of the past movement, while the worst-case movement model returns reachability sets and the probabilistic model adds probabilities to these positions [23]. On the one hand, for pedestrians a worst-case prediction is adequate because of their agility. On the other hand, for vehicles a probabilistic model is recommended that includes changes in speed and direction, but only to a certain realistic extent [23].

2.8 Energy Management

2.8.1 Regenerative Braking

Regenerative braking enables the vehicle's kinetic energy to be converted back to electrical energy during braking (deceleration or downhill running). The converted electrical energy is stored in energy storage devices to extend the driving range by up to 10% [68].

Kinetic energy of moving vehicles depends on mass and speed:

$$K_E = \frac{1}{2}mv^2 \tag{2.112}$$

Necessary kinetic energy to be dissipated to reduce vehicle speed from the initial to the final speed can be calculated by difference between car's kinetic energy at these two speeds [69]:

$$\Delta K_E = K_{E_{v_{final}}} - K_{E_{v_0}} \tag{2.113}$$

As power can be expressed as a function of the change in energy over a time interval, the power produced during braking can be calculated as follows:

$$P_{G_{out}} = \eta_G \frac{\Delta K_E}{\Delta t} \tag{2.114}$$

η_G indicates the efficiency of the motor/generator.

In this way, we can ascertain that the main elements associated with regenerative rafters are:

- Braking distance
- Initial speed
- Final speed

The braking distance depends on the force applied to the brakes, the speed difference, i.e. initial and final speed and also, among other factors, the road surface conditions. Longer braking distance might mean longer braking time and, coupled with a possibly greater force applied to the brakes, more energy is regenerated.

2.8.2 Optimization Algorithm

In order to optimise the driving cycles, the following conditions must be taken into account:

- Battery SOC
- Autonomy of the AGV (involves the battery capacity and control method)
- Minimum and Maximum time the AGV has to complete the transport of goods
- Minimum and maximum speed
- Energy produced from regenerative braking, which can happen during descent at a controlled speed or during necessary braking.
- Energy consumed

The desired result of the algorithm will be an appropriate speed for each sector of the route in order to minimise energy consumption.

2.8.2.1 Simulated Annealing

The SA algorithm is a heuristic algorithm for solving the global optimization problem by locating a good approximation to the global optimum of a given function in a large search space [70].

The steps of the SA algorithm are shown in the figure 2.30:

Data: Velocity series $V \in \mathbb{R}^{N \times L}$, Energy series $E \in \mathbb{R}^{N \times L}$
Result: Optimal policy $V^{\text{opt}} \in \mathbb{R}^{L}$
1 $[V^{\text{opt}}, E^{\text{opt}}] \leftarrow [V^{\text{curr}}, E^{\text{curr}}] \leftarrow \{[V_i, E_i] \mid \neg\exists\, j \;\text{ s.t. }\; \sum E_j < \sum E_i,\; i, j \in [1, \ldots, N]\}$;
2 **for** $\mathcal{T} = \mathcal{T}_{max}, \ldots, \mathcal{T}_{min}$ **do**
3 $[V^{\text{next}}, E^{\text{next}}] \leftarrow \text{Perturbate}(V^{\text{curr}}, E^{\text{curr}}, V, E)$;
4 $\Delta E = \sum E^{\text{next}} < \sum E^{\text{curr}}$;
5 **if** $\Delta E < 0 \vee \mathit{rand}(0,1) < e^{\frac{\Delta E}{\mathcal{T}}}$ **then**
6 $[V^{\text{curr}}, E^{\text{curr}}] \leftarrow [V^{\text{next}}, E^{\text{next}}]$;
7 **if** $\sum E^{curr} < \sum E^{opt}$ **then**
8 $[V^{\text{opt}}, E^{\text{opt}}] \leftarrow [V^{\text{curr}}, E^{\text{curr}}]$;
9 **end**
10 **end**
11 **end**
12 **return** V^{opt}

Figure 2.30: Energy consumption optimization algorithm base on SA [24]

According to [24], the algorithm starts by initializing speed and energy consumption with the current values and the optimal values. The current series identifies the latest perturbation iteratively, while the optimal series record the series with the minimal total energy consumed so far. During each iteration (line 2), the next series (line 3) can have a smaller or larger total energy. The difference is recorded in total energy consumption before and after the perturbation as ΔE in line 4. If the next series has a lower energy ($\Delta E < 0$) then it is accepted directly in line 5 and the perturbated next series is copied to the current solution (line 6), in order to start a new perturbation. During each next accepted solution it is checked whether the new current series has the minimum/optimal so far energy (lines 7-9).

2.9 Conclusion

Nowadays, AGVs are fundamental to optimise the intra-logistic processes as they are more and more flexible and allow the transportation of goods in a safe way, without the need of workers to perform these tasks. However, free navigation poses new hazards that must be avoided. In the context of Industry 4.0, the integration of various sensors has been essential to achieve the desired safety levels.

Regarding powertrain, the major problem of electric vehicles is related to their autonomy. Therefore, control methods should be chosen that ensure better use of available resources as well

as the achievement of better efficiencies. Furthermore, the lifetime of the machine should also be taken into account, as well as the load stabilisation of the AGV. Thus, modulation methods that produce large oscillations may not be the most suitable for this type of application.

Although sensing technology has evolved a lot, outdoor environments still represent a new challenge. Firstly because it is very common in these environments to share the same work area with people or other vehicles, then because weather conditions make it difficult to use methods such as vision or laser because on different days or seasons, conditions change, raising questions about the reliability of these methods. On the other hand, the current harmonised standard no longer addresses the current state of the art technology and is also not harmonized with the Machinery Directive.

Finally, navigation and safety become impossible to separate, since it is not possible to create specific zones for the use of AGVs for economic, flexibility or structural reasons. Navigation only makes sense if it is done safely. Therefore, it is fundamental to be able to detect and characterise obstacles attentively so as to enable safe braking or even circumvent possible obstacles and thus not disturb the work that the vehicle may be performing.

Chapter 3

Modelling and Analysis of the Powertrain

3.1 Introduction

The powertrain simulation was performed using Matlab and Simulink. This simulation has as main objective the study of the AGV dynamic behaviour. On the other hand, the energy consumption associated with different operating conditions was also analysed. In this way, this chapter will be subdivided by the different constituent elements of the powertrain in order to explain its implementation and/or the methods chosen.

3.2 Induction Motor

To simulate the electrical and mechanical behaviour of the induction motor a squirrel-cage induction motor model was adopted. For better organisation and easier access to information, a script was implemented in Matlab with its parameters and the Simulink "Asynchronous Machine SI Units" block was used for its simulation, and that can be seen in the following figure:

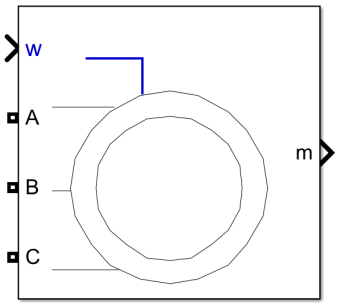

Figure 3.1: Asynchronous Machine SI Units (Simulink block)

The main parameters of the motor can be read from the following table:

Table 3.1: Induction motor parameters

Symbol	Value	Units	Description
P_n	5000	W	Nominal power
T_n	32.1855	Nm	Rated Torque
ω_n	152.3672	rad/s	Rated rotor speed
V_n	48	V	Rated line-to-line voltage
f_n	50	Hz	Rated frequency
p	2	—	Pole pairs
pf	0.72	—	Power factor
η_n	0.9	—	Rated efficiency
I_n	92.8096	A	Rated phase-current
R_s	0.0200	Ω	Stator resistance
R_r	0.0108	Ω	Rotor resistance
L_s	$84 \cdot 10^{-6}$	H	Stator inductance
L_r	$84 \cdot 10^{-6}$	H	Rotor inductance
L_m	$1.35 \cdot 10^{-3}$	H	Mutual inductance

From the dq model, already stated in 2.5.2.2, and the power factor, it is possible to obtain a good estimate of the rated values of the current i_d and i_q. This deduction is possible since the d-component represents the flux component and the q-component the torque component. In other words, relating current consumption to power consumption, the magnetisation of the machine involves the consumption of reactive power (associated with the i_d consumption) and torque production the consumption of active power (associated with the i_q consumption). Then, the current references can be calculated as follows:

$$i_{d-rated} = \sqrt{2} I_n \cdot \sqrt{1^2 - fp^2} \tag{3.1}$$

$$i_{q-rated} = \sqrt{2} I_n \cdot fp = \sqrt{(\sqrt{2} I_n)^2 - i_{d-rated}^2} \tag{3.2}$$

These two currents will be very useful for flux and torque control, as will be discussed later.

To simulate the mechanical behaviour, the simulink model offers two possibilities of coupling with the load (input): angular speed or load torque. When the input is in the form of torque, the angular speed of the rotor will be the result of the equation described in 2.5.2.3, so the parameters of the load such as inertia must be specified in this block. When the input is in the form of angular speed, the load inertia will have to be modelled externally. This input is viewed as a rotating load, which when force is applied to it will produce a rotary motion. Given the real context of a vehicle, where the rotary motion of the wheels is a result of the torque applied by the engine, the input model in the form of angular speed was adopted, so the parameters of the load were modelled externally in a block that will be detailed later.

3.3 Load Modelling

3.3.1 AGV route

The proposal for this dissertation is to develop a solution based on an electric AGV that tows a large load between two warehouses in an outdoor industrial environment. With full load, a maximum weight (AGV+load) of 5000 kg was assumed, while the empty AGV total weight was assumed to be 1000 kg. The maximum speed of the agv considered was 10 km/h. Between the two warehouses, there is a predefined route which AGV needs to follow in both directions, from warehouse A to warehouse B. Two routes are shown in the figure 3.2:

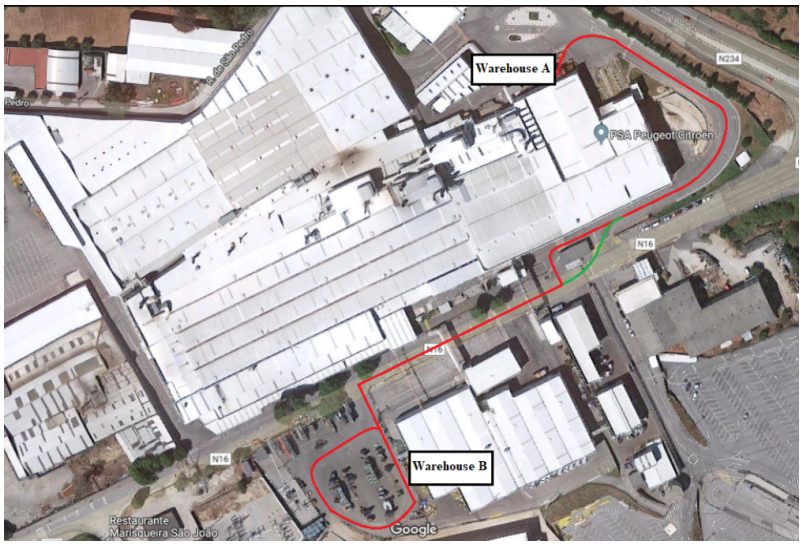

Figure 3.2: Outdoor environment with two routes (red and green)

Due to the length of the vehicle, the red route has two tight curves, which imposes difficulties in turning as well as lower speed. On the other hand, the green route is all the same as the red one except for the curve area, but it makes a more outward course with a lower curvature.

The AGV route can be further divided into three categories based on its slope:

- Flat route (0% gradient)
- Uphill course (about 2% gradient)
- Downhill course (about 2% gradient)

3.3.2 Forces Acting on Road Vehicles

To simulate vehicle dynamics, only straight-line motion was considered and with no wind speed. Thus, in equation 2.84, the effect of the turning resistance is neglected and $w = 0\ m/s$, leading to

the following simplification:

$$F_{res}(t) = \frac{1}{2}\rho_a C_D(t) A_f (v(t))^2 + C_{rr} mgcos(\alpha(s(t))) + mgsin(\alpha(s(t))) \tag{3.3}$$

The parameters required for this equation can be found in the following table:

Table 3.2: Resistance force parameters

Symbol	Value	Units
m	1000 or 5000	Kg
g	9.81	m/s^2
ρ_a	1.18 (at 25ºC and 1 atmosphere)	Kg/m^3
C_D	1.05	—
A_f	4	m^2
C_{rr}	0.013	—
$\alpha(s(t))$	$\arctan(-0.02)$, 0 or $\arctan(0.02)$	radians

3.3.3 Gearbox dimensioning

Considering the vehicle travelling at 10km/h with a full load, without braking action and on an uphill gradient of 2%, the total resistance force will be as follows:

$$\begin{aligned} F_{res} &= \frac{1}{2} \cdot 1.18 \cdot 1.05 \cdot (10 \cdot \frac{1000}{3600})^2 + 0.013 \cdot 5000 \cdot 9.81 \cdot \cos(\arctan 0.02) + \\ &\quad + 5000 \cdot 9.81 \cdot \sin(\arctan 0.02) \\ F_{res} &\approx 1.6374 \cdot 10^3 N \end{aligned} \tag{3.4}$$

With r representing the tires radius, the simple conversion from force to torque can be obtained as follows:

$$T = F \cdot r \tag{3.5}$$

Thus, assuming that $r = 0.1\ m$, the maximum torque required from the motor will have the value of:

$$T_{max} = F_{res} \cdot 0.1 \approx 163.74 Nm \tag{3.6}$$

This is approximately five times the nominal torque that the motor can produce. On the other hand, at a speed of 10km, converted into angular speed results in:

$$\omega_{wheels} = \frac{v}{r} \approx 27.78 rad/s \tag{3.7}$$

about 5.5 times less than the rated speed of the motor.

This requires the use of a gearbox. The principle of its operation is based on reducing the speed of rotation of its input, in this case the motor shaft, increasing the torque produced by it. In

this way, the speed applied to the wheels is adequate and the torque will be sufficient to overcome the resistance forces. Since the maximum speed allowed for the AGV is 10 km/h, the reduction coefficient of the gearbox will be calculated as a function of the angular speeds of the wheels and the engine:

$$G = \frac{\omega_n}{\omega_{wheels}} \approx 5.4852 \tag{3.8}$$

This reduction value will allow that, at the maximum linear speed, the rotation speed of the motor is its nominal speed. The torque applied to the wheels will be:

$$T_{wheels} = T_n \cdot G = 180.00Nm \tag{3.9}$$

As can be seen, at maximum linear speed, the motor will have a nominal speed, which leads to the production of its nominal torque, which, at the output of the reduction gearbox, is higher than the load torque. It can therefore be seen that the AGV will be able to accelerate, i.e. increase its speed if necessary, in what will be the worst case: maximum load, starting from rest and in an area of the route with an upward slope of 2%.

3.3.4 Speed and Acceleration calculation

The calculation of speed and acceleration of AGV is based on the basic equation of motion, taking into account the 2nd Law of Newton, as already presented in equation 2.83.

For simulation purposes, the mechanical braking force was not taken into account in order to study the amount of energy that could be regenerated during braking as well as the engine's ability to maintain a constant vehicle speed during downhill driving. Thus, equation 2.83 is reduced to the following form:

$$m\frac{dv(t)}{dt} = F_p(t) - F_{res}(t) \tag{3.10}$$

Given figure 3.3, F_p will correspond to the torque at the gearbox output multiplied by the radius of the wheels. The purpose of the "grade" input is to parameterise the value of the gradient of the route.

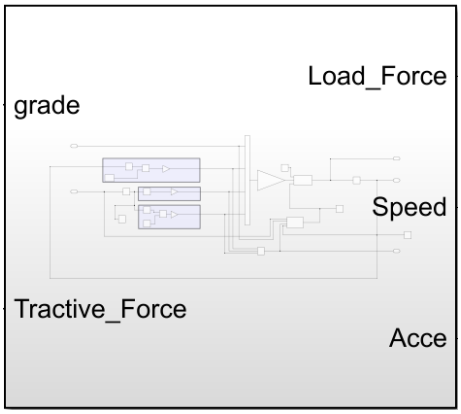

Figure 3.3: Load Model block (implemented in Simulink)

Although $m\frac{dv(t)}{dt}$ represents the inertia of the load, it is missing to add the effect of the losses concerning the gearbox and the force needed to rotate the rotating parts, whose equation is as follows:

$$F_r = I\frac{G^2}{\eta_g r^2}a \tag{3.11}$$

where I is the motor rotor inertia, and a value of 0.1 kgm^2 was taken, and $a = \frac{dv}{dt}$. For simplicity it was considered that $\eta_g = 1$.

Thus, the vehicle acceleration is calculated as follows:

$$a = \frac{F_p(t) - F_{res}(t)}{m + 0.1 \cdot (\frac{G^2}{r^2})} \tag{3.12}$$

To calculate the speed of the AGV, it is just required the integration the acceleration:

$$v = \int a\,dt \tag{3.13}$$

In turn, the speed value will be applied to the sub-block, in a closed loop, that calculates the value of the Aerodynamics Resistance. On the other hand, the angular speed is the input of the motor block, so the value of this will be calculated as follows:

$$\omega_m = v\frac{G}{r} \tag{3.14}$$

3.4 Motor Control Method

3.4.1 Introduction

To control the induction motor, the IFOC (Indirect Field Oriented Control) method was chosen. The schematic of a general FOC can be seen in the figure 2.15. The main reasons that motivated its choice, taking into account the FOC advantages (2.5.6.2) and the comparison between FOC and DTC (2.13), are as follows:

1. Less harmonic content in the motor output torque
2. Better use of DC bus voltage
3. Power consumption reduction
4. Very high dynamics are not required

The first reason is the durability of the materials. The AGV is a vehicle that carries heavy loads, so it will require maintenance due to the wear to which it will be subjected. The increase of vibrations on the AGV motor shaft, resulting in the torque ripple produced as a consequence of the voltage ripple applied to the motor, contributes to the reduction of its durability and performance. Both in DTC and FOC these vibrations are present, however in DTC they can occur at different frequencies while in FOC they occur at the switching frequency of the inverter switches, not affecting the fundamental component of the VSI output voltage. On the other hand, it is important that in the steady state the torque has a low ripple or at a constant frequency so that the load carried by the AGV remains stable and undamaged. Then, the second and third reason are interconnected. The FOC uses SVM-PWM as modulation technique which, as already studied, has modulation rates close to 90%, which leads to a good utilization of the DC bus voltage. In this way, batteries of such high voltages are not required compared to modulation methods such as SPWM, which results in a reduction in weight of the vehicle. Moreover, this technique allows to put at the VSI output the desired and adequate voltage for each voltage reference, which makes the FOC a robust method in torque control both at low and high frequencies and rotor speeds. Lastly, the total load on the AGV is 5000 kg, with a low-power motor. As a consequence, the difference between the electromagnetic torque and the load torque will be low, while the influence of inertia will be high on the dynamics of the system. Therefore, the dynamics of the system will be imposed by its inertia, and being high, it will be slow. For this reason, a stable steady state is required from the motor controller instead of a very fast response.

Taking into account the selected method, the following blocks necessary for its implementation will be addressed:

- Flux angle estimation
- Current transformation
- Outer controller
- Inner controller
- Modulation technique

3.4.2 Flux angle estimation

To estimate the flux angle, the method used was the one described in 2.5.6.2, concerning IFOC. The mechanical angular speed of the rotor is obtained through the motor simulation block, which,

among other variables, has this particular variable as one of its outputs. The mechanical slip speed of the rotor is obtained through the following block:

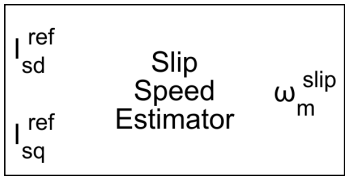

Figure 3.4: Slip Speed Estimator (Simulink block)

This block has as input the references of the currents (i_d and i_q) and in its output the mechanical slip speed of the rotor, whose equations inherent to this block are the equations 2.57, 2.58 and 2.59, studied in the study on FOC 2.5.6.2. Since its output is a mechanical speed, the result value of the equations 2.57 or 2.58 is then divided by the number of pole pairs of the motor (p).

Having obtained the two speeds (mechanical angular speed and mechanical slip speed of the rotor), these are then multiplied by the number of motor pole pairs in order to estimate the rotating field speed:

$$\omega_e = p(\omega_m + \omega_{m-sl}) \tag{3.15}$$

To obtain the flux angle, the speed obtained is integrated. However, as 2π *radians* represents one complete revolution of the motor shaft, and 0 *radians* being the start of the revolution, the integral value is reset each time it reaches 2π. As an expected result, the flux angle will have the shape of a straight line starting at 0 *radians* that whenever it reaches 2π *radians* it returns to the value of 0 *radians*, going up again until it reaches 2π *radians*, and so on. The higher the speed of the rotor, the faster this commutation occurs.

3.4.3 Currents transformation

For IFOC implementation, only the currents of phase *A* and *B* were measured, and phase *C* was estimated, assuming a balanced three-phase system, as already stated in 2.5.1.1. In order to transform them, these are the inputs of the block "Clarke Transform", whose outputs will be the inputs of the block that performs the Park Transform. Additionally, this last block, instead of admitting the flux angle as input, admits the cosine and sine of this angle. Thus, it is necessary to calculate the sine and cosine values of this angle, calculation that is performed in the Simulink block "Sine-cosine lookup" (figure 3.5). This block uses a table approach for optimized code-execution. The number of data points for lookup table chosen was 1024, the default value, and the unit of the angle is radians.

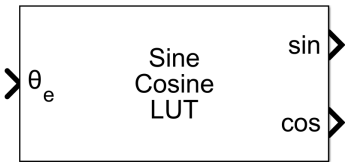

Figure 3.5: Sine-cossine loockup (Simulink block)

3.4.4 Outer controller

The outer control is seen as the combined action of the controllers that set the current references (d and q) for a given operating point. These two control actions are interconnected since $i_s = \sqrt{i_d^2 + i_q^2}$. While one controls the magnetization of the machine, the other is responsible for, knowing the reference magnetization current value, which torque current value it must set at its output. Both have as input the angular mechanical speed of the rotor (ω_m), in the first in its absolute value, in the second the error for a desired speed reference is calculated. On the other hand, in the outer control, the current consumed by the motor is limited and a control action is applied in the field weakening region.

3.4.4.1 Speed Control

Speed control involves the following elements:

- Generate a speed reference
- Compare the actual motor speed with the reference speed (speed error)
- PI controller
- Converting PI output to torque value
- Convert the torque value into i_q current

As studied in load modelling and gearbox dimensioning, the AGV speed and motor shaft speed only differ by the gearbox reduction ratio. Hence, the speed reference was expressed in km/h, for reasons of comobility in reading values in this unit, subsequently converted into m/s and finally multiplied by $\frac{G}{r}$ in order to convert it into angular speed. In order to ensure the same dynamic response of the system independent of the reference speed, in other words, to ensure that for the same floor conditions the AGV tends to the reference speed with the same acceleration, the error between the reference angular speed and the mechanical angular speed of the rotor has been normalised by dividing by the value of the reference angular speed:

$$\Delta\omega = \frac{\omega_{ref} - \omega_m}{\omega_{ref} + 0.001} \tag{3.16}$$

It should be noted that an offset with a value of 0.001 was added to the denominator of equation 3.16. This is because when the reference speed is zero, it is necessary to avoid dividing by zero.

Also, during motion, if the null reference is activated, it means that the AGV is commanded to stop, so it may be necessary to apply the mechanical brakes to shorten the braking time and distance.

After the error has been normalised, which means that it will typically assume values between 0 and $|1|$, it is necessary to generate an appropriate control action. The controller chosen was the PI controller. Although in 2.5.5.1 it was described that PID controllers are the most suitable for systems that require fast dynamic responses, in this case this requirement is not considered. As already explained in 3.4.1, in this system the dynamic response will be imposed by its inertia, which is high due to the AGV load and the presence of a low power motor.

Instead of using appropriate tools for tuning the controller gains, these were tuned based on the information from the table 2.8 and the evaluation of the system response for the different gains. Then, the gains that are considered appropriate for this controller are those present in the following table:

Table 3.3: Speed controller: PI gains

Gain	**Value**
k_p	1.5
k_i	0.1

K_p has a value of 1.5 for the following reasons:

- As the error varies between 0 and $|1|$, and 1 represents a maximum deviation, so the maximum torque is desired in order to promote maximum acceleration allowed. Thus, if the error was constant and always maximum, the controller output would have the value of 1.5, assuming only the proportional action.

- In transient regimes, the motor is allowed to reach overload regimes (torque produced higher than the nominal torque). The maximum allowed overload value was 50%, thus at 50% of overload, the torque produced will be about $1.5 \cdot T_n$.

Subsequently, a gain with the value of the motor nominal torque (T_n) will be applied to the controller output. This gain is responsible for converting the controller output into torque values. In turn, the conversion of torque into a reference value iq is based on the following equation:

$$T_e = \frac{3}{2}\frac{L_m}{L_r} p(i_{sq}\psi_{rd} - i_{sd}\psi_{rq}) \tag{3.17}$$

Approximating ψ_{rd} by $L_m i_{sd}$ and considering that the q-component of the steady state rotor flux can be neglected, the following simplification can be obtained:

$$T_e = \frac{3}{2} p \frac{L_m^2}{L_r}(i_{sq} i_{sd}) \tag{3.18}$$

Thus, being i_{sd-ref} the i_{sd} reference current and T_{PI} the controller output multiplied by the gain T_n, i_{sq-ref} is obtained as follows:

$$i_{sq-ref} = \frac{T_{PI}}{\frac{3}{2}p\frac{L_m^2}{L_r}i_{sd-ref}} \tag{3.19}$$

3.4.4.2 Flux Control

The principle of flux control is to ensure the correct magnetisation of the motor by generating a current reference i_{sd-ref}. Excluding the control mechanism in field weakening, this current will have its nominal value, which can be calculated through the equation 3.1. Thus, for rotor mechanical speeds between 0 to ω_n the value of the current reference i_{sd} will have the value as the rated i_d current:

$$i_{sd-ref} = i_{d-rated} \approx 91.0859A \tag{3.20}$$

3.4.4.3 Field Weakening Control

For the field weakening control, only two of the three regions shown by [13] were considered:

- Constant torque region
- Field weakening region

The voltage loop has also been neglected. The reasons for this choice are as follows:

- Since the reduction gearbox was dimensioned so that the maximum speed of the AGV was equivalent to the nominal rotation speed of the engine, only in specific cases, such as descents, did the speeds of the latter exceed its rated value. Therefore, the AGV will not be allowed to reach speeds that would justify entering the field weakening region 2.
- As the motor will be allowed to reach overload and the input of the modulation block will be limited, as will be discussed below, the voltage loop is not relevant under these simulation conditions.

Therefore, the value of the current reference i_d will correspond only to the value of i_{BS} (equation 2.65) presented in 2.5.6.4, i.e. it will have the following form:

$$i_{sd-ref} = \begin{cases} i_{sd-rated} & \omega_{ref} \leq \omega_n \\ i_{sd-rated}\frac{\omega_n}{\omega_{ref}} & \omega_{ref} > \omega_n \end{cases} \tag{3.21}$$

Taking into account the current constrain, two limits have been set for the current i_q:

$$i_{sq-limit} = \begin{cases} \sqrt{is_{max}^2 - i_{sd-ref}^2} & i_{sq-ref} \geq 0 \\ -i_{sq-rated} & i_{sq-ref} < 0 \end{cases} \tag{3.22}$$

When the reference of iq takes negative values, the limit for this will always be, in absolute value, equal to the nominal value of iq. A negative reference of iq represents the induction motor entering in regeneration mode. For battery protection, namely overheating problems, the maximum current that the motor can regenerate shall take its nominal value.

3.4.4.4 Overload limiter

In order to improve performance, it may be necessary, during transients, for the electromagnetic torque produced by the motor to exceed its nominal value by overloading. However, overloading will result in a reduction in the life of the machine as well as problems of overheating. Therefore, it is necessary to study the construction characteristics and type of insulation of the motor in order to be able to draw a relationship between the overload percentage and the time that the machine may be operating in this mode.

Considering that in the worst case, i.e. the AGV starts moving at a standstill, at full load and while climbing, the electromagnetic torque exceeds the load torque, thus allowing the AGV to increase its speed, the overload entry is only necessary for a few seconds in order to reduce the time until it reaches a given speed reference. For this reason, and given that the main focus of the powertrain simulation will be to evaluate the dynamics of the AGV+load system and to study the energy consumption, a maximum overload of 50% was admitted. As such, the maximum current presented above is multiplied by 1.5:

$$i_{s-max} = 1.5 \cdot \sqrt{2} \cdot i_n \tag{3.23}$$

3.4.5 Inner control

The inner control ensures the correct operation of the electrical machine for a given operating point, i.e. application of the desired current references to the motor. As the function is the application of the references generated to the motor, it is essential that the dynamic response of the controllers is faster than that of the outer controllers. In other words, if it is desired that the AGV moves at a certain speed and the outer control generates the current references in order to produce the desired torque, it is intended that the internal controller quickly applies these same references to the motor so that it produces the required torque. Based on table 2.8, a low rise-time is required in this case. If the overshoot is controlled, the currents fluctuate around the reference value but with small deviations, ensuring a fast application of the desired current reference.

From the FOC point of view, this control is responsible for creating the reference voltage vector, whose components will be the input of the modulation block. Thus, this control is based on two PI controllers, one for the control of the current error i_d and the other for the current error i_q. The outputs of these controllers correspond to the orthogonal components of the reference voltage vector.

3.4.5.1 Flux current controller

The flux current controller is the controller of the current i_d. The current reference i_d was subtracted from the current id applied to the motor, forming the current i_d error. This error is then normalised and divided by the rated value of the current i_d:

$$\Delta_i d = \frac{i_{sd-ref} - i_{sd}}{i_{sd-rated}} \tag{3.24}$$

The gains of the PI controller are as follows:

Table 3.4: Flux controller-PI gains

Gain	Value
k_p	0.9
k_i	9

The output of this controller is limited to -1 and 1. This is due to the fact that the current has been normalised and the input of the simulation block only admits values between these two.

3.4.5.2 Torque current controller

The torque current controller is the controller of the current i_q. Similarly to the i_d current loop, the error of this current is also normalised to its rated value:

$$\Delta_i q = \frac{i_{sq-ref} - i_{sq}}{i_{sq-rated}} \tag{3.25}$$

The PI controller output is also limited between -1 and 1, for the same reasons as above. Its gains are as follows:

Table 3.5: Torque controller-PI gains

Gain	Value
k_p	3
k_i	10

3.4.6 Modulation Technique

3.5 Voltage Source Inverter

The VSI was built using an IGBTs bridge through the "IGBT/Diode" Simulink block, which implements an ideal diode and an antiparallel diode. The representation of the VSI implementation can be seen in the next figure, where the letters in block C, E and g represent the collector, emitter and gate of the IGBT respectively. The gate is where the command signal to open and close the IGBT is received (gate control).

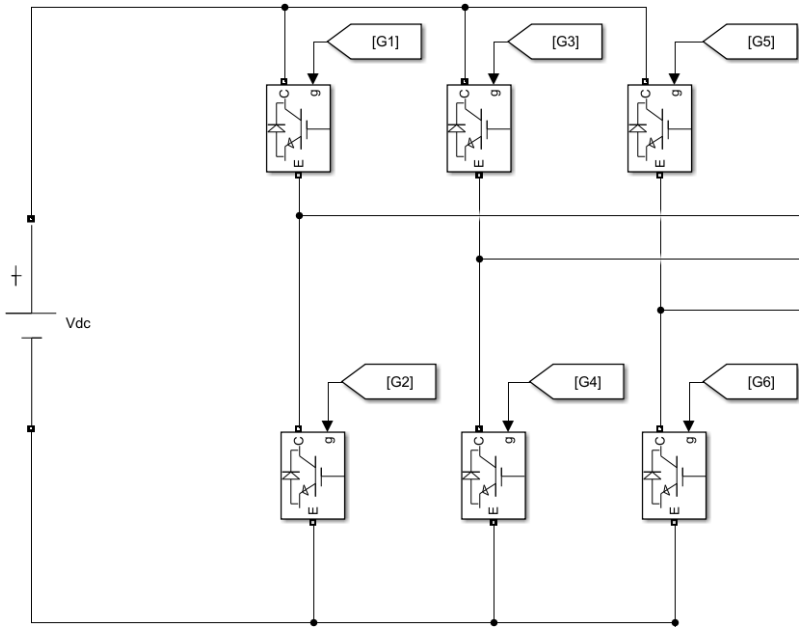

Figure 3.6: Voltage Source Inverter using IGBTs (implemented in Simulink)

The internal parameters associated with the IGBTs are described in the following table, whose values have been kept the default ones by the block.

Table 3.6: IGBT/Diode block internal parameters

Symbol	Value	Unit	Description
R_{on}	$1 \cdot 10^{-3}$	Ohm	Internal resistance
R_s	$1 \cdot 10^{5}$	Ohm	Snubber resistance
C_s	inf	Ohm	Snubber capacitance

3.5.1 Modulation technique

As already studied, the modulation technique of the FOC is SV-PWM. In Simulink, the block that implements this technique is the "SVPWM Generator (2 level)", figure x. As inputs, this admits the orthogonal components α and β, or through the representation in phase and modulus, of the voltage reference vector, v_{ref}, and presents in the output 6 command signals, one for each switch, being that the command signal of switch 2, S_2, complementary of the signal S_1, and so on. While the orthogonal components are limited between -1 an 1, the modulus varies between 0 and 1.

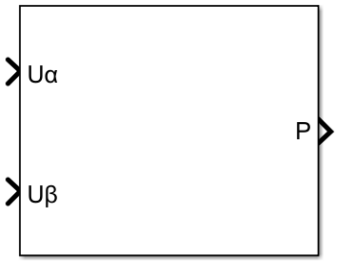

Figure 3.7: SVPWM Generator (2 level) (Simulink block)

Using this block, the output voltage of the VSI is calculates as follows:

$$V_{out} = m\frac{V_{DC}}{\sqrt{2}} \tag{3.26}$$

where m represents the modulation index. As verified in the literature review, SV-PWM allows modulation indices of about 90%. Knowing the value of the motor supply voltage and considering $m = 0.9$, it is possible to calculate the battery voltage required to power the DC bus:

$$V_{DC} = \sqrt{2}\frac{V_{out}}{0.9} \approx 75.42V \tag{3.27}$$

On the other hand, it is necessary to set the switching frequency, which will correspond to the PWM frequency. In order to obtain results with reduced harmonic content at low frequencies, but guaranteeing more computational flexibility, it was defined a switching frequency with the value of 10000 Hz.

3.5.2 Inverse Park Transform

As the outputs of the PI controllers are the components of the voltage reference vector, expressed in the dq referential, it is necessary to convert them to the dq referential. This transform is calculated through the inverse Park transform, performed by the simulink block "Inverse Park Transform", represented in the figure 3.8. Like the "Park Transform" block, it also has the sine and cosine of the flux angle as inputs.

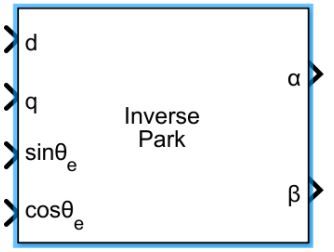

Figure 3.8: Inverse Park Transform (Simulink block)

3.6 Battery

For modelling the battery behaviour, a Lithium-Ion model was chosen. The reasons for this choice compared to other battery models are as follows:

- High energy density and good power density, helping to reduce the number of cells required and thereby the size of the battery.
- High energy efficiency
- High cycle life
- No maintenance required, reducing AGV maintenance costs

For its implementation, the Simulink "Battery" block was chosen, as can be seen in the following figure:

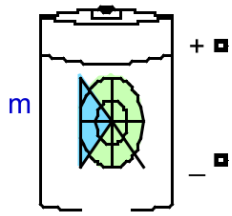

Figure 3.9: Battery (Simulink block)

And the following parameters have been set:

Table 3.7: Battery block parameters

Symbol	Value	Description
V_{rated}	84 V	Nominal voltage
C	150 Ah	Rated capacity
$\%SOC$	80%	Initial state-of-charge
t_r	30s	Battery response time

The effect of temperature and age were also ignored in the implementation.

Since batteries are usually constructed by a set of cells in series (or parallel), with a typical voltage of 12 V, the nominal voltage of the battery was 84 V so as to correspond to a multiple of 12 and, attending to equation x, the voltage V_{DC} required is about 75.42 V. The value of the voltage multiple of 12 that comes closest to this value is 72, below what is required. On the other hand, an oversizing of this voltage is positive in order to avoid over-modulation or to allow the motor to reach overload regimes. The value of the rated capacity adopted took into account the peak value of the rated motor current ($\sqrt{(2)} \cdot i_n$). As this is slightly higher than 120 A, the value of 150 Ah was adopted. With this capacity, if the AGV travels at 10 km/h, it will have an autonomy of a little

more than 1h. As for its initial state of charge, it was assumed that the battery would only charge until it reached 80% *SOC* to allow the AGV to perform regenerative braking. The response time was kept at its default value,

For the discharge simulation, this block has the option to estimate the parameters of the discharge curve from the nominal parameters of the battery. Three discharge curves were also chosen:

- $0.1 \cdot I_{peak}$
- $0.5 \cdot I_{peak}$
- I_{peak}

The resulting curves are represented in the following figure:

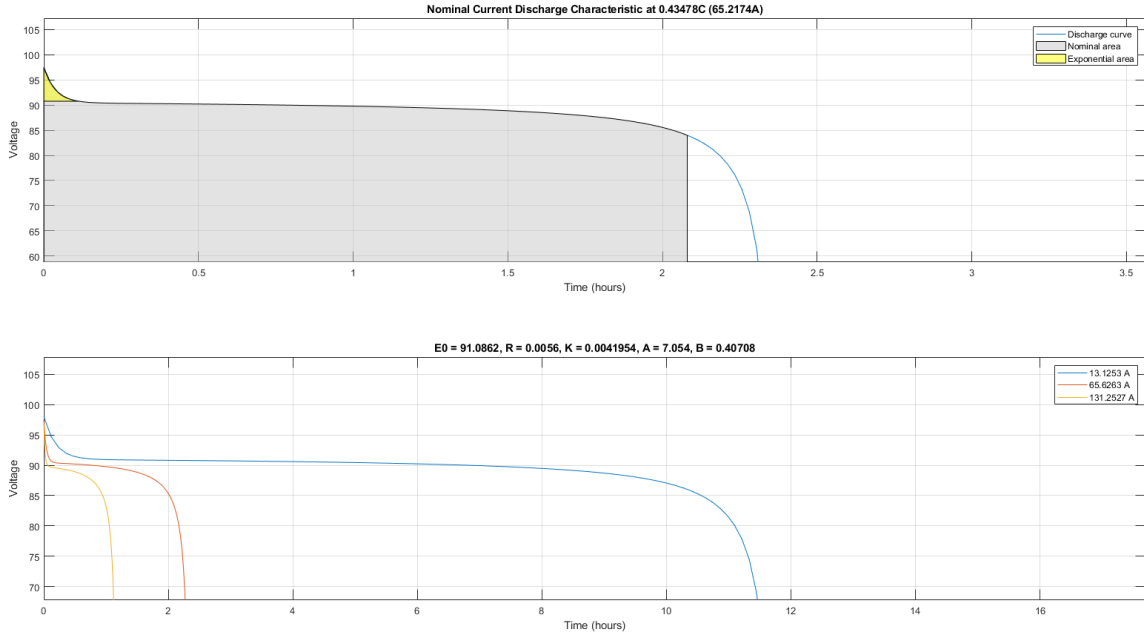

Figure 3.10: Battery (Simulink block)

3.7 Supervision block

This block is divided into two parts:

- Supervising the battery, measuring its state of charge, *SOC*, voltage at the output terminals, current and temperature;
- Calculation of the energy consumed by the vehicle taking into account the torque applied to the wheels and their speed.

As the simulation conditions are ideal, thus disregarding the effect of age and temperature on its performance, for battery supervision only $\%SOC$ was studied. For the calculation of the energy consumed by the drivetrain, the power calculation formula is taken into account:

$$P = T \cdot \omega \tag{3.28}$$

where T represents the torque and ω the angular speed of a rotating shaft. Since torque can be seen as the multiplication of an applied force by the radius distance, $F \cdot r$, and $\omega = \frac{v}{r}$, then the following relationship can be obtained:

$$P = F \cdot r \cdot \frac{v}{r} = F \cdot v \tag{3.29}$$

In this block, F represents the force applied to the wheels (georbox output torque multiplied by the radius of the wheels) and v the linear speed of the AGV.

For the energy calculation, the consumed power is integrated:

$$E_{drivetrain} = \int P\,dt \tag{3.30}$$

and its unit is Joule (J). Subsequently, the result of the integration is converted from Joule units to kilowatt-hours (kWh).

This conversion is done as follows:

$$E_{(kWh)} = \frac{E_{(J)}}{1000 \cdot 60 \cdot 60} = \frac{E_{(J)}}{3600000} \tag{3.31}$$

3.8 Conclusion

This chapter discussed why the different methods were chosen and how they were implemented. The options, above all, were intended to make better use of the DC bus voltage and more efficient. Besides optimization algorithms, it is in the powertrain control that a large portion of energy is managed, so it must be critically well studied and implemented.

Having in mind the academic learning objective, not always the most efficient methods were used, being used simpler methods in order to better understand its operation, as it is the case of the fieldweakening control. However, and given the fact that the AGV speed will not exceed much its nominal speed, a basic scheme will still perform well. Nevertheless, one issue that has not been well discussed in this chapter is overloading. Due to lack of knowledge on isolation related parameters, no algorithm has been implemented to effectively manage this area of operation. A good implementation would involve calculating the temperature and period for which the motor could operate at a certain overload without jeopardising its performance and safety.

The robustness of the methods adopted will be discussed in chapter 5, for which the results obtained will be presented and discussed.

Chapter 4

Study of a reliable Navigation System

4.1 Introduction

Taking into account the variation in atmospheric conditions and the amount of data and restrictions that other sensors present, the integration of GPS and INS was approached as a viable navigation solution for outdoor environments. On the other hand, this topic is currently arousing a lot of interest and research, with great expectations of use in autonomous driving vehicles.

Although the integration involves the calculation of variables associated with GPS, many of these become more difficult to calculate, especially in low-cost sensors. Therefore, in this chapter will be discussed the mechanization and characteristics of the INS and then the kalman filter equations, assuming that the GPS sensor provides the values of position, speed and time (PVT).

4.2 INS

4.2.1 INS mechanization

The INS mechanization equations will be expressed in local-level frame. According to [25], the main advantages of this reference frame are that it provides a intuitive solution to the user on or near the Earth's surface and the attitude angles can be obtained directly at the output of the mechanization equations when solved in the local-level frame since the axes of the l-frame are aligned to the local east, north and up directions [25].

The mechanization equations in local-level frame are the follows:

$$\begin{bmatrix} \dot{r}^l \\ \dot{v}^l \\ \dot{R}^l_b \end{bmatrix} = \begin{bmatrix} D^{-1}v^l \\ R^l_b f^b - (2\Omega^l_{ie} + \Omega^l_{el}v^l) + g^l \\ R^l_b(\Omega^b_{ib} - \Omega^b_{il}) \end{bmatrix} \tag{4.1}$$

These equations can be divided into position computation, speed computation and attitude computation, respectively. The step by step computation of navigation parameters is extensively described in [25], which is summarised as follows:

- Obtain rotation rates from the gyros (ω_x, ω_y, ω_z) and the accelerations from the accelerators (f_x, f_y, f_z) (both are in relation to the inertial frame resolved into the body frame).
- Calculate the attitude angles (p, r, A) (in terms of the rotation rates) and compute the rotation matrix (R_b^l)
- Transform the specific forces expressed in body frame to the navigation frame (f_e, f_n, f_u), using the rotation matrix.
- Calculate the local-level speeds (v_e, v_n, v_u) by integrating the transformed specific forces.
- Calculate the geodetic coordinates of position (φ, λ, h) by integrating the speeds.

The INS mechanization in local-level frame schema can be seen in the next figure:

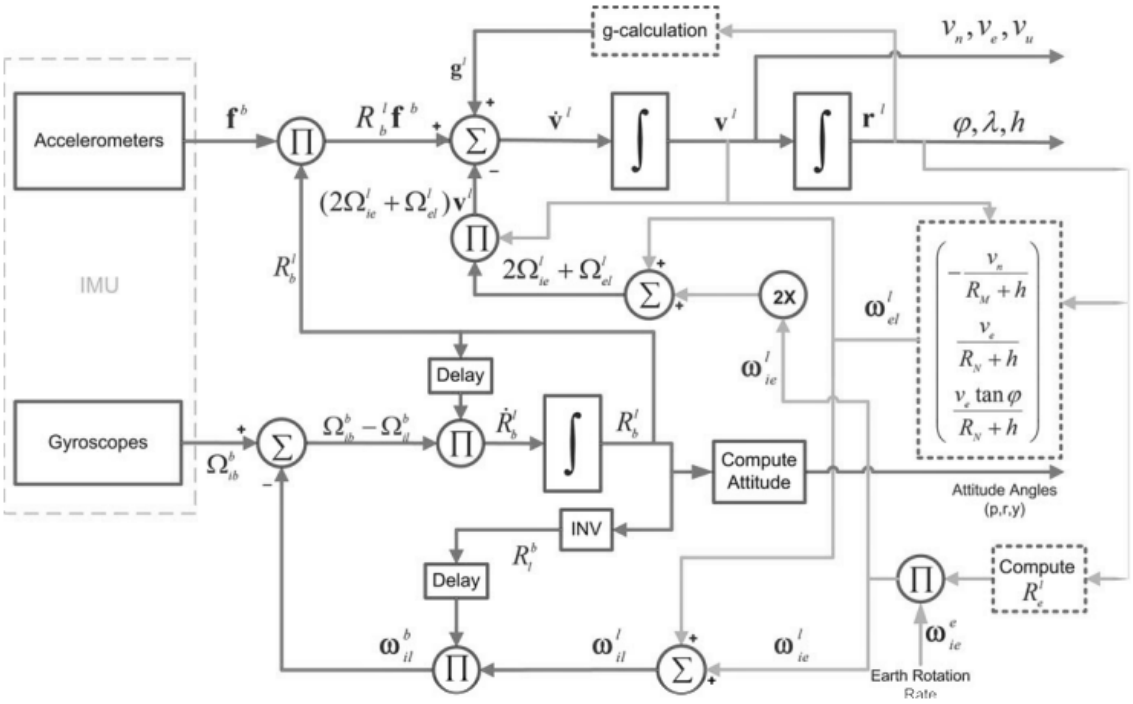

Figure 4.1: INS mechanization in local-level frame (adapted from [25])

4.2.2 Measurement data correction

Since any measurements contain deterministic errors that can be corrected, sensors are calibrated in factory and laboratory [20][25]. The results of this calibration lead to the following relationship:

$$\Delta\theta_{ib}^{b} = \begin{bmatrix} \frac{1}{1+S_x^g} & 0 & 0 \\ 0 & \frac{1}{1+S_y^g} & 0 \\ 0 & 0 & \frac{1}{1+S_z^g} \end{bmatrix} \cdot (\Delta\tilde{\theta}_{ib}^{b} - d_{gyro} \cdot \Delta_t) \tag{4.2}$$

$$\Delta v^b = \begin{bmatrix} \frac{1}{1+S_x^a} & 0 & 0 \\ 0 & \frac{1}{1+S_y^a} & 0 \\ 0 & 0 & \frac{1}{1+S_z^a} \end{bmatrix} \cdot (\Delta \tilde{v}^b - b_{acc} \cdot \Delta_t) \tag{4.3}$$

where:

d_{gyro}	is the drift of gyroscope in $radians/s$
$S^g_{x,y,x}$	is the gyroscope scale factor in ppm
b_{acc}	is the accelerometer bias in m/s^2
$S^a_{x,y,x}$	is the accelerometer scale factor in ppm
$\Delta\theta^b_{ib}$	is the corrected incremental gyroscope output in $radians/sec$
Δv^b	is the corrected incremental accelerometer output in m/s

4.2.3 Attitude computation

The attitude computation is performed using quarternions since it is robustness against singularities and computational efficient [20]. A quarternion can be expressed as:

$$q = (q_1 q_2 q_3 q_4)^T \tag{4.4}$$

where:

$$q_1^2 + q_1^2 + q_3^2 + q_4^2 = 1 \tag{4.5}$$

A closed form solution of the quaternion equation is presented in [25] and [20], and can be expressed as:

$$\dot{q} = \frac{1}{2} \cdot \Omega(\omega) \cdot q = \frac{1}{2} \cdot \begin{bmatrix} 0 & \omega_z & -\omega_y & \omega_x \\ -\omega_z & 0 & \omega_x & \omega_y \\ \omega_y & -\omega_x & 0 & \omega_z \\ -\omega_x & -\omega_y & -\omega_z & 0 \end{bmatrix} \cdot q \tag{4.6}$$

Using the angular increments, the quarternion equation update can be written as follows:

$$\begin{bmatrix} q_1 \\ q_2 \\ q_3 \\ q_4 \end{bmatrix}_{t+1} = \begin{bmatrix} q_1 \\ q_2 \\ q_3 \\ q_4 \end{bmatrix}_t + \begin{bmatrix} c & s \cdot \Delta\theta_z & -s \cdot \Delta\theta_y & s \cdot \Delta\theta_x \\ -s \cdot \Delta\theta_z & c & s \cdot \Delta\theta_x & s \cdot \Delta\theta_y \\ s \cdot \Delta\theta_y & -s \cdot \Delta\theta_x & c & s \cdot \Delta\theta_z \\ -s \cdot \Delta\theta_x & -s \cdot \Delta\theta_y & -s \cdot \Delta\theta_z & c \end{bmatrix} + \begin{bmatrix} q_1 \\ q_2 \\ q_3 \\ q_4 \end{bmatrix}_t \tag{4.7}$$

where:

$$\Delta\theta = \sqrt{\Delta\theta_x^2 + \Delta\theta_y^2 + \Delta\theta_z^2}$$
$$c = 2 \cdot (\cos(\tfrac{\Delta\theta}{2}) - 1)$$
$$s = \tfrac{2}{\Delta\theta} \cdot \sin(\tfrac{\Delta\theta}{2})$$

According to [25], the rotation rate of the l-frame due to the Earth's rotation rate, ω_{ie}^{l}, and movement on the curved surface of the Earth, ω_{el}^{l}, must be compensated from the measured angular rate of the body ω_{ib}^{b} prior to integration. Thus, as:

$$\omega_{ie}^{l} = \begin{bmatrix} 0 \\ \Omega^{e} cos\varphi \\ \Omega^{e} sin\varphi \end{bmatrix} \rightarrow \Omega_{ie}^{l} = \begin{bmatrix} 0 & -\omega^{e} sin\varphi & \omega^{e} cos\varphi \\ \omega^{e} sin\varphi & 0 & 0 \\ -\omega^{e} cos\varphi & 0 & 0 \end{bmatrix} \tag{4.8}$$

$$\omega_{el}^{l} = \begin{bmatrix} -\frac{v_n}{R_M+h} \\ \frac{v_e}{R_n+h} \\ \frac{v_e \tan\varphi}{R_n+h} \end{bmatrix} \rightarrow \Omega_{el}^{l} = \begin{bmatrix} 0 & -\frac{v_e \tan\varphi}{R_N+h} & \frac{v_e}{R_N+h} \\ \frac{v_e \tan\varphi}{R_N+h} & 0 & \frac{v_n}{R_M+h} \\ -\frac{v_e}{R_N+h} & -\frac{v_n}{R_M+h} & 0 \end{bmatrix} \tag{4.9}$$

and:

$$\omega_{il}^{b} = \omega_{ie}^{l} + \omega_{el}^{l} \tag{4.10}$$

$$\omega_{lb}^{b} = \omega_{ib}^{b} + \omega_{il}^{b} \tag{4.11}$$

It can then be concluded that:

$$\begin{aligned} \Delta\theta_{lb}^{b} &= (\Delta\theta_x \Delta\theta_y \Delta\theta_z)^T \\ &= \Delta\theta_{ib}^{b} - \Delta\theta_{il}^{b} \\ &= \Delta\theta_{ib}^{b} - R_{l}^{b} \cdot (\omega_{ie}^{l} + \omega_{el}^{l}) \cdot \Delta_t \cdot R_{l}^{b} \end{aligned} \tag{4.12}$$

4.2.3.1 Rotation Matrix

The rotation matrix, using quaternions, can be written as follows:

$$R_{b}^{l} = \begin{bmatrix} q_1^2 - q_2^2 - q_3^2 + q_4^2 & 2(q_1 q_2 - q_3 q_4) & 2(q_1 q_3 + q_2 q_4) \\ 2(q_1 q_2 + q_3 q_4) & -q_1^2 + q_2^2 - q_3^2 + q_4^2 & 2(q_2 q_3 - q_1 q_4) \\ 2(q_1 q_3 - q_2 q_4) & 2(q_2 q_3 + q_1 q_4) & -q_1^2 - q_2^2 + q_3^2 + q_4^2 \end{bmatrix} \tag{4.13}$$

and the pitch, roll and yaw angle can be calculated through the equations 2.94, 2.96 and 2.95, respectively.

4.2.4 Speed computation

The mechanization equation for the rate change of speed, expressed in l-frame [25], can be calculated using the following formula:

$$\Delta v^{l} = \Delta\tilde{v}^{l} - (2\Omega_i e^{l} + \Omega_e l^{l}) v^{l} \Delta_t + g^{l} \Delta_t \tag{4.14}$$

where:

$\Delta\tilde{v}^l$	is the measured speed increment in l-frame
$(2\Omega_i e^l + \Omega_e l^l)v^l\Delta_t$	is the Coriolis correction that compensates for the Earth's rotation and the resulting change of orientation of the l-frame [25].
$g^l\Delta_t$	is the gravity correction

In the local-level frame, the z-axis is normal to the ellipsoid, thus the normal gravity vector have the following form:

$$g^l = \begin{bmatrix} 0 & 0 & -g \end{bmatrix}^T \tag{4.15}$$

and g is calculated using the equation 2.87.

4.2.5 Position computation

For position computation, it is important to define the transformation matrix between the speed components in l-frame and the derivative of geographic coordinates:

$$D^{-1} = \begin{bmatrix} 0 & \frac{1}{R_M+h} & 0 \\ \frac{1}{(R_N+h)cos\varphi} & 0 & 0 \\ 0 & 0 & 1 \end{bmatrix} \tag{4.16}$$

Thus, the rate of change of the position vector can be written as follows:

$$r^l_{t+1} = r^l_t + \frac{1}{2}\cdot D^{-1}\cdot(v^l_t + v^l_{t+1})\cdot\Delta_t \tag{4.17}$$

4.3 GPS/INS integration method

For the GPS and INS integration, the strategy chosen is the loosely coupled since on the AGV route there will be no tall buildings or trees and the fact that this algorithm is the simplest and most computationally efficient. As explained earlier, this method is based on the Kalman Filter, so it is divided into two parts:

- System model
- Measurement model

Thus, the method for the initial alignment of the IMU will now be studied and subsequently the kalman filter equations will be presented.

4.3.1 Kalman Filter equations

4.3.1.1 System Model

The system model equation is given by:

$$\delta \dot{x} = F\delta x + Gw \tag{4.18}$$

δx is the state vector and is defined as:

$$\delta x^{l}_{15\times 1} = \left[\delta r^{l}_{3\times 1}, \quad \delta v^{l}_{3\times 1}, \quad \varepsilon^{l}_{3\times 1} \quad \delta\omega_{3\times 1} \quad \delta f_{3\times 1}\right]^{T} \tag{4.19}$$

where:

δr^{l}	is the position error vector ($\delta\varphi$, $\delta\lambda$, δh)
δv^{l}	is the Earth-referenced speed error vector (δv_e, δv_n, δv_u)
ε^{l}	is the attitude error vector (δp, δr, δy)
$\delta\omega$	is the gyroscope error vector (drifts) ($\delta\omega_x$, $\delta\omega_y$, $\delta\omega_z$)
δf	is the accelerometer error vector (biases) (δf_X, δf_y, δf_z)

G is the noise distribution vector, which includes the variances associated with the state vector [25]. As stated in 2.6.4.5, the INS errors can be modeled by using the 1st order Gauss Markov process. This model is valid for a stationary Gaussian process that has an exponential autocorrelation [26]. The figure 4.2 has represented the autocorrelation sequence of this process:

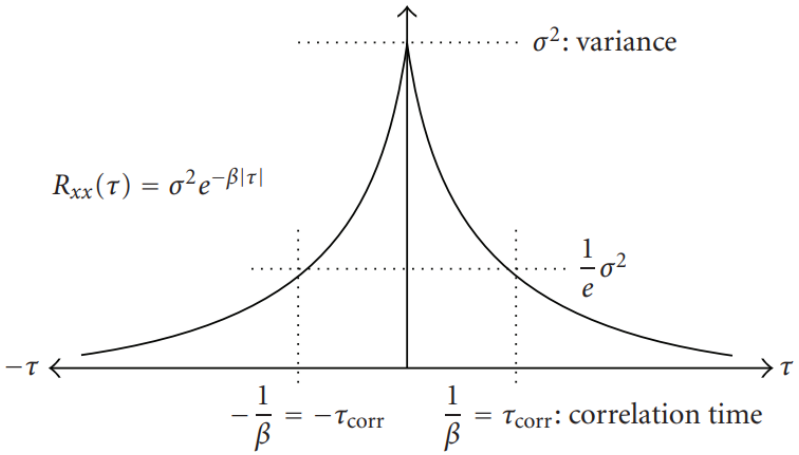

Figure 4.2: Autocorrelation sequence of a 1st-order Gauss-Markov process [26]

The first-order Gauss-Markov process can be described through the following equation:

$$\dot{x}(t) = -\beta x(t) + \sqrt{2\sigma^2\beta}w(t) \tag{4.20}$$

and in its discrete-time domain form:

$$x_k = (I - \beta\Delta_t)x_{k-1} + \sqrt{2\sigma^2\beta}w_k\Delta_t \tag{4.21}$$

where:

β	is the reciprocal of the correlation time of the random process.
σ	is the e standard deviation of this random process.
$w(t)$	is unity variance white Gaussian noise.

Hence, the vector G can be written as follows:

$$G = \begin{bmatrix} \sigma_{r,1\times3} \\ \sigma_{v,1\times3} \\ \sigma_{\varepsilon,1\times3} \\ \sigma_{\omega,1\times3} \\ \sigma_{f,1\times3} \end{bmatrix} = \begin{bmatrix} \sigma_{\varphi} \\ \sigma_{\lambda} \\ \sigma_{h} \\ \sigma_{ve} \\ \sigma_{vn} \\ \sigma_{vu} \\ \sigma_{p} \\ \sigma_{r} \\ \sigma_{y} \\ \sqrt{2\beta_{\omega x}\sigma_{\omega x}^2} \\ \sqrt{2\beta_{\omega y}\sigma_{\omega y}^2} \\ \sqrt{2\beta_{\omega z}\sigma_{\omega z}^2} \\ \sqrt{2\beta_{fx}\sigma_{fx}^2} \\ \sqrt{2\beta_{fy}\sigma_{fy}^2} \\ \sqrt{2\beta_{fz}\sigma_{fz}^2} \end{bmatrix} \tag{4.22}$$

where:

$\beta_{\omega xyz}$	are the reciprocals of the correlation times associated with the autocorrelation sequence of the gyroscope error
$\beta_{f_{xyz}}$	are the reciprocals of the correlation times associated with the autocorrelation sequence of the accelerometer error
$\sigma_{\omega xyz}$	are the gyroscope errors variances
σ_{fxyz}	are the accelerometers errors variances

w is the unit-variance white Gaussian noise and F is the dynamic coefficient matrix, defined as:

$$F = \begin{bmatrix} 0_{3\times3} & F_r & 0_{3\times3} & 0_{3\times3} & 0_{3\times3} \\ 0_{3\times3} & 0_{3\times3} & F_v & 0_{3\times3} & R_b^l \\ 0_{3\times3} & F_{\varepsilon} & 0_{3\times3} & R_b^l & 0_{3\times3} \\ 0_{3\times3} & 0_{3\times3} & 0_{3\times3} & F_{\omega} & 0_{3\times3} \\ 0_{3\times3} & 0_{3\times3} & 0_{3\times3} & 0_{3\times3} & F_f \end{bmatrix} \tag{4.23}$$

where:

$$F_r = \begin{bmatrix} 0 & \frac{1}{R_M+h} & 0 \\ \frac{1}{(R_n+h)\cos\varphi} & 0 & 0 \\ 0 & 0 & 1 \end{bmatrix} \tag{4.24}$$

$$F_v = \begin{bmatrix} 0 & f_u & -f_n \\ -f_u & 0 & f_e \\ f_n & -f_e & 0 \end{bmatrix} \tag{4.25}$$

$$F_\varepsilon = \begin{bmatrix} 0 & \frac{1}{R_m+h} & 0 \\ -\frac{1}{R_n+h} & 0 & 0 \\ -\frac{-\tan\varphi}{R_n+h} & 0 & 0 \end{bmatrix} \tag{4.26}$$

$$F_\omega = \begin{bmatrix} \beta_{\omega x} & 0 & 0 \\ 0 & \beta_{\omega y} & 0 \\ 0 & 0 & \beta_{\omega z} \end{bmatrix} \tag{4.27}$$

$$F_f = \begin{bmatrix} \beta_{f_x} & 0 & 0 \\ 0 & \beta_{f_y} & 0 \\ 0 & 0 & \beta_{f_z} \end{bmatrix} \tag{4.28}$$

On the basis of equation 2.108 and 2.110, the system model can be rewritten as follows:

$$\delta x_k = (I + F\Delta_t)\delta x_{k-1} + G\Delta_t w_{k-1} \tag{4.29}$$

4.3.1.2 Measurement Model

The discrete-time measurement model equation is as follows:

$$\delta z_k = H_k \delta x_k + \eta_k \tag{4.30}$$

where:

$$\delta z_k = \begin{bmatrix} r^l_{INS} - r^l_{GPS} \\ v^l_{INS} - v^l_{INS} \end{bmatrix} = \begin{bmatrix} \varphi_{INS} - \varphi_{GPS} \\ \lambda_{INS} - \lambda_{GPS} \\ h_{INS} - h_{GPS} \\ v_{e,INS} - v_{e,GPS} \\ v_{n,INS} - v_{n,GPS} \\ v_{u,INS} - v_{u,GPS} \end{bmatrix} \tag{4.31}$$

H_k is the measurement design matrix at time t_k, having the following formula:

$$H_k = \begin{bmatrix} I_{6\times6} & 0_{6\times9} \end{bmatrix} \tag{4.32}$$

η_k is the zero-mean measurement noise vector with covariance R_k:

$$\eta_k = \begin{bmatrix} \eta_r \\ \eta_v \end{bmatrix}_k = \begin{bmatrix} \eta_\varphi \\ \eta_\lambda \\ \eta_h \\ \eta_{ve} \\ \eta_{vn} \\ \eta_{vu} \end{bmatrix}_k \tag{4.33}$$

$$R_k = \begin{bmatrix} \sigma_\varphi^2 & 0 & 0 & 0 & 0 & 0 \\ 0 & \sigma_\lambda^2 & 0 & 0 & 0 & 0 \\ 0 & 0 & \sigma_h^2 & 0 & 0 & 0 \\ 0 & 0 & 0 & \sigma_{ve}^2 & 0 & 0 \\ 0 & 0 & 0 & 0 & \sigma_{vn}^2 & 0 \\ 0 & 0 & 0 & 0 & 0 & \sigma_{vu}^2 \end{bmatrix} \tag{4.34}$$

4.4 Conclusion

It was then studied a method that promises to be able to present a robust navigation with less error. GPS/INS becomes the best candidate taking into account that the characteristics of both methods are complementary, helping their integration. This integration is made easier by the fact that GPS errors tend to be constant, i.e. they vary little over time. On the other hand, INS errors tend to increase given the integrative nature of its mechanization process, causing the error to increase with each iteration. Thus, good modelling of both errors and integration of the two methods will allow the overall error of the system to be reduced.

The integration method chosen should also be taken into account: loosely coupled. Although this method can solve the problems of INS errors, it is not compatible with environments where the number of visible satellites is low or the presence of trees or tall buildings. In the AGV path there will not be these limitations, however, if there is any failure in the GPS signal reception, the system is unable to correct the INS errors, so these failures cannot be extended. However, given the low speed of the AGV, a loss of GPS signal does not represent long distances travelled, so these failures could also be mitigated by incorporating other navigation methods, such as odometry.

Chapter 5

Results and discussion

5.1 Introduction

This chapter aims at presenting the results obtained in the powertrain simulation and the implementation of the navigation subsystem. As previously clarified, of the latter, it was only possible to implement and test the GPS behaviour. Therefore, this chapter will be divided into two parts: powertrain simulation and GPS implementation and results.

5.2 Powertrain simulation

5.2.1 Characterization of the simulation

To study the dynamic and electrical behaviour of the powertrain, a single simulation of 240 seconds was carried out under the following conditions:

- The mass of AGV is equal to 5000 kg.
- The vehicle speed reference was always 10 km/h.
- The AGV starts its movement from rest.
- A new limit was added to the current i_q: not to exceed $\sqrt{2}i_n$.
- The slope of the ground varies in step for the study of the response of the controllers to such a disturbance. The way the slope varies can be seen in the following figure:

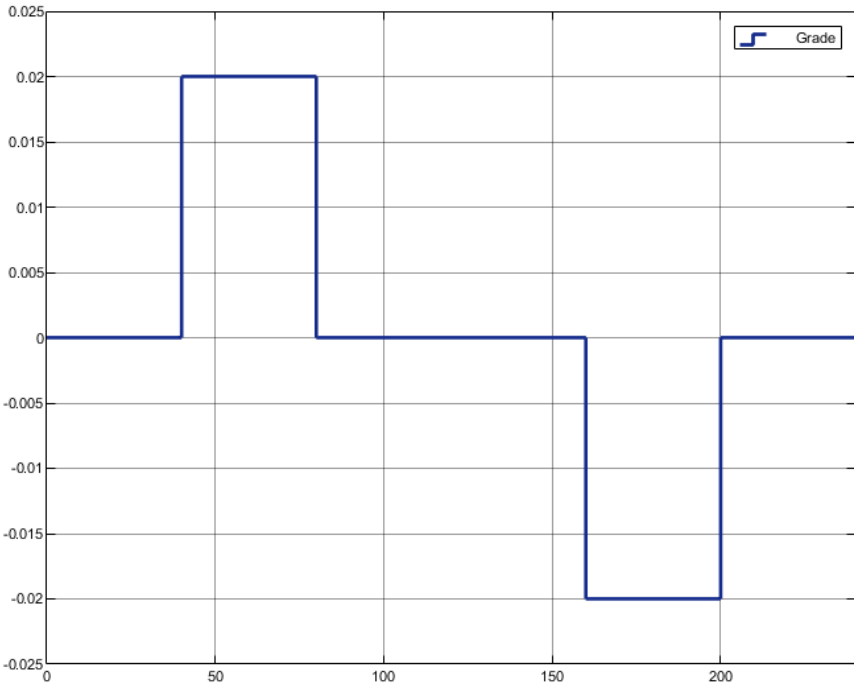

Figure 5.1: Slope of the route

As can be seen in figure 5.1, the variation in the slope of the route during the simulation was as follows:

1. 0% from 0*s* to 40*s*
2. 2% from 40*s* to 80*s*
3. 0% from 80*s* to 160*s*
4. -2% from 160*s* to 200*s*
5. 0% from 200*s* to 240*s*

5.2.2 System outputs

The outputs of the system are the result of the control action. In this case, it will be the creation of the movement and the value of the variables that directly or indirectly influence it. Thus, the simulation results for the following quantities will be discussed:

- Vehicle speed
- Acceleration
- Motor electromagnetic torque
- Load torque
- Rotor angular speed

5.2.2.1 Results

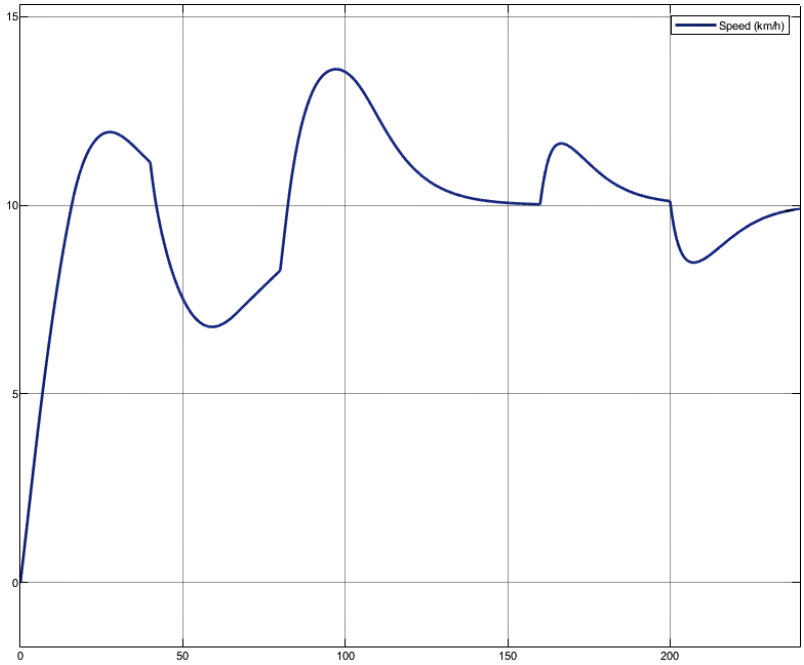

Figure 5.2: AGV speed (km/h)

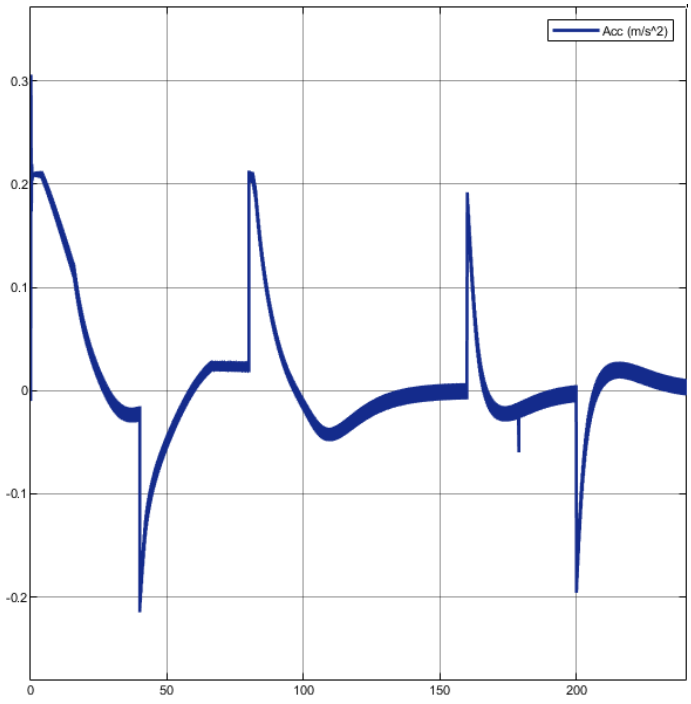

Figure 5.3: AGV acceleration (m/s^2)

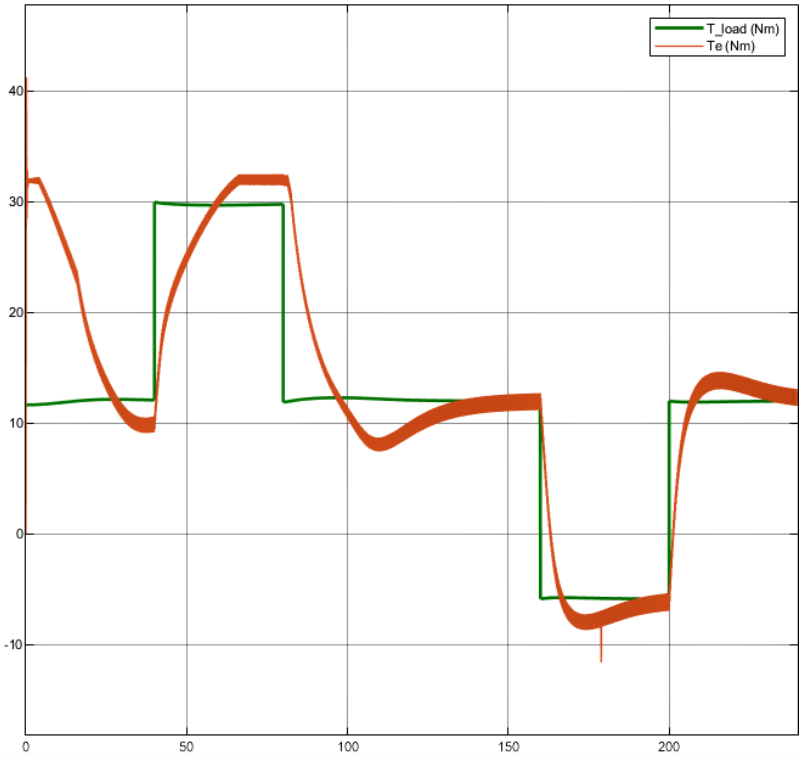

Figure 5.4: Electromagnetic torque (orange) and load torque (green) (*Nm*)

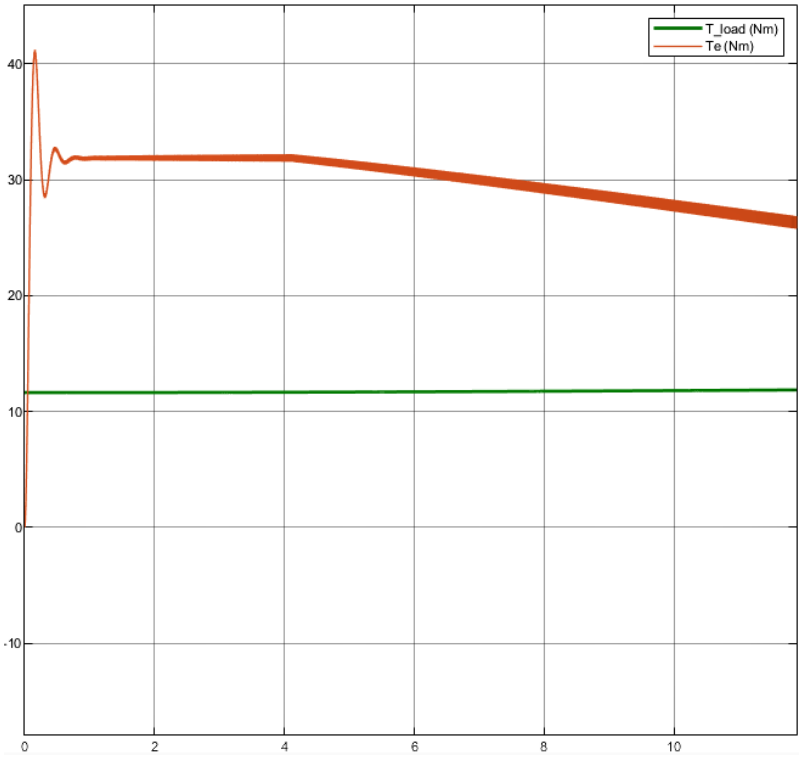

Figure 5.5: Electromagnetic torque (orange) and load torque (green) (*Nm*) at the first seconds of simulation

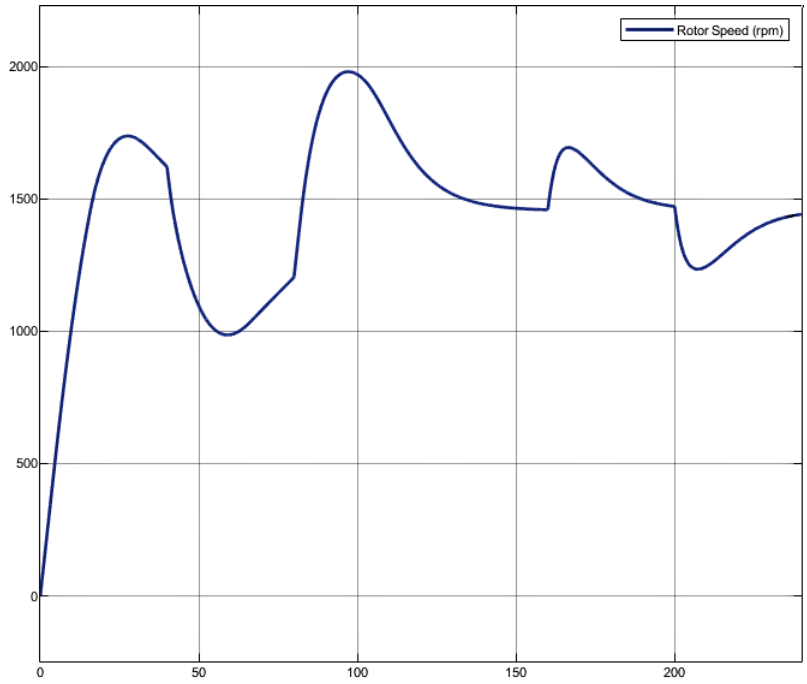

Figure 5.6: Rotor mechanical angular speed (rpm)

5.2.2.2 Discussion

From the results it is possible to conclude that the response of the system to the step is slow. However, the presence of overshoot in the speed curve leads to validate the thesis that the speed of dynamic response is highly influenced by the large inertia of the system, a consequence of the high weight of the AGV+load set, and not so much by the correct tuning of the gains of the controllers. Based on figure 5.5, it can be verified that the electromagnetic torque reaches overload values, but only lasts for a few seconds. Nevertheless, from 40 s to 80 s it could reach overload values, but it is limited in its nominal value. This limitation has its origin in the limitation of the maximum value of the i_q reference but is also due to other factors:

- As the torque is seen as the vector product of the stator current and the flux between the air gap, in order to reach overload values it is also necessary to ensure the correct magnetization of the machine, so also the i_d reference must be increased.

Regarding the speed, in this simulation it is concluded that the AGV reaches its reference value from 150s, which is verified by the fact that the electromagnetic torque of the motor follows the load torque in order to keep the speed constant. It is also possible to verify the proper functioning of the control in field weakening. During the first 50s, there is an overshoot in the vehicle speed, which can be seen from figure 5.6 that the motor reaches speeds higher than its nominal speed. However, in the torque curve there is an initial exponential decrease of its value, explained by the reduction of the i_d reference with the speed increase.

From 160 to 200s it is also possible to validate the motor's ability to effect regenerative braking. Since the speed was already close to its reference value, when starting the descent, the motor

torque follows the value of the load torque which has its negative value due to the effect of gravity on a descent. However, it must be taken into account that the response of the system to the step is not the fastest, so that for some seconds there are speed values higher than its reference or lower in the response of the system the last 2 steps.

5.2.3 Outer Control

It will now be presented and discussed the results of the outer control, that is, to verify the response of the speed controller and what current references were given to the system. As discussed above, it will also be studied the i_d reference reduction in field weakening region.

5.2.3.1 Results

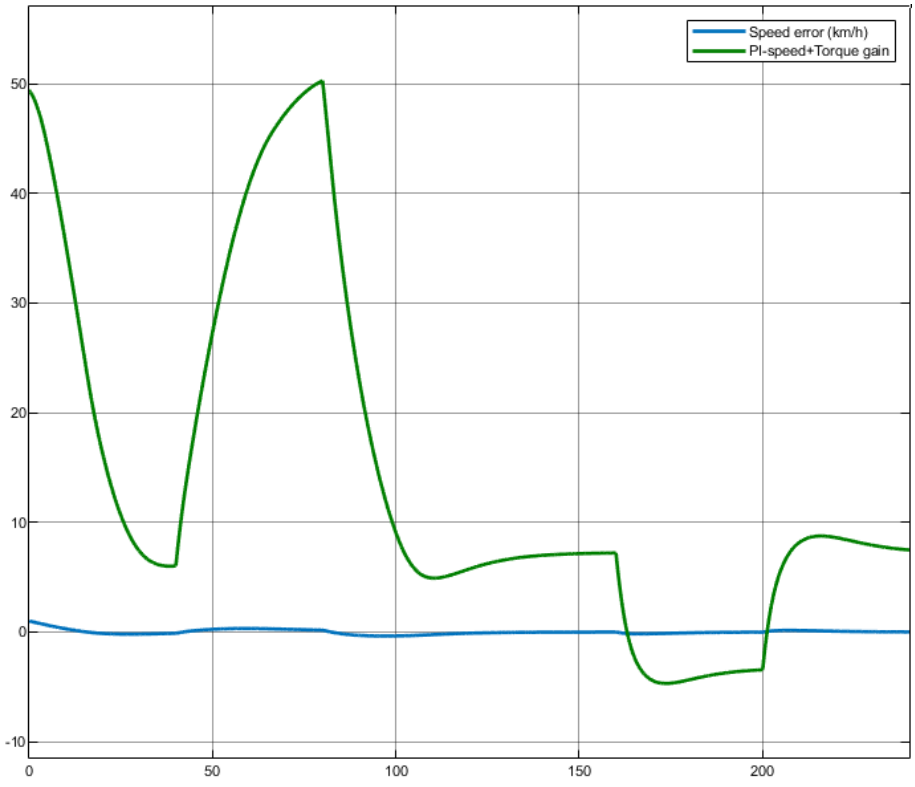

Figure 5.7: PI speed output multiplied by T_n (green) (Nm)

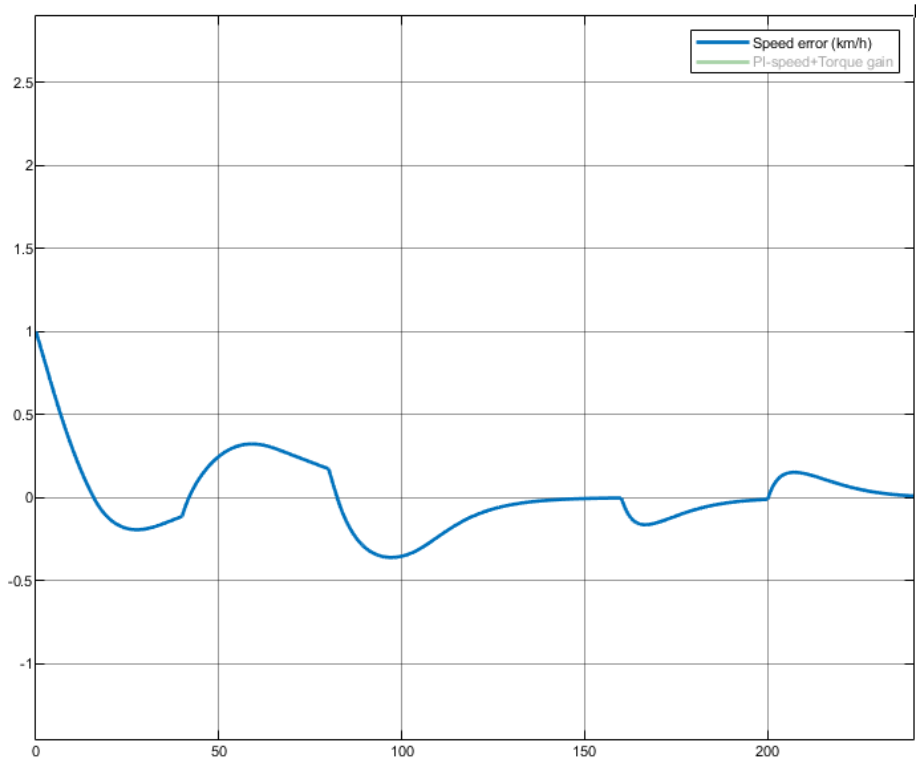

Figure 5.8: Normalized speed error

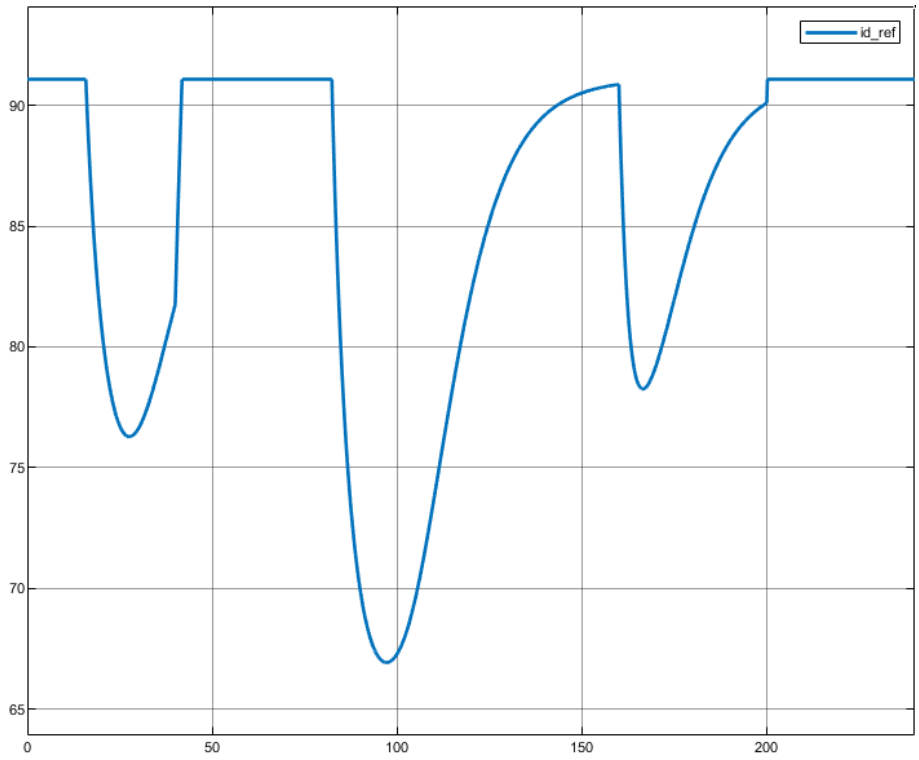

Figure 5.9: i_{d-ref} (A)

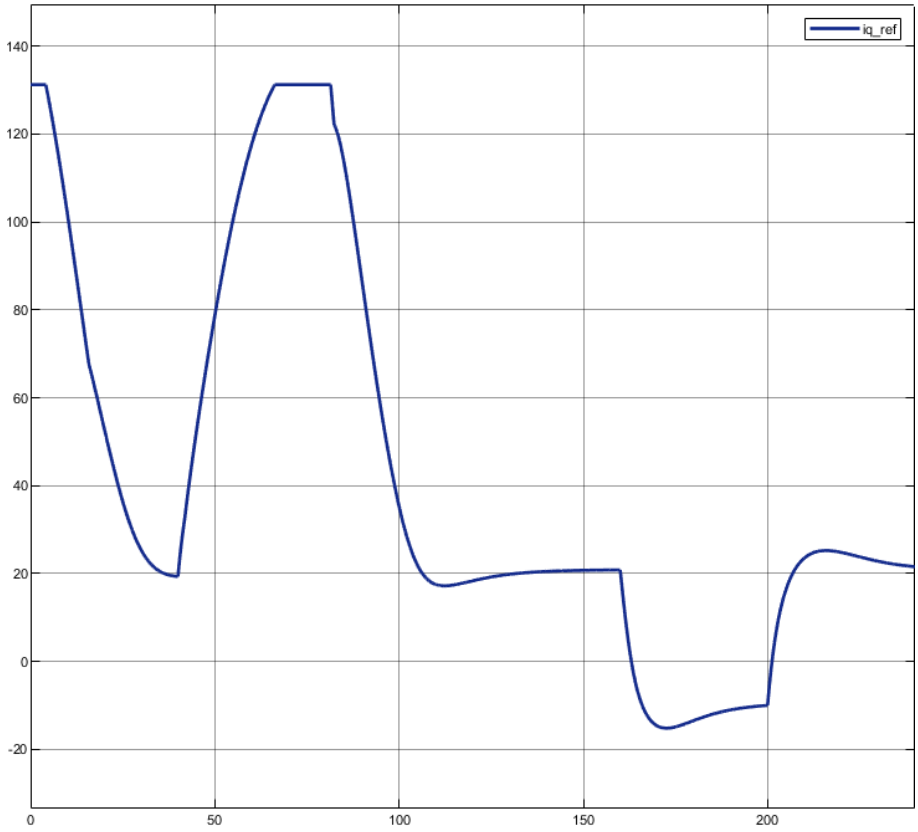

Figure 5.10: i_{q-ref} (A)

5.2.3.2 Discussion

At the initial instants, the output of the PI speed multiplied by T_n, figure 5.7, starts from overload values. This is due to the linear gain of the controller ($k_p = 1.5$) and the fact that at the beginning of the simulation, the speed error is maximum. On the other hand the slope of the output descent of this is a result of the integrative gain that the higher it is, the lower it will be, applying for more time a higher torque reference. However, and as verified previously, the speed response presents overshoot, which concludes that the value of the integrative gain cannot be too high under the consequence of increasing even more the response overshoot. A high proportional gain would also cause a saturation of the response, i.e. torque reference values much higher than the nominal value. If the value of the proportional gain were much higher than the integrative gain, the response of the system would be very fast, although reaching saturation values, but with the disadvantage of not correcting the error in the steady state. It is clear that the application band of this controller is limited by the inertia of the system.

Figure 5.10 shows the evolution of the i_q reference, for which it is possible to verify its saturation, not allowing it to be higher than $\sqrt{(2)}I_n$. After 160 s, it takes negative values in order to allow the engine to perform regenerative braking. In contrast, figure 5.9 shows the evolution of the reference i_d. Note that this always takes positive values since the electric motor, even during regeneration, needs to be magnetized, representing a reactive power consumption. Comparing figure

5.9 with figure 5.6, whenever the rotor angular speed exceeds its nominal values, the i_d reference decreases inversely proportional to the speed increase above nominal values. This way, a correct functioning of the field weakening control is verified.

5.2.4 Inner control

We will now study the response of the inner control. It is important to emphasize that its response must be faster than the outer control in order to quickly apply the generated references to the motor.

5.2.4.1 Results

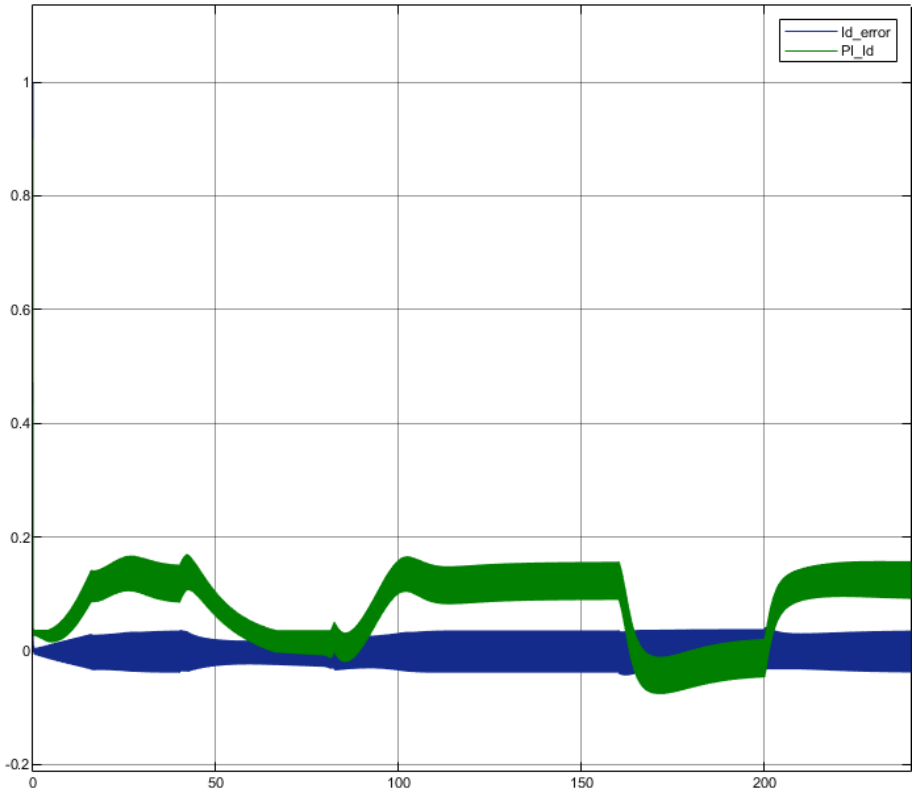

Figure 5.11: PI response (green) and error of i_d (blue)

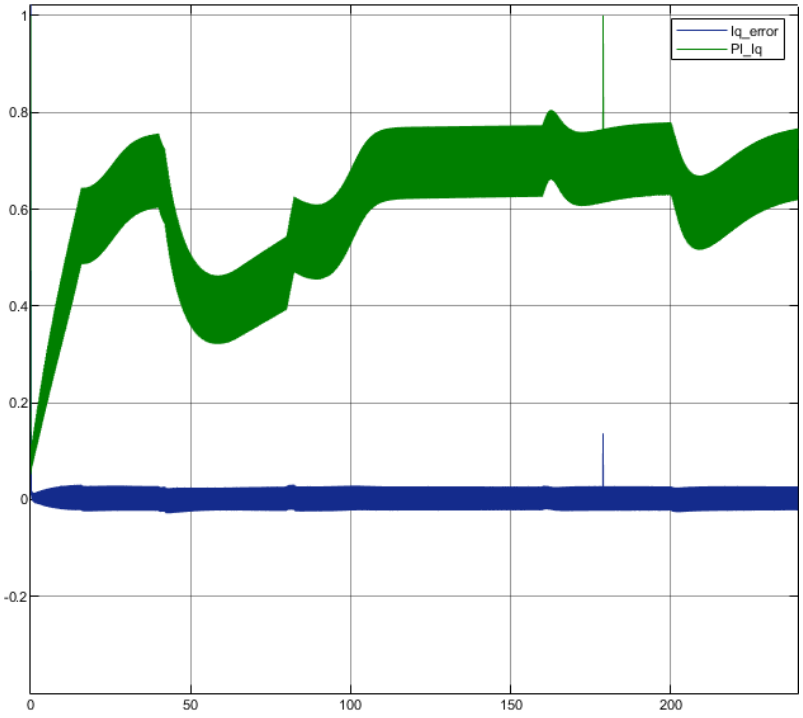

Figure 5.12: PI response (green) and error of i_q (blue)

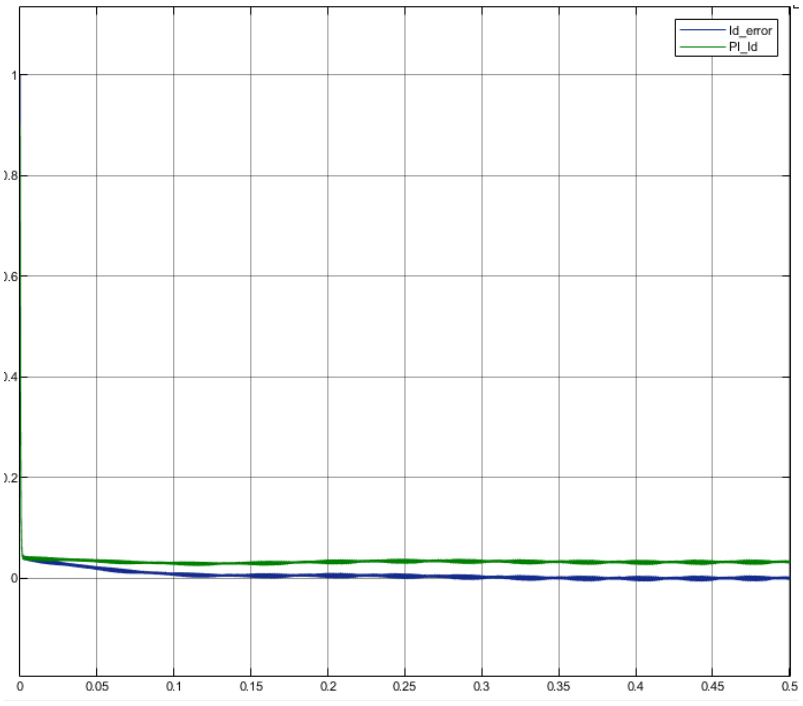

Figure 5.13: Transient PI response (green) and error of i_d (blue)

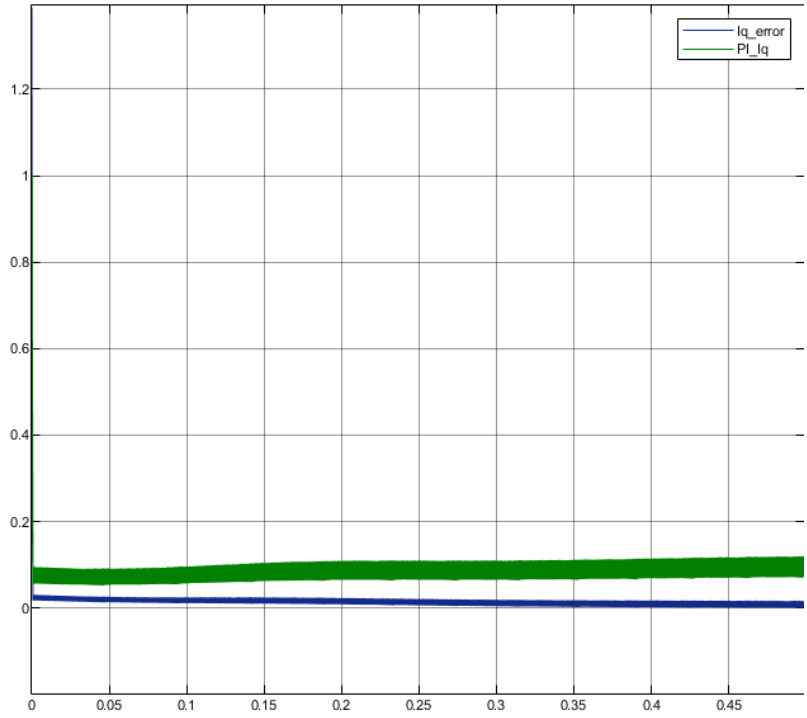

Figure 5.14: Transient PI response (green) and error of i_q (blue)

5.2.4.2 Discussion

As discussed in chapter 3, the error of the currents has been normalised, so the expected response will remain between values between -1 and 1. Evaluating the results, it can be seen that the error of the currents is cancelled out and throughout the simulation it remains at values close to 0, which means that the references created are applied to the motor. Through 5.13 and 5.14 figures, the transient response of the controllers is evaluated in order to study their speed. In both cases the response reaches its steady state regime before 0.5 s, thus verifying that the response of these controllers is faster than the response of the external control. Looking at figure 5.11, it is possible to observe a lot of oscillations that result in ripple in the electromagnetic torque. These oscillations are another criterion to be added to the fact that the use of a PID controller in this situation would be harmful since the response of the derivative component would compromise the performance of the system because the noise derivative varies rapidly in magnitude and sign.

In the first 50 s, the output of the i_q PI controller increases, figure 5.12. This is justified by the fact that the speed of the AGV increases slowly. Thus, as the rotor speed increases, the slip decreases, which would tend to cause the electromagnetic torque to decrease as well. So, in order for the torque value to remain constant, it is necessary to increase the voltage applied to the motor. As the *id* response remains constant, that is, the machine is magnetized, it is then necessary to increase the q component (torque component) to compensate for this effect and thus produce the desired torque.

5.2.5 Energy Consumption

For the study of energy consumption, only the consumption of the vehicle will be studied. The SOC of the battery was not considered since for a 240s simulation, it is not enough time for significant discharges in the battery.

5.2.5.1 Results

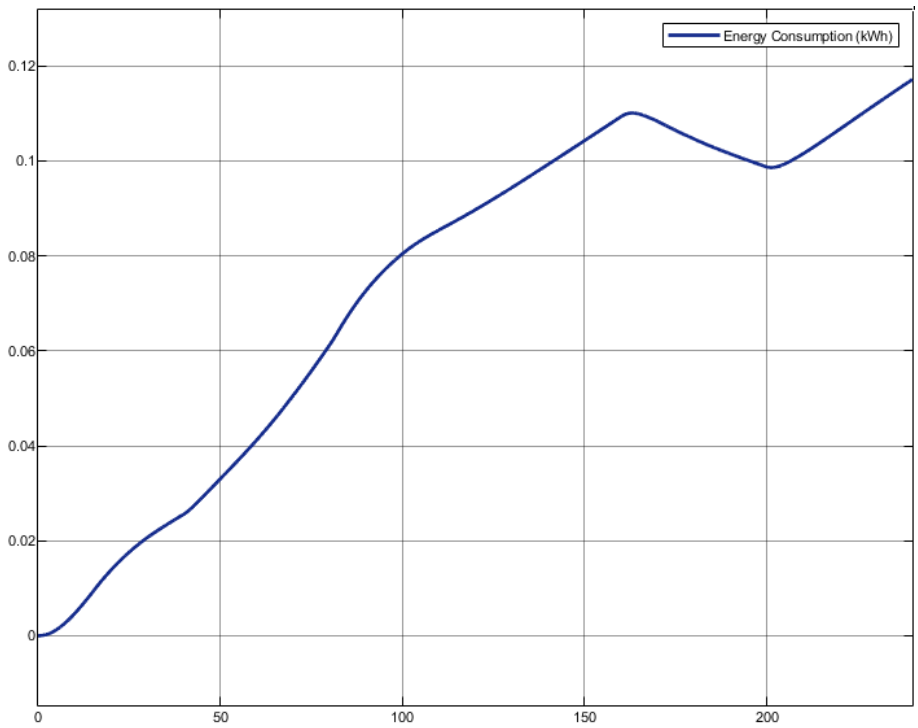

Figure 5.15: Vehicle Energy Consumption (kWh)

5.2.5.2 Discussion

Taking into account that the energy consumed during the movement of the AGV is kinetic energy, whose calculation formula is as follows:

$$E = \frac{1}{2} \cdot m \cdot v^2 \tag{5.1}$$

It is possible to validate that it varies with the square of the speed. This variation is particularly visible in the first 40s of the simulation. The speed of the AGV increases, so the energy consumed increases exponentially.

A positive value represents energy consumption, leading to battery decarging. A negative consumption or decrease of it, is an indicator of electric regeneration. From 160s to 200s, the AGV is on a downhill slope with the reference speed already reached. This way, the electromagnetic torque also takes negative values, following the load torque. This sign variation represents the electric regeneration, so the power direction is inverted. In other words, the engine starts producing

electrical energy, making it possible to charge the battery. As a consequence, the consumption curve has a negative slope, as shown in figure 5.15.

5.3 GPS implementation and results

To study and validate a GPS-based navigation solution, the Adafruit Ultimate GPS Breakout Version 3 sensor and an Arduino Mega were used.

5.3.1 GPS sensor

The GPS sensor datasheet and supporting material can be found here: [27]. Among others, the main features of this sensor are:

- 22 tracking satellites and 66 searching
- Update rate: 1 to 10 Hz
- Position accuracy: < 3m
- Speed accuracy: 0.1 m/s
- Acquisition sensitivity: -145 dBm
- Tracking sensitivity: -165 dBm
- Hot start: 1 second typical
- Warm start: 33 seconds typical
- Cold start: 35 seconds typical
- Output: NMEA sentences at 9600 bps (baud rate)

The NMEA sentences description can be found in the sensor datasheet and can be studied in the next image:

Table-1: NMEA Output Sentence	
Option	**Description**
GGA	Time, position and fix type data.
GSA	GPS receiver operating mode, active satellites used in the position solution and DOP values.
GSV	The number of GPS satellites in view satellite ID numbers, elevation, azimuth, and SNR values.
RMC	Time, date, position, course and speed data. Recommended Minimum Navigation Information.
VTG	Course and speed information relative to the ground.

Figure 5.16: NMEA sentences (adapted from [27])

5.3.2 Implementation

For the implementation of the sensor, the library provided, [71], represented a great help in the code development. It provides the necessary code for controlling and reading the data coming from the sensor.

Although the sensor can receive data at a 10 Hz update rate, for interpretation purposes it is recommended to maintain the default rate of 1 Hz, so this was the update rate set. Unfortunately, this sensor does not provide information about the speed in its three components, providing only the "speed over ground" and the "course over ground", which in the case of a land vehicle can be considered the Yaw angle, disregarding the occurrence of slip. This way, it was created a data structure where latitude (in degrees), longitude (in degrees), altitude (in meters above sea level), tangential speed (converted from $Knots$ to m/s) and yaw angle (in degrees from true north) were stored. Additionally, information about the number of visible satellites is also provided, so that this variable was also saved with a view to further study of the signal quality.

For the study of the data and verification of the paths, the data stored in the data structure were written in text files. Two files were created, one containing the number of visible satellites and the time when it was recorded. This was done using the arduino function "$millis()$" which returns the number of milliseconds passed since the Arduino board began running the current program. The other file contains the recorded latitude, longitude and altitude. In order for the collected data to be synchronised, a timer was created on the arduino with a duration of 1 s. In this way, every second it is checked if the number of visible satellites is higher or equal than 4, if so, then the coordinates received are saved in the text file intended to save these. The number of visible satellites is saved every time a message is sent by the GPS sensor to the arduino.

For the representation of the coordinates, with the text file containing the coordinates a *.kml* file was created, compatible to be opened through Google's map service, either Google Maps or Google Earth. The text file containing the number of visible satellites is inserted into a spreadsheet and then a graph is constructed with the collected information.

5.3.2.1 Results

To evaluate the robustness of the GPS sensor, a pedestrian test was conducted. In this test, the weather conditions were optimal, as there were no clouds and the wind speed was low. The comparison of the trajectory recorded by the GPS and the actual trajectory can be seen in the next figure:

Figure 5.17: Predefined route (red) and GPS route (green)

The number of satellites visible during the route are as follows:

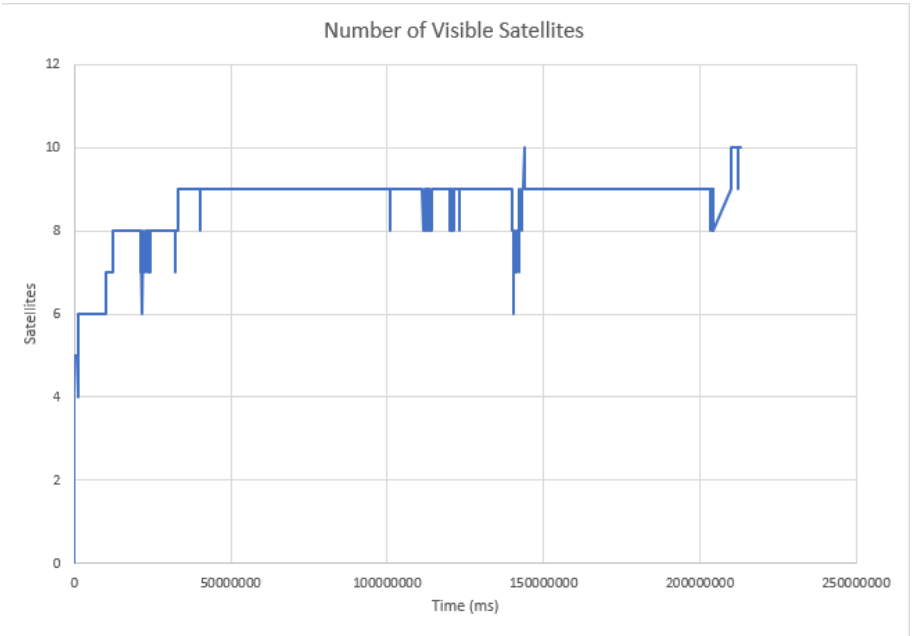

Figure 5.18: Number of visible satellites

5.3.2.2 Discussion

As can be seen in figure 5.18, the number of visible satellites during the entire route was always greater than four. These values are obviously positive taking into account the optimal weather conditions and the absence of trees or tall buildings along the route. However, even though the number of visible satellites was sufficient to enable a correct location, there was a section of the route marked by the absence of received coordinates:

Figure 5.19: Section of the route without coordinates received

This absence may be due to poor quality of the received signal or with horizontal dilution of precision, vertical dilution of precision or position dilution of precision. These last ones characterize the precision of the received signal, when too low, it becomes unfeasible to locate the GPS sensor. When evaluating the error between the actual route and the one plotted by the GPS, it largely turns out that while the pedestrian was moving on the edge of the road, the coordinates received indicate positions on the other side of the road or outside the road. Taking into account the normal width of a road, ranging from 5 to 6 m, it is observed that this is the average value of the error. There is also a section of the course where the error was quite high, exceeding 15 m:

Figure 5.20: Section of the route with high error

Thus, it can be concluded that the GPS solution based on this sensor, when used alone, is sufficient for supervision purposes, i.e. monitoring its position in the plant. Nonetheless, for navigation, it clearly becomes insufficient taking into account the safety constraints required of the AGV and the ability for it to move autonomously. With errors between 5 and 6 m, it is enough for it to leave the intended route, crashing into walls, other vehicles or even overturning, completely damaging the load transported. This justifies the fusion of GPS with other sensors and navigation methods, as is the case of INS, in order to reduce the error and circumvent the problem of lack of signal.

5.4 Conclusions and future work

Regarding the powertrain, the results were as expected, with a slow dynamic response imposed by the high inertia of the system. However, it should be noted that the control of the references, especially in field-weakning control and overload, should be better implemented, being verified that the electromagnetic torque, even demanding higher than nominal current values, presented saturated values close to its nominal value. In what concerns GPS, it was verified that it is not a viable solution for AGV navigation when used alone, requiring other sensors to help combat the periods in which it can not provide coordinates and helping to reduce the position error that was found to be high for what the AGV safety and application needs.

Therefore, for future work, it is necessary to work on the following issues:

- The powertrain requires revision of the reference control methods, the overload control method and the field weakening method. On the other hand, the possibility of applying non-linear control methods to generate the speed reference should be studied. This is because in the simulations a constant load of 5000 kg was considered, being demonstrated the high influence of the inertia of the system. For smaller load values, the system response should be able to be faster, and it may be necessary to adjust the controller gains or the creation of a set of rules. A study on battery charging and discharging is also missing.
- Implementation of the GPS/INS integration method
- Developing an optimisation algorithm that interacts with powertrain and navigation system

- Study and implement a safety algorithm

References

[1] FristAGV.jpg (354×264). URL: https://media.springernature.com/original/springer-static/image/chp{%}3A10.1007{%}2F978-3-662-44814-4{_}1/MediaObjects/290934{_}1{_}En{_}1{_}Fig2{_}HTML.jpg.

[2] Antonio Sciarretta and Ardalan Vahidi. *Energy-Efficient Driving of Road Vehicles*. Lecture Notes in Intelligent Transportation and Infrastructure. Springer International Publishing, Cham, 2019. URL: http://link.springer.com/10.1007/978-3-030-24127-8, doi:10.1007/978-3-030-24127-8.

[3] Torque Slip Characteristics of Induction Motor | Electrical4u. URL: https://www.electrical4u.com/torque-slip-characteristics-of-induction-motor/.

[4] Three-phase voltage source inverter - Simulink. URL: https://www.mathworks.com/help/autoblks/ref/threephasevoltagesourceinverter.html.

[5] Rubén Molina Llorente. *Space Vector Modulation*, pages 427–462. Springer International Publishing, Cham, 2020. URL: https://doi.org/10.1007/978-3-030-34758-1_9, doi:10.1007/978-3-030-34758-1_9.

[6] Qamil Kabashi, Myzafere Limani, Nebi Caka, and Milaim Zabeli. The impact of sampling frequency and amplitude modulation index on low order harmonics in a 3-phase sv-pvm voltage source inverter. *Turkish Journal of Electrical Engineering and Computer Sciences*, Vol 25:184–199, 01 2017. doi:10.3906/ELK.

[7] Performance comparison technology - knowledge base - zubax knowledge base. URL: https://kb.zubax.com/display/MAINKB/Performance+comparison+technology.

[8] Ramesh Chawla Ahmed Rubaai and Joseph Cannon. Laboratory implementation of bang bang controller based motor drive module for modeling and control courses. In *2008 Annual Conference & Exposition*, Pittsburgh, Pennsylvania, June 2008. ASEE Conferences. https://peer.asee.org/3423. doi:10.18260/1-2--3423.

[9] Mirza Begh and Hans-Georg Herzog. Comparison of field oriented control and direct torque control. Technical report, Technical University of Munich, Germany, 03 2018. doi:10.13140/RG.2.2.21677.59360/1.

[10] Rafael Rodríguez-Ponce, Fortino Mendoza-Mondragón, Moisés Martínez-Hernández, and Marcelino Gutiérrez-Villalobos. DTC-FPGA Drive for Induction Motors. In *Induction Motors - Applications, Control and Fault Diagnostics*. InTech, nov 2015. URL: http://www.intechopen.com/books/

induction-motors-applications-control-and-fault-diagnostics/dtc-fpga-drive-for-induction-motors, doi:10.5772/60871.

[11] Rafael Rodríguez-Ponce and Francisco Gustavo Mota-Muñoz. Microcontroller-Based Direct Torque Control Servodrive. *Journal of Robotics*, 2020, 2020. doi:10.1155/2020/9152494.

[12] Haitham Abu-Rub, Atif Iqbal, and Jaroslaw Guzinski. *High Performance Control of AC Drives with Matlab/Simulink*. John Wiley & Sons, 2021.

[13] Gaolin Wang, Yong Yu, Guoqiang Zhang, Bo Wang, Ming Yang, and Dianguo Xu. Chapter 12 - sensorless control of motor drives. In Frede Blaabjerg, editor, *Control of Power Electronic Converters and Systems*, pages 331–369. Academic Press, 2018. URL: https://www.sciencedirect.com/science/article/pii/B9780128052457000123, doi:https://doi.org/10.1016/B978-0-12-805245-7.00012-3.

[14] Epec. Battery Comparison of Energy Density - Cylindrical and Prismatic Cells, 2016. URL: https://www.epectec.com/batteries/cell-comparison.html.

[15] J. Gonçalves and P. Costa. Differential mobile robot controller study: A low cost experiment based on a small arduino based prototype. In *2017 25th Mediterranean Conference on Control and Automation (MED)*, pages 945–950, 2017. doi:10.1109/MED.2017.7984241.

[16] Aboelmagd Noureldin, Tashfeen B. Karamat, and Jacques Georgy. *Basic Navigational Mathematics, Reference Frames and the Earth's Geometry*, pages 21–63. Springer Berlin Heidelberg, Berlin, Heidelberg, 2013. URL: https://doi.org/10.1007/978-3-642-30466-8_2, doi:10.1007/978-3-642-30466-8_2.

[17] Chao Li, Zengcai Wang, and Huisheng Liu. Novel method to integrate marg and an odometer into ahrs for moving vehicles. *Advances in Mechanical Engineering*, 9:168781401772797, 09 2017. doi:10.1177/1687814017727972.

[18] Introduction Transponder Positioning | Götting KG. URL: https://www.goetting-agv.com/components/transponder/introduction.

[19] Aboelmagd Noureldin, Tashfeen B. Karamat, and Jacques Georgy. *Kalman Filter*, pages 225–245. Springer Berlin Heidelberg, Berlin, Heidelberg, 2013. URL: https://doi.org/10.1007/978-3-642-30466-8_7, doi:10.1007/978-3-642-30466-8_7.

[20] Casper Ebbesen Schultz. *INS and GPS integration*. PhD thesis, Technical University of Denmark, Denmark, 2006. URL: www.imm.dtu.dkhttp://etd.dtu.dk/thesis/191665/imm4704.pdf.

[21] Miguel Tradacete, Álvaro Sáez, Juan Felipe Arango, Carlos Gómez Huélamo, Pedro Revenga, Rafael Barea, Elena López-Guillén, and Luis Miguel Bergasa. Positioning system for an electric autonomous vehicle based on the fusion of multi-gnss rtk and odometry by using an extented kalman filter. In Raquel Fuentetaja Pizán, Ángel García Olaya, Maria Paz Sesmero Lorente, Jose Antonio Iglesias Martínez, and Agapito Ledezma Espino, editors, *Advances in Physical Agents*, pages 16–30, Cham, 2019. Springer International Publishing.

[22] Seunghwan Choi, Kijung Kim, Yunki Kim, and Jangmyung Lee. Outdoor Precision Position Estimation System Using Multi-GPS Receivers. In Jangmyung Lee, Min Cheol Lee, Honghai Liu, and Jee-Hwan Ryu, editors, *Intelligent Robotics and Applications*, pages 66–76, Berlin, Heidelberg, 2013. Springer Berlin Heidelberg.

[23] Tobe Toben, Sönke Eilers, Christian Kuka, Sören Schweigert, Hannes Winkelmann, and Stefan Ruehrup. Safe Autonomous Transport Vehicles in Heterogeneous Outdoor Environments. In Reiner Hähnle, Jens Knoop, Tiziana Margaria, Dietmar Schreiner, and Bernhard Steffen, editors, *Leveraging Applications of Formal Methods, Verification, and Validation*, pages 61–75, Berlin, Heidelberg, 2012. Springer Berlin Heidelberg. doi:https://doi.org/10.1007/978-3-642-34781-8_5.

[24] J. Grabocka, A. Dalkalitsis, A. Lois, E. Katsaros, and L. Schmidt-Thieme. Realistic optimal policies for energy-efficient train driving. In *17th International IEEE Conference on Intelligent Transportation Systems (ITSC)*, pages 629–634, 2014. doi:10.1109/ITSC.2014.6957760.

[25] Aboelmagd Noureldin, Tashfeen B. Karamat, and Jacques Georgy. *Inertial Navigation System Modeling*, pages 167–200. Springer Berlin Heidelberg, Berlin, Heidelberg, 2013. URL: https://doi.org/10.1007/978-3-642-30466-8_5, doi:10.1007/978-3-642-30466-8_5.

[26] Umar Iqbal, Tashfeen B. Karamat, Aime F. Okou, and Aboelmagd Noureldin. Experimental Results on an Integrated GPS and Multisensor System for Land Vehicle Positioning. *International Journal of Navigation and Observation*, 2009:1–18, jun 2009. doi:10.1155/2009/765010.

[27] Adafruit. Adafruit Ultimate GPS Breakout - 66 channel w/10 Hz updates [Version 3] ID: 746 - $39.95 : Adafruit Industries, Unique & fun DIY electronics and kits, 2015. URL: https://www.adafruit.com/product/746https://www.adafruit.com/products/746.

[28] Günter Ullrich. *Automated Guided Vehicle Systems*. Springer Berlin Heidelberg, Berlin, Heidelberg, 2015. URL: http://link.springer.com/10.1007/978-3-662-44814-4, doi:10.1007/978-3-662-44814-4.

[29] Three-phase induction motor - Simulink. URL: https://www.mathworks.com/help/autoblks/ref/inductionmotor.html.

[30] Somjit Swain, Devendra Singh Mandavi, and Arup Avishek Behera. *Comparison of Performance Analysis of Different Control Structures*. PhD thesis, National Institute of Technology, Rourkela, 2012. URL: https://core.ac.uk/download/pdf/53188593.pdf.

[31] Najib El Ouanjli, Aziz Derouich, Abdelaziz El Ghzizal, Saad Motahhir, Ali Chebabhi, Youness El Mourabit, and Mohammed Taoussi. Modern improvement techniques of direct torque control for induction motor drives - a review. *Protection and Control of Modern Power Systems*, 4(1):11, dec 2019. URL: https://pcmp.springeropen.com/articles/10.1186/s41601-019-0125-5, doi:10.1186/s41601-019-0125-5.

[32] Bogdan Enache, Emilian Lefter, and Constantin Stoica. Comparative study for generic battery models used for electric vehicles. In *2013* -

8th International Symposium on Advanced Topics in Electrical Engineering, ATEE 2013, 2013. URL: https://www.academia.edu/45415550/Comparative{_}study{_}for{_}generic{_}battery{_}models{_}used{_}for{_}electric{_} doi:10.1109/ATEE.2013.6563497.

[33] Aboelmagd Noureldin, Tashfeen B. Karamat, and Jacques Georgy. *Introduction*, pages 1–20. Springer Berlin Heidelberg, Berlin, Heidelberg, 2013. URL: https://doi.org/10.1007/978-3-642-30466-8_1, doi:10.1007/978-3-642-30466-8_1.

[34] Jasprabhjit Mehami, Mauludin Nawi, and Ray Y. Zhong. Smart automated guided vehicles for manufacturing in the context of Industry 4.0. *Procedia Manufacturing*, 26:1077–1086, 2018. URL: www.sciencedirect.comAvailableonlineatwww.sciencedirect.comwww.elsevier.com/locate/procediahttps://linkinghub.elsevier.com/retrieve/pii/S2351978918308205, doi:10.1016/j.promfg.2018.07.144.

[35] The Past, Present and Future of AGVs - Fred Automation. URL: https://www.fredagv.com/news/the-past-present-and-future-of-agvs/.

[36] The 1980's: a decade of job growth and industry shifts. URL: https://www.bls.gov/opub/mlr/1990/09/Art1full.pdf.

[37] Automatizando o transporte de peças. URL: https://www.seat.pt/empresa-seat/noticias-auto/novidades-automoveis/SEAT-implementa-robots-autonomos.html.

[38] Robots take to the streets. URL: https://www.seat.com/company/news/cars/robots-take-to-the-streets.html.

[39] ISO 3691-4:2020 – A new standard for industrial driverless trucks. URL: https://www.linkedin.com/pulse/iso-3691-42020-new-standard-industrial-driverless-kidman-phd?trk=public{_}profile{_}article{_}view.

[40] Name Josip Babi and Josip Babi. Guidelines for Personal Safety in Flexible Automated Warehouses. Technical report, KEEI, 2017.

[41] *Safety of Mobile Robot Systems in Industrial Applications*, 2019. doi:10.3217/978-3-85125-663-5-04.

[42] Clarke and Park Transforms - MATLAB & Simulink. URL: https://www.mathworks.com/solutions/power-electronics-control/clarke-and-park-transforms.htmlhttps://au.mathworks.com/solutions/power-electronics-control/clarke-and-park-transforms.html.

[43] Ali Abdul and Ali Altahir. Park and Clark Transformations Park and Clark Transformations: A Short Review, 04 2020. doi:10.13140/RG.2.2.20287.46241.

[44] Implement ab to $\alpha\beta$ transformation - Simulink. URL: https://www.mathworks.com/help/mcb/ref/clarketransform.html.

[45] Implement $\alpha\beta$ to abc transformation - Simulink. URL: https://www.mathworks.com/help/mcb/ref/inverseclarketransform.html.

[46] Implement $\alpha\beta$ to dq transformation - Simulink. URL: https://www.mathworks.com/help/mcb/ref/parktransform.html.

[47] Implement dq to $\alpha\beta$ transformation - Simulink. URL: https://www.mathworks.com/help/mcb/ref/inverseparktransform.html.

[48] Freescale Semiconductor. Sensorless ACIM Motor Control Using MC56F82748. URL: https://www.nxp.com/docs/en/application-note/AN5210.pdf?ICID=I-CT-TECH-RES-CLA-JUN{_}21-896.

[49] D Arun Dominic and Thanga Raj Chelliah. Analysis of field-oriented controlled induction motor drives under sensor faults and an overview of sensorless schemes. *ISA Transactions*, 53(5):1680–1694, 2014. ICCA 2013. URL: https://www.sciencedirect.com/science/article/pii/S0019057814000871, doi:https://doi.org/10.1016/j.isatra.2014.04.008.

[50] K. Zeb, Z. Ali, K. Saleem, W. Uddin, M. A. Javed, and N. Christofides. Indirect field-oriented control of induction motor drive based on adaptive fuzzy logic controller. *Electrical Engineering 2016 99:3*, 99(3):803–815, oct 2016. URL: https://link.springer.com/article/10.1007/s00202-016-0447-5, doi:10.1007/S00202-016-0447-5.

[51] Anupam Mishra, Sunil Panda, and Srinivas B. *Control of Voltage Source Inverters using PWM/SVPWM for Adjustable Speed Drive Applications*. PhD thesis, National Institute Of Technology Rourkela, 2009. URL: https://core.ac.uk/download/pdf/53187171.pdf.

[52] Saurabh Kharjule. Voltage source inverter. In *2015 International Conference on Energy Systems and Applications*, pages 537–542, 2015. doi:10.1109/ICESA.2015.7503407.

[53] Robert D. Christ and Robert L. Wernli. Chapter 7 - power and telemetry. In Robert D. Christ and Robert L. Wernli, editors, *The ROV Manual (Second Edition)*, pages 141–161. Butterworth-Heinemann, Oxford, second edition edition, 2014. URL: https://www.sciencedirect.com/science/article/pii/B9780080982885000075, doi:https://doi.org/10.1016/B978-0-08-098288-5.00007-5.

[54] Ghadeer Soud Al Shayaa and Hisham Mohamed Tawfik. Voltage Source Inverters Control using PWM/SVPWM For Adjustable Speed Drive Applications. *IOSR Journal of Electrical and Electronics Engineering*, 9(1):29–45, 2014. URL: www.iosrjournals.orgwww.iosrjournals.orghttp://www.iosrjournals.org/iosr-jeee/Papers/Vol9-issue1/Version-4/D09142945.pdf, doi:10.9790/1676-09142945.

[55] Waheed Ahmed and Syed M Usman Ali. Comparative study of SVPWM (space vector pulse width modulation) & SPWM (sinusoidal pulse width modulation) based three phase voltage source inverters for variable speed drive. *IOP Conference Series: Materials Science and Engineering*, 51:012027, dec 2013. URL: https://doi.org/10.1088/1757-899x/51/1/012027, doi:10.1088/1757-899x/51/1/012027.

[56] José Fernando Silva and Sónia F. Pinto. 35 - linear and nonlinear control of switching power converters. In Muhammad H. Rashid, editor, *Power Electronics Handbook (Fourth Edition)*, pages 1141–1220. Butterworth-Heinemann, fourth edition edition, 2018. URL: https://www.sciencedirect.com/science/article/pii/B9780128114070000398, doi:https://doi.org/10.1016/B978-0-12-811407-0.00039-8.

[57] Pid controller: Working, types, advantages and its applications. URL: https://www.elprocus.com/the-working-of-a-pid-controller/.

[58] Field-Oriented Control (FOC) - MATLAB & Simulink. URL: https://www.mathworks.com/help/mcb/gs/implement-motor-speed-control-by-using-field-oriented-control-foc.html.

[59] Venu Gopal B T. Comparison Between Direct and Indirect Field Oriented Control of Induction Motor. *International Journal of Engineering Trends and Technology*, 43(6):364–369, 2017. URL: http://www.ijettjournal.org, doi:10.14445/22315381/ijett-v43p260.

[60] Calculate slip speed of AC induction motor - Simulink. URL: https://www.mathworks.com/help/mcb/ref/acimslipspeedestimator.html.

[61] Cong Jiang, Shunli Wang, Bin Wu, Carlos Fernandez, Xin Xiong, and James Coffie-Ken. A state-of-charge estimation method of the power lithium-ion battery in complex conditions based on adaptive square root extended kalman filter. *Energy*, 219:119603, 2021. URL: https://www.sciencedirect.com/science/article/pii/S0360544220327109, doi:https://doi.org/10.1016/j.energy.2020.119603.

[62] Antonio Angrisano. *GNSS/INS Integration Methods*. PhD thesis, Universita' Degli Studi Di Napoli, Napoli, 2010. URL: https://schulich.ucalgary.ca/labs/position-location-and-navigation/files/position-location-and-navigation/angrisano2010{_}phd.pdf.

[63] What Is SLAM (Simultaneous Localization and Mapping) – MATLAB & Simulink - MATLAB & Simulink. URL: https://www.mathworks.com/discovery/slam.htmlhttps://la.mathworks.com/discovery/slam.html.

[64] Zheyuan Lu, Zhencheng Hu, and Keiichi Uchimura. Slam estimation in dynamic outdoor environments: A review. In Ming Xie, Youlun Xiong, Caihua Xiong, Honghai Liu, and Zhencheng Hu, editors, *Intelligent Robotics and Applications*, pages 255–267, Berlin, Heidelberg, 2009. Springer Berlin Heidelberg.

[65] Aboelmagd Noureldin, Tashfeen B. Karamat, and Jacques Georgy. *Global Positioning System*, pages 65–123. Springer Berlin Heidelberg, Berlin, Heidelberg, 2013. URL: https://doi.org/10.1007/978-3-642-30466-8_3, doi:10.1007/978-3-642-30466-8_3.

[66] Spyros G. Tzafestas. 12 - mobile robot localization and mapping. In Spyros G. Tzafestas, editor, *Introduction to Mobile Robot Control*, pages 479–531. Elsevier, Oxford, 2014. URL: https://www.sciencedirect.com/science/article/pii/B9780124170490000122, doi:https://doi.org/10.1016/B978-0-12-417049-0.00012-2.

[67] Shota Muroi, Koichiro Iijima, and Masafumi Ekawa. Development of a wide area satellite-based surveillance system utilizing rtk-gnss to monitor displacement of slopes and infrastructure. In Phung Duc Long and Nguyen Tien Dung, editors, *Geotechnics for Sustainable Infrastructure Development*, pages 1171–1176, Singapore, 2020. Springer Singapore.

[68] K.T. Chau. 21 - pure electric vehicles. In Richard Folkson, editor, *Alternative Fuels and Advanced Vehicle Technologies for Improved Environmental Performance*, pages 655–684. Woodhead Publishing, 2014. URL: https://www.sciencedirect.com/science/article/pii/B9780857095220500212, doi:https://doi.org/10.1533/9780857097422.3.655.

[69] V. Stajilov and C. Bujoreanu. Regenerative braking kinematic analysis and optimisation strategies. In *IOP Conference Series: Materials Science and Engineering*, volume 997, 2020. URL: www.scopus.com.

[70] S. Su, X. Wang, Y. Cao, and J. Yin. An energy-efficient train operation approach by integrating the metro timetabling and eco-driving. *IEEE Transactions on Intelligent Transportation Systems*, 21(10):4252–4268, 2020. doi:10.1109/TITS.2019.2939358.

[71] Adafruit. An interrupt-based GPS library for no-parsing-required use, 2015. URL: https://github.com/adafruit/Adafruit{_}GPS.